DIRECT TORQUE CONTROL STRATEGIES FOR INTERIOR PERMANENT MAGNET SYNCHRONOUS MOTORS DRIVEN BY A THREE-LEVEL SIMPLIFIED NEUTRAL POINT CLAMPED INVERTER

A THESIS SUBMITTED TO AUCKLAND UNIVERSITY OF TECHNOLOGY
IN FULFILMENT OF THE REQUIREMENTS FOR THE DEGREE OF
DOCTOR OF PHILOSOPHY

By

Tung Ngo

School of Engineering, Computer and Mathematical Sciences

August 2018

Declaration

I hereby declare that this submission is my own work and that, to the best of my knowledge and belief, it contains no material previously published or written by another person nor material which to a substantial extent has been accepted for the qualification of any other degree or diploma of a university or other institution of higher learning.

Signature of candidate

Acknowledgements

First of all, I would like to express my sincere thanks to my supervisor, Dr. Gilbert Foo, for his guidance and support throughout my PhD studies. His impressive knowledge and human qualities have been a source of inspiration for me. He has been patiently answering all my technical questions regarding to this project, giving me a lot of valuable advice and guiding me through the right direction. Without him, this project would not have been possibly completed.

I wish to extend my sincere gratitude to my co-supervisor, Dr. Craig Baguley, for his constant support, constructive suggestions and helpful discussions. He has helped me a lot in designing the power multilevel inverter and trouble-shooting the circuits used in this project.

I also would like to thanks Mr. Jian Huang and Mr. Stephen Hartley for their technical support in designing and fabricating the printed circuit boards, as well as logistical support.

I extend my thanks to Dr. Zhang Xinan from Nanyang Technological University for his advice in programming the digital signal processor evaluation board used in this project.

A special thanks to Fransa Van Zijl for her technical support on dSPACE system, and her friendship.

To the Auckland University of Technology, I would like to express my gratitude for providing financial support for my fourth year of research study.

To the Ministry of Education of Vietnam, I would like to express my sincere thanks for providing three years financial support for my research study through the PhD fellowship Project 911.

To all my friends, I wish to express my gratitude for their friendship and moral support.

Last, but not least, I would like to express my deepest gratitude to my parents, family members and especially to my wife Phuong Dao, my daughter Linh Ngo and my son Quang Ngo for their unconditional support, encouragement and love, and without which I would not have come this far.

Abstract

The three-level simplified neutral point clamped (3L-SNPC) was first proposed in 1993. Compared to the T-type and NPC inverters, it uses fewer switching devices to generate a multilevel waveform. This makes the 3L-SNPC inverter attractive for low-voltage motor drive applications. However, and to date, it has received comparatively little research attention, particularly in relation to suitable control strategies. The work described in this thesis addresses this shortcoming through proposing several direct torque control (DTC) strategies for 3L-SNPC inverter-fed interior permanent magnet synchronous motor (IPMSM) drives.

A duty-cycle-control-based DTC strategy with torque ripple reduction suited to the 3L-SNPC inverter is firstly proposed. It utilises hysteresis controllers to directly control electromagnetic torque and stator flux within hysteresis bands. To reduce the torque ripples the proposed strategy employs two voltage vectors within each sampling cycle. The duty cycle of each applied voltage vector is calculated from knowledge of the torque error and rotor speed. In addition, the proposed algorithm incorporates neutral point voltage balancing. The experimental results indicate that the proposed duty-cycle-control-based DTC strategy achieves smaller torque and flux ripples compared to a non-duty-cycle-based DTC strategy.

Another control method proposed in this thesis is predictive torque control (PTC). It uses stator current and rotor speed values to predict both the electromagnetic torque and

stator flux. Then, the most appropriate voltage vector that minimises a predetermined cost function and, hence, the torque error is selected. To further reduce the torque error, duty-cycle-control and neutral point voltage balancing methods are incorporated. The combined duty-cycle PTC method necessitates variable switching frequency operation. To address this issue, torque-regulator-based DTC and space vector modulation (SVM) based deadbeat PTC (DB-PTC) strategies are proposed.

The proposed torque-regulator-based DTC strategy employs a PI torque controller and four triangular-carriers to attain torque ripple reduction at a constant switching frequency. The hysteresis torque levels are determined by comparing the output of the PI torque controller with four triangular-carriers. With knowledge of the torque and flux error levels, an appropriate voltage vector is selected from a switching table to regulate the torque and stator flux. In this method the PI torque controller is used to negate the large rate of torque variation, while periodic triangular-carriers are used to achieve a constant switching frequency.

On the other hand, the proposed DB-PTC strategy achieves a constant switching frequency through the adoption of a novel SVM. The desired voltage vector is determined on the basis of the deadbeat control and synthesized using SVM. The proposed SVM algorithm is developed specifically for the 3L-SNPC inverter and overcomes the problem of a lack of medium voltage vectors. The algorithm involves selecting the switching sequence in a manner to assure pole voltages can only change by one voltage level at most during each voltage vector transition. In addition, the algorithm assures that all reference voltage vectors confined to the hexagonal limit of the inverter can be synthesized. With the adoption of SVM, torque and flux ripples are significantly reduced.

All control strategies presented in this thesis are novel and described, modelled and experimentally verified under both steady-state and dynamic test conditions. A comprehensive comparative evaluation of the strategies is also carried out. All proposed

strategies represent a contribution to knowledge, and are expected to improve the attractiveness of the 3L-SNPC inverter for future motor drive applications.

Contents

List of Tables

List of Figures

Nomenclature

Acronyms

3L-ANPC	three-level active neutral point clamped
3L-FC	three-level flying capacitor
3L-NPC	three-level neutral point clamped
3L-SNPC	three-level simplified neutral point clamped
5L-ANPC	five-level active neutral point clamped
5L-FC	five-level flying capacitor
5L-NPC	five-level neutral point clamped
AC	alternating current
CHB	cascaded H-bride
DB-PTC	deadbeat predictive torque control
DC	direct current
DTC	direct torque control
EV	electric vehicle
FC	flying capacitors
FCS-PTC	finite control state predictive torque control
FOC	field-oriented control
IPMSMs	interior permanent magnet synchronous motors

NPC	neutral point clamped
PM	permanent magnet
PMSM	permanent magnet synchronous motor
PTC	predictive torque control
SPMSMs	surface mounted permanent magnet synchronous motors
SVM	space vector modulation
SVM-DTC	space vector modulation based direct torque control

Symbols

$\boldsymbol{\lambda_s}$	stator flux linkage vector in the stationary reference frame
$\boldsymbol{i_s}$	stator current vector in the stationary reference frame
$\boldsymbol{v_s}$	stator voltage vector in the stationary reference frame
δ	load angle
ΔV_C	difference between the two DC-link capacitor voltages
λ_a	active flux
λ_s	stator flux linkage
λ_{rated}	rated flux
$(x-y)$	stator flux reference frame
ω_n	natural frequency of the system
ω_s	speed of stator flux linkage vector
ω_{rated}	rated speed of motor
ω_{re}	electrical speed of motor
ξ	damping ratio of the system
C_1	DC-link capacitor
C_2	DC-link capacitor

i_x	stator current in the x-axis
i_y	stator current in the y-axis
k_f	weighting factor
P	number of pole pairs
P_m	motor power
R_s	stator resistance
T_e	electromagnetic torque
T_e^*	reference torque
T_e^0	initial value of instantaneous torque
T_{rated}	rated torque
v_x	stator voltage in the x-axis
v_y	stator voltage in the in the y-axis
V_{C1}	voltage across DC-link capacitor C_1
V_{C2}	voltage across DC-link capacitor C_2
V_{dc}	DC-link voltage

Chapter 1

Introduction

1.1 AC Motors

An AC motor is an electric machine driven by an alternating current (AC) that converts electrical energy into mechanical energy. Basically, AC motors can be classified into two categories: induction and synchronous. The induction motor has been widely used in the industry due to its solid rotor structure and low manufacturing cost. In induction motors, the rotor field is produced by electromagnetic induction action, if the alternating currents are applied directly to the stator windings. In contrast, the rotor field of conventional synchronous motors is excited with direct current (DC). Alternatively, permanent magnet (PM) synchronous motors utilise permanent magnets to generate DC magnetic flux. Due to the absent of losses associated with the rotor, PM synchronous motors have higher efficiency than induction motors.

PM synchronous motors can be classified into two categories: surface mounted PM synchronous motors (SPMSMs) and interior PM synchronous motors (IPMSMs). As shown in Figure 1.1, SPMSMs have permanent magnets fixed to the outer surface of the rotor while IPMSMs have permanent magnets inserted in the rotor. It is apparent

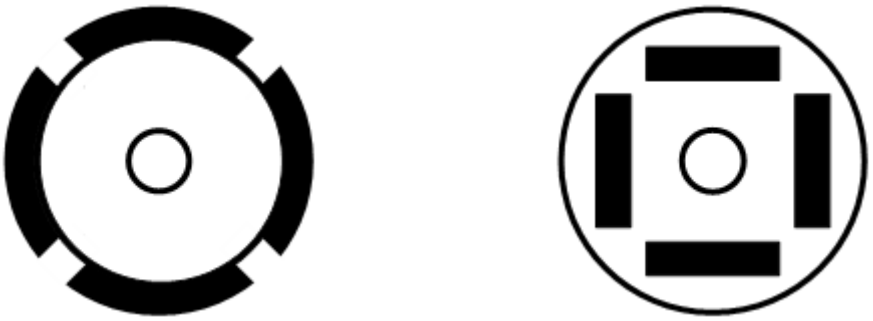

(a) SPMSM (b) IPMSM

Figure 1.1: Rotor Structure of IPMSM.

that IPMSMs have a stronger rotor structure than SPMSMs. Furthermore, due to the saliency of the rotor, reluctance torque is generated in IPMSMs. Therefore, IPMSMs have higher torque density compared to SPMSMs.

1.2 Electric Vehicle and IPMSM Drives

Electric vehicles (EVs) have significant advantages over internal combustion engine alternatives in terms of carbon footprint, as well as performance. A critical enabler of improved EV performance is the propulsion system, which is commonly implemented using the induction motor and the interior permanent magnet synchronous motor (IPMSM) [1–4]. However, and for traction applications, the IPMSM is preferable to the induction motor, due to its higher power density and efficiency [5]. Further advantages of IPMSM drives for EV applications can be realized, depending on the control strategy employed. Field-oriented control (FOC), which was introduced in the 1970s [6], is the most well-known control method. The control block diagram of FOC is illustrated in Figure 1.2, and is based on the transformation of three-phase stator currents into a two co-ordinate synchronous rotating reference frame. The stator currents are therefore visualized as a vector with two orthogonal components, one which defines the torque, the other flux. This enables torque and flux to be regulated by controlling the torque and

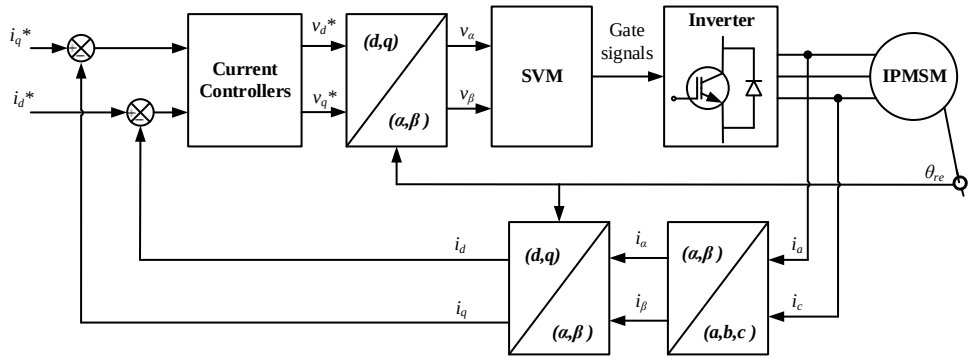

Figure 1.2: Block diagram of the FOC strategy.

flux components of the stator current vector. As a coordinate transformation is required, the rotor angle must be known. It can be directly measured using an encoder mounted on the rotor shaft, or estimated based on a model of the machine.

Implementing IPMSM drives with FOC gives excellent steady-state torque and flux responses over a wide range of operating speeds at a constant switching frequency. However, the presence of two PI current controllers, a space vector modulation (SVM) block and coordinate transformations complicate the control structure. Further, the dynamic response is sluggish, due to the characteristic of the PI controller.

Direct torque control (DTC) for IPMSM was introduced in the 1990s [7, 8]. The control block diagram of this strategy is shown in Figure 1.3. DTC requires neither the SVM block, nor current controllers. Rather, the torque and stator flux are directly regulated by selecting appropriate voltage vectors from a switching table. In addition, the use of hysteresis control facilitates fast torque and stator flux dynamics. Therefore, DTC offers superior dynamic response and is robust against machine parameter variations. Disadvantages include high torque ripple and a variable switching frequency. A number of modified DTC schemes have been proposed to overcome these drawbacks. The duty-cycle-control-based DTC [9–12] and the SVM-based DTC [13–16] method have

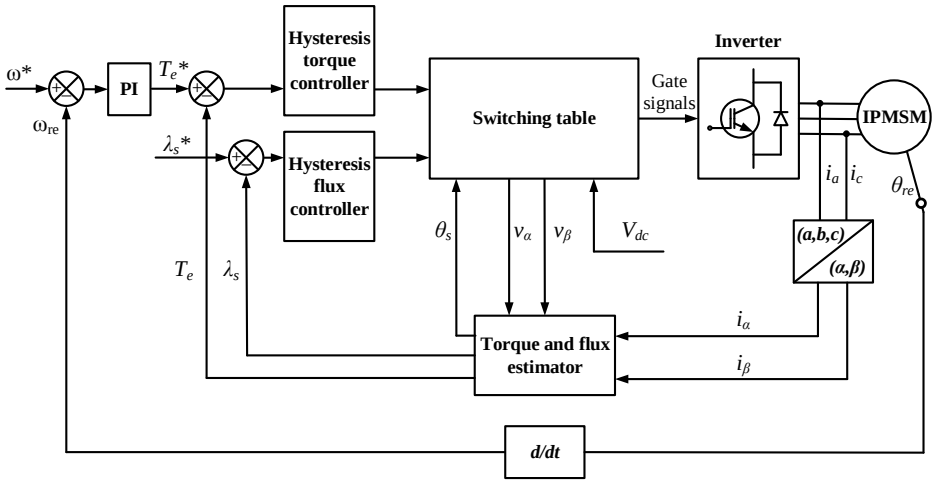

Figure 1.3: Block diagram of the DTC strategy.

been amongst the most popular methods.

Another direct torque control method for the IPMSM is predictive torque control (PTC) [17–27]. PTC can be classified into two categories: continuous PTC and finite control state PTC (FCS-PTC). In the former, a SVM block is needed to synthesize a continuous reference voltage output from the controller. Thus, a constant switching frequency is achieved. In the latter, and differently, the reference voltage vector is selected from a finite set of voltage vectors of a power inverter. Figure 1.4 illustrates the control block diagram of the FCS-PTC strategy. The voltage vector that minimizes the defined cost function and, hence, torque and flux errors, will be selected. However, and due to the absence of a modulator, a constant switching frequency cannot be achieved in FCS-PTC. In addition, the computational burden is high because of the existence of several selective voltage vectors in each sampling cycle. Compared to DTC, FCS-PTC has a simpler control structure, yet maintains the advantage of a fast dynamic response [24]. However, high torque ripple levels are incurred, because of the use of only one voltage vector within each sampling cycle [21]. Due to the importance of reducing torque ripple significant research effort exists in this area [21, 23].

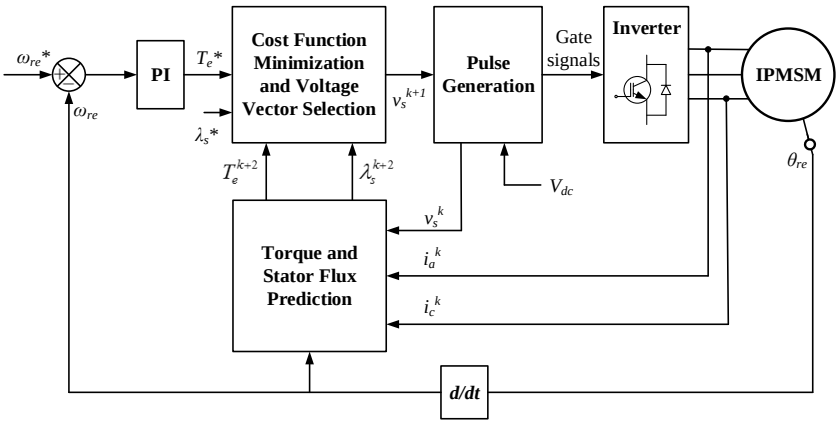

Figure 1.4: Block diagram of the PTC strategy.

The performance of the IPMSM drive depends not only on the control strategy employed but also on the type of power inverter. In general, a two-level inverter is used to power the IPMSM. The total harmonic distortion of the stator current can be reduced by increasing the switching frequency of the inverter. But, it will increase the total inverter losses, which requires more efficient cooling systems [3]. Multilevel inverters can be used as an alternative in this respect [28]. Compared to the two-level inverter, multilevel inverters are able to operate at lower switching frequency and dv/dt levels and with reduced harmonic distortion in drive output waveforms. Experimental results presented in [29] show that the proposed drive system achieved better total efficiency compared to the conventional two-level inverter-fed motor drive solution. However, and disadvantageously, multilevel inverters require significant number of semiconductor devices, increasing overall system complexity and cost. The three-level simplified neutral point clamped (3L-SNPC) inverter can be used to overcome this drawback.

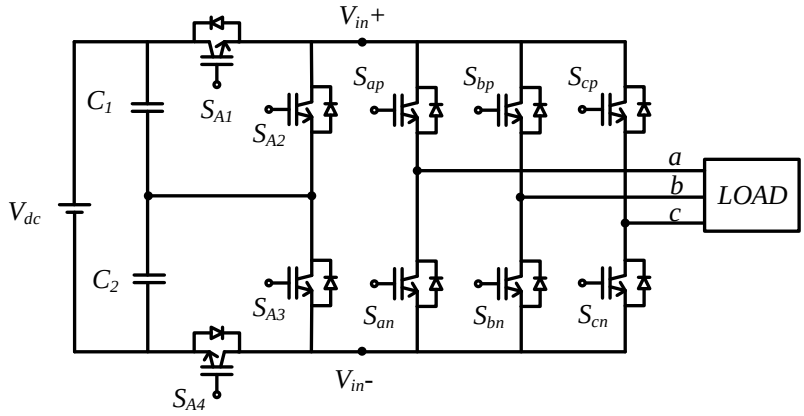

Figure 1.5: Circuit diagram of the 3L-SNPC inverter

1.3 Three-level Simplified Neutral Point Clamped Inverter

First proposed in [30] , the three-level simplified neutral point clamped (3L-SNPC) inverter uses less number of semiconductor devices to generate multilevel output voltage waveforms. Originally, the 3L-SNPC inverter was employed with gate turn-off thyristors. However, it can be implemented with IGBTs, as depicted in Figure 1.5.

As shown in Figure 1.5, the 3L-SNPC inverter comprises a dual-buck converter $(S_{A1} - S_{A4})$ and a conventional two-level inverter $(S_{ap}, S_{bp}, S_{cp}, S_{an}, S_{bn}, S_{cn})$. This arrangement only requires only 10 active switches, which is fewer than both the conventional three-level NPC (3L-NPC) and T-type inverters. The 3L-NPC inverter requires at least 12 actives switches and/or 6 diodes. On the other hand, while no diodes are needed, the T-type inverter needs 12 active switches of which half are bidirectional. Moreover, due to the absence of medium voltage vectors, the problem of neutral point voltage imbalance is less severe in the 3L-SNPC inverter. This means smaller DC-link capacitors can be used. These features make the 3L-SNPC inverter very suitable for EVs, for which the operating voltages are in the range 200 to 800 Volts [31].

1.4 Research Objective

Compared to its three-level counterparts, the 3L-SNPC inverter uses less switching devices to generate multilevel output voltage waveforms. Moreover, the issue of the neutral point voltage imbalance is less severe, due to the absence of the medium voltage vectors. This makes the 3L-SNPC inverter very suitable for EV applications. However, and to date, the development of low-voltage high performance IPMSM drives fed from 3L-SNPC inverters has received little research attention. Consequently, the fundamental objective of the work presented in this thesis is to contribute to scientific knowledge through the development and experimental verification of novel control strategies suited to 3L-SNPC inverter-fed IPMSM drives. A particular focus is placed on direct torque control strategies.

1.5 Outline of the Thesis

The chapters of this thesis are arranged as follows:

Chapter 1 gives an introduction of the EV and IPMSM drives. The main control strategies for IPMSM are briefly reviewed. The 3L-SNPC inverter are also introduced. The main objective of this research is discussed then.

Chapter 2 presents a brief review of multilevel inverter topologies. The advantages and disadvantages of the 3L-SNPC inverter are highlighted.

Chapter 3 proposes a duty-cycle-control-based DTC strategy with torque ripple reduction suited to the 3L-SNPC inverter-fed IPMSM drive. It includes an analysis the relation between rate of torque variation and voltage vectors, as well as explanations for the proposed switching table and duty cycle calculations. Furthermore, the neutral point voltage balancing is addressed. The performance of the duty-cycle-control-based

DTC strategy is also compared with that of the non-duty-cycle-control-based DTC in experiments.

Chapter 4 presents a PTC strategy. To reduce the torque ripples, a duty-cycle-control-based PTC strategy is implemented. The voltage vectors are selected to minimize the torque ripples and simultaneously balance the two DC-link capacitor voltages. All design equations pertain to the stationary $(\alpha - \beta)$ reference frame are presented in details. The robustness of the proposed PTC strategy is also discussed.

Chapter 5 presents a torque-regulator-based DTC strategy. It includes analysis and design of the proposed torque regulator. The proposed strategy achieves a constant switching frequency and also reduced torque ripples through the use of a simple PI torque controller and a triangular-wave carrier-based comparator. The robustness merits of the DTC strategy is preserved.

Chapter 6 proposes a deadbeat-based PTC (DB-PTC) strategy, which adopts a novel SVM algorithm specific to the 3L-SNPC inverter. The desired voltage vector is determined on the basis of the deadbeat control and synthesized using SVM. With the adoption of SVM, the torque and flux ripples are significantly reduced. In addition, a constant switching frequency is also achieved.

Chapter 7 presents a comparative evaluation of all proposed strategies. The evaluation is conducted on the basis of several criteria: torque and flux ripples, stator current total harmonic distortions and neutral point voltage fluctuations.

Chapter 8 presents the conclusions and some suggestions for future research.

Chapter 2

Review of Multilevel Inverters Topologies

2.1 Introduction

Multilevel inverters are widely used in many applications [28, 32–35]. Since the concept of multilevel inverter was first introduced in 1975 [36], various multilevel inverter topologies has been developed [37–44], and can be classified into neutral point clamped (NPC), flying capacitors (FC) and cascaded categories. Such a classification is shown in Figure 2.1. In this chapter a review of multilevel inverter topologies for motor drive applications is presented.

2.2 NPC Inverters

2.2.1 Diode NPC Inverters

The three-level neutral point clamped (3L-NPC) inverter was introduced in [37]. The main circuit diagram of the 3L-NPC inverter is illustrated in Figure 2.2. Each phase leg

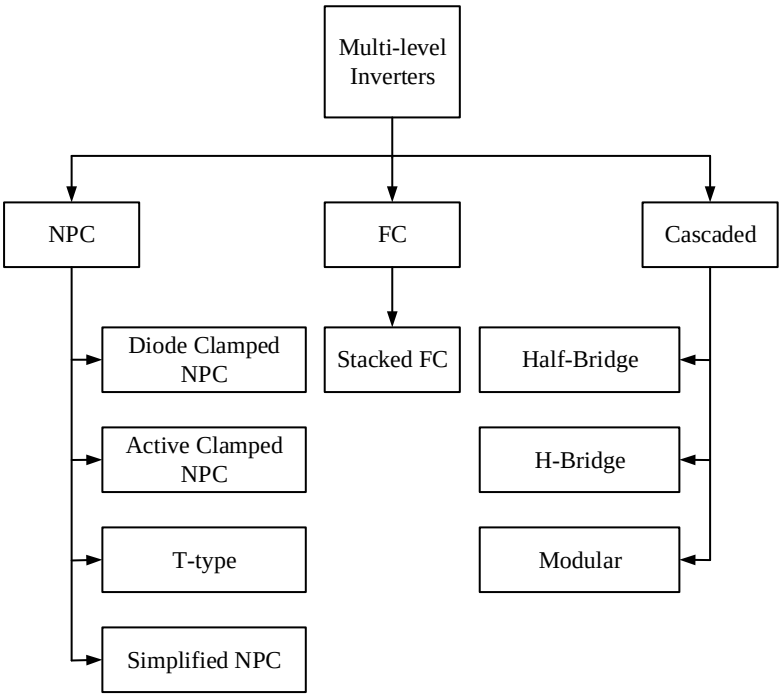

Figure 2.1: Multilevel inverters classification.

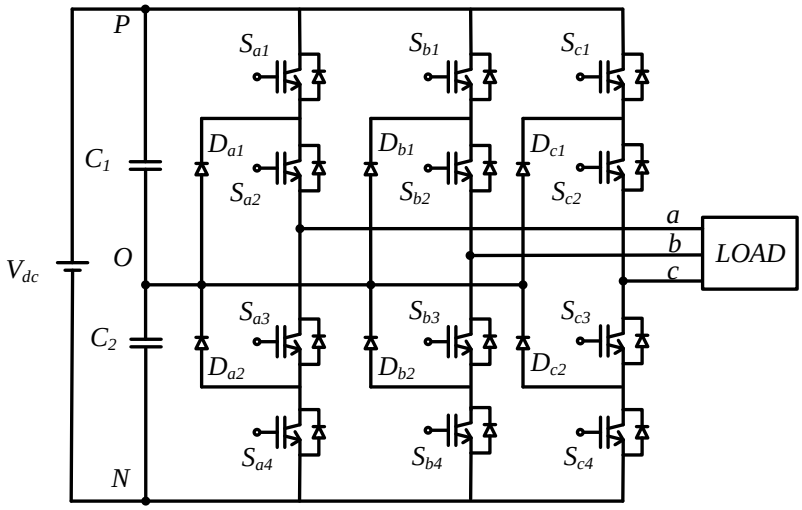

Figure 2.2: Circuit diagram of the 3L-NPC inverter

of the 3L-NPC inverter consists of four switching devices along with their anti-parallel diodes and two clamping diodes. The switching devices have only to block half of the DC-link voltage (V_{dc}). At each instant of time, only two of the four switching devices in

each phase leg are turned on. According to the switching combinations of $(S_{a1} - S_{a4})$ in Table 2.1, the possible voltage across the inverter output terminals *'a'* and the neutral point *'O'* can be $V_{dc}/2$, $-V_{dc}/2$ or 0. Therefore, the three-level output at the inverter output terminals (a, b, c) can be produced. The current commutation during switching in one phase leg for positive and negative output current are shown in Figure 2.3.

Switching combination				V_{aO}
S_{a1}	S_{a2}	S_{a3}	S_{a4}	
1	1	0	0	$V_{dc}/2$
0	1	1	0	0
0	0	1	1	$-V_{dc}/2$

Table 2.1: Switching combinations for phase leg-*a* of the 3L-NPC inverter

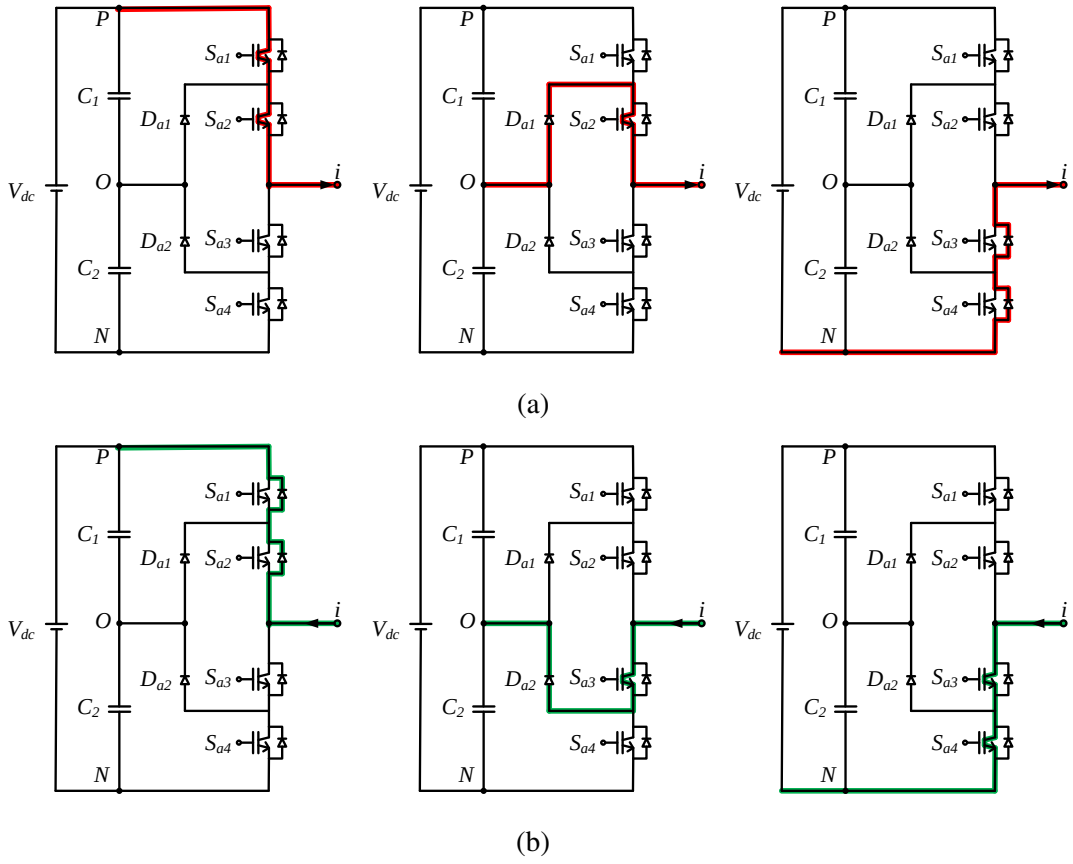

Figure 2.3: Current commutation during switching for (a) positive and (b) negative output current of the 3L-NPC inverter.

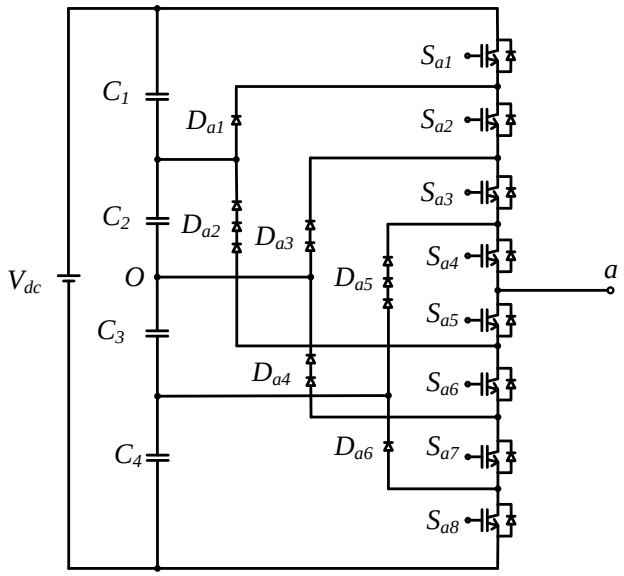

Figure 2.4: Circuit diagram of phase leg-*a* of the 5L-NPC inverter

The 3L-NPC inverter can be extended to higher levels [45, 46]. Figure 2.4 shows one phase leg of the five-level NPC (5L-NPC) inverter. The DC-link voltage is divided into five levels by four series connected capacitors $(C_1 - C_4)$. The voltage across the inverter output terminals *'a'* and the neutral point *'O'* can be $-V_{dc}/2, -V_{dc}/4, 0, V_{dc}/4$ and $V_{dc}/2$, depending on the switching combinations of $(S_{a1} - S_{a8})$, as tabulated in Table 2.2. For the 5L-NPC inverter, each switching device is only required to block one-fourth of the DC-link voltage. However, the clamping diodes have different reverse blocking voltage rating. For example, when $(S_{a4} - S_{a8})$ are turned on, the clamping diode D_{a2} has to block a voltage level of $3V_{dc}/4$, while D_{a1} only has to block a voltage

Switch combination								V_{aO}
S_{a1}	S_{a2}	S_{a3}	S_{a4}	S_{a5}	S_{a6}	S_{a7}	S_{a8}	
1	1	1	1	0	0	0	0	$V_{dc}/2$
0	1	1	1	1	0	0	0	$V_{dc}/4$
0	0	1	1	1	1	0	0	0
0	0	0	1	1	1	1	0	$-V_{dc}/4$
0	0	0	0	1	1	1	1	$-V_{dc}/2$

Table 2.2: Switching combinations for phase leg-*a* of the 5L-NPC inverter

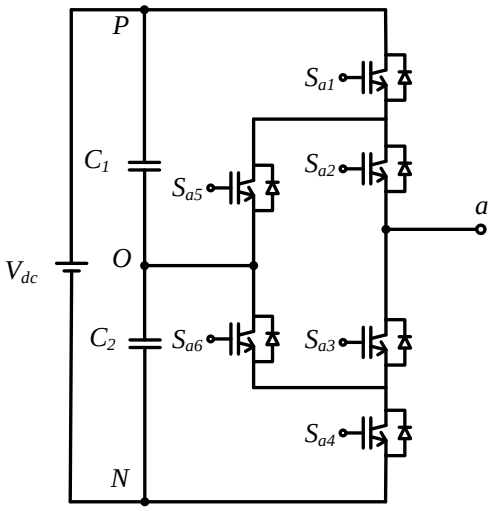

Figure 2.5: Circuit diagram of phase leg-*a* of the 3L-ANPC inverter

level of $V_{dc}/4$. Assuming that each clamping diode has the same blocking voltage rating as the switch device, the number of switching devices and clamping diodes in each phase leg of an *m*-level NPC inverter will be $2\,(m-1)$ and $(m-1)\,(m-2)$, respectively. It is apparent that when *m* is sufficiently high, the structure of the inverter becomes very complex with large number of semiconductor devices. Therefore, the level number for diode NPC topology never exceeds five in common industrial practice.

2.2.2 Active NPC Inverters

The three-level active NPC (3L-ANPC) inverter is presented in [47, 48]. Unlike the 3L-NPC inverter, the 3L-ANPC inverter uses clamping switches instead of clamping diodes, as shown in Figure 2.5. This modification allows the 3L-ANPC inverter to overcome the problem of unequal losses for each device in one phase leg of the 3L-NPC inverter. By driving the current go through the upper or lower clamping path, the symmetrical semiconductor-junction temperature distribution can be achieved [28]. This makes the cooling system design less complex and maximizes the power capability of the inverter. As a result, the 3L-ANPC inverter is able to achieve a higher power rate

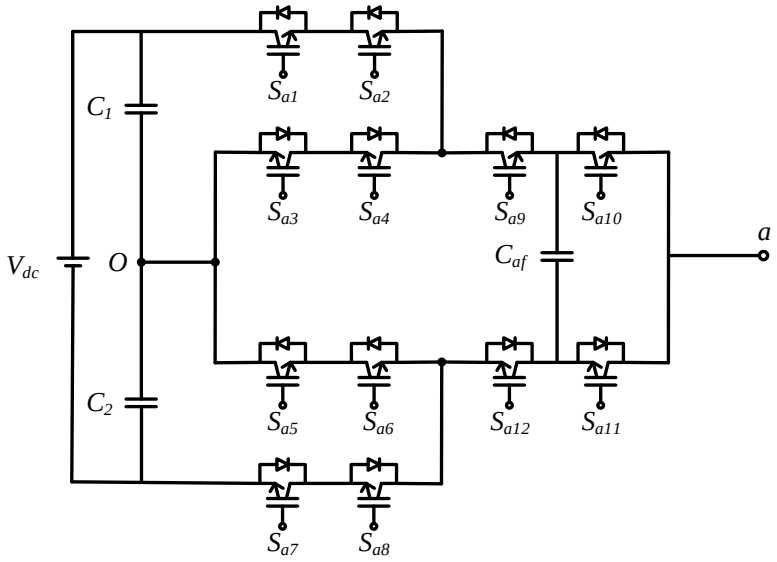

Figure 2.6: Circuit diagram of phase leg-a of the 5L-ANPC inverter

than the 3L-NPC inverter.

The 3L-ANPC inverter can also be extended to higher levels. For the m-level ANPC inverter, the number of switching devices in each phase leg is $m\,(m-1)$. Clearly, when the level number of the inverter is sufficiently high, a significant number of switching devices required will make the system impractical to implement. Therefore, the level number for ANPC topology also never exceeds five in common industrial practice.

The 3L-ANPC inverter can be combined with the three-level flying capacitor (3L-FC) inverter to form a five-level hybrid inverter [49, 50]. Despite the fact that it is a hybrid topology, it is commonly called 5L-ANPC inverter. A commercial version of this topology has been reported [51]. Figure 2.6 shows one phase leg of the 5L-ANPC inverter. From Figure 2.6, it is apparent that this topology requires fewer number of switching devices than the standard 5L-ANPC inverter. Nonetheless, this advantage come at the expense of a more complex current commutation loop during switching and unequal losses for each device in one phase leg. Moreover, the neutral point voltage and the floating capacitors voltage need to be controlled at the same time [28].

Switch combination								V_{aO}
S_{a1}, S_{a2}	S_{a3}, S_{a4}	S_{a5}, S_{a6}	S_{a7}, S_{a8}	S_{a9}	S_{a10}	S_{a11}	S_{a12}	
0	0	0	1	0	0	1	1	$-V_{dc}/2$
0	1	1	1	0	1	0	1	$-V_{dc}/4$
0	1	0	0	1	0	1	0	$-V_{dc}/4$
0	1	0	0	1	1	0	0	0
0	0	1	0	0	0	1	1	0
0	0	1	0	0	1	0	1	$V_{dc}/4$
1	0	0	0	1	0	1	0	$V_{dc}/4$
1	0	0	0	1	1	0	0	$V_{dc}/2$

Table 2.3: Switching combinations for phase leg-a of the 5L-ANPC inverter

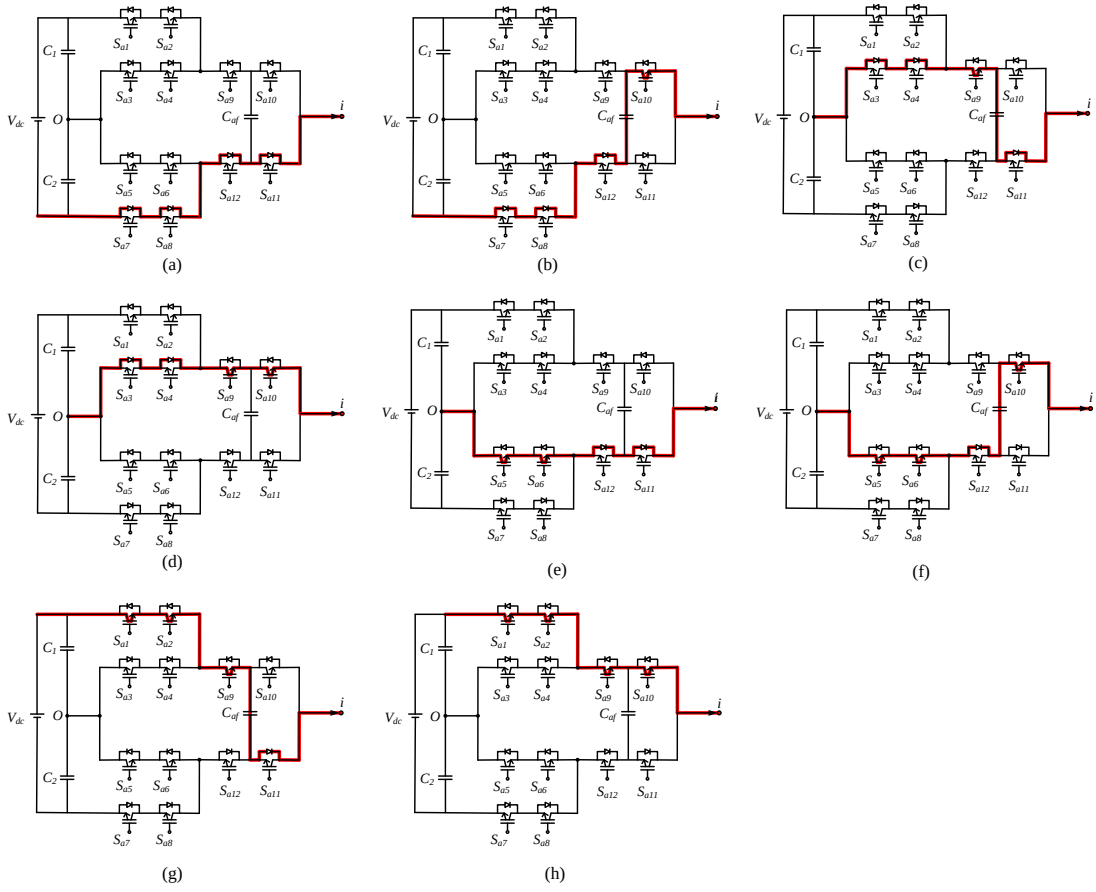

Figure 2.7: Current commutation during switching for positive output current of the 5L-ANPC inverter.

For the 5L-ANPC inverter, the floating capacitor C_{af} is initially charged to $V_{dc}/4$ while the two DC-link capacitors C_1 and C_2 are charged to $V_{dc}/2$. According to the switching

combinations of $(S_{a1} - S_{a11})$ tabulated in Table 2.3, the voltage across the inverter output terminal *'a'* and the neutral point *'O'* can be $-V_{dc}/2, -V_{dc}/4, 0, V_{dc}/4$ and $V_{dc}/2$. Therefore, the five-level output at the inverter output terminals can be produced. It is noteworthy that each phase leg of the 5L-ANPC inverter can produces eight switching states. Among them, two switching states generate the same voltage level of $-V_{dc}/4$, 0 and $V_{dc}/4$, respectively. These redundancies can be used to control the floating capacitor voltage. The switch commutation for each switching state for positive phase output current is depicted in Figure 2.7.

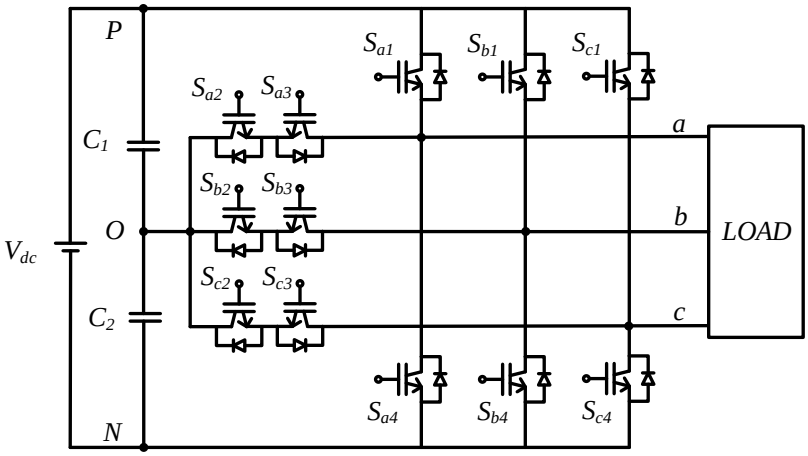

Figure 2.8: Circuit diagram of the T-type inverter.

2.2.3 T-type Inverter

Figure 2.8 shows the main circuit diagram of three-level T-type inverter. As shown in Figure 2.8, each phase leg of the T-type inverter consists of four switching devices along with their anti-parallel diodes. Compared to the 3L-NPC inverter, the T-type inverter uses the same number of active switching devices, but six fewer diodes and therefore reduces conduction losses. However, S_{x1} and S_{x4} have to block full DC-link voltage. S_{x2} and S_{x3}, which form a bidirectional switch connecting between the phase output terminal *'x'* $\{x \in (a, b, c)\}$ and neutral point *'O'*, have to block only half of the DC-link

Switching combination				V_{aO}
S_{x1}	S_{x2}	S_{x3}	S_{x4}	
1	1	0	0	$V_{dc}/2$
0	1	1	0	0
0	0	1	1	$-V_{dc}/2$

Table 2.4: Switching combinations in each phase leg of the T-type inverter

voltage. At each time instant, only two of the four switching devices in each phase leg are turned on. According to the switching combinations of $(S_{x1} - S_{x4})$ tabulated in Table 2.4, the possible voltage across the inverter output terminals *'x'* and the neutral point *'O'* can be $V_{dc}/2, -V_{dc}/2$ or 0. Therefore, the three-level output at the inverter output terminals (a, b, c) can be produced. The current commutation during switching for positive and negative output current in one phase leg of the T-type inverter is shown in Figure 2.9.

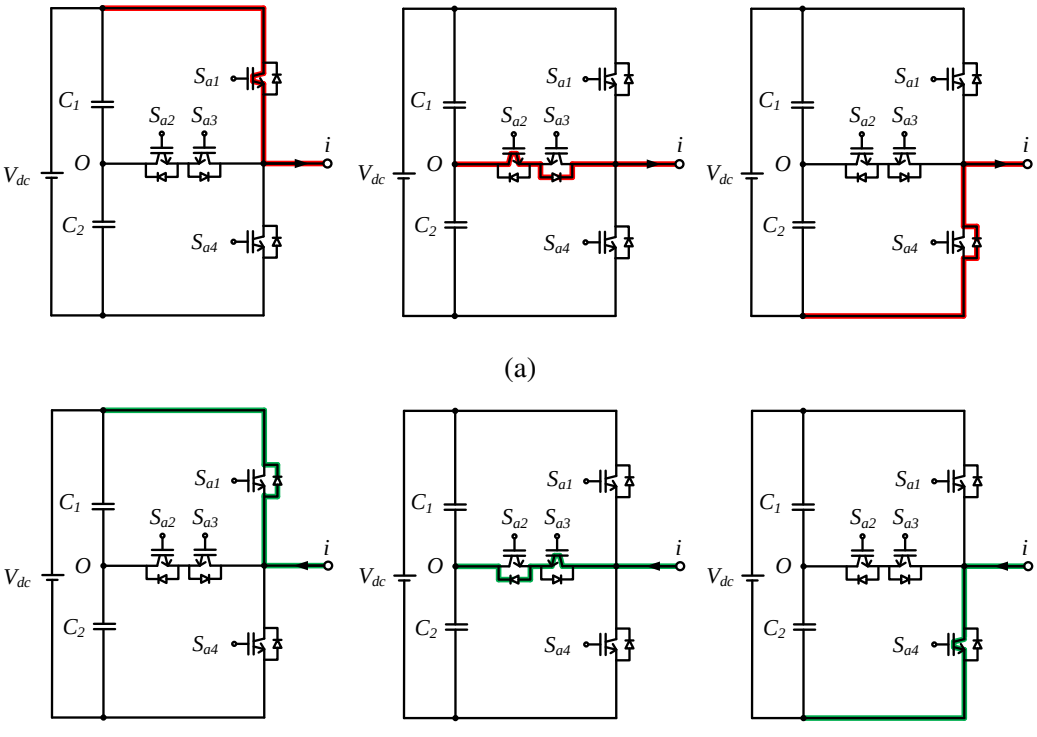

Figure 2.9: Current commutation during switching for (a) positive and (b) negative output current of the T-type inverter.

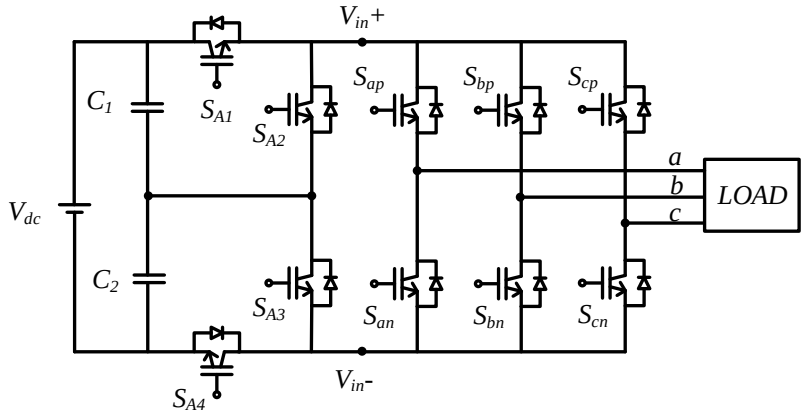

Figure 2.10: Circuit diagram of the 3L-SNPC inverter

The application of the T-type inverter for low-voltage motor drives has been recently reported in [29]. Experimental results show that the proposed drive system achieved better total efficiency compared to the conventional two-level inverter-fed motor drive solution. In addition, to further increase the total drive efficiency, the conduction losses of the switches and iron losses of the machine must be reduced.

2.2.4 Simplified NPC Inverter

The main circuit diagram of three-level simplified neutral point clamped (3L-SNPC) inverter [30] is illustrated in Figure 2.10. As shown in Figure 2.10, the 3L-SNPC inverter can be divided into two parts. The first part is a dual-buck converter, comprising two equal capacitors (C_1, C_2) and four switching devices $(S_{A1} - S_{A4})$ along with their anti-parallel diodes. Functionally, it splits the DC-link voltage into three levels $(V_{dc}/2, 0, -V_{dc}/2)$, allowing two voltage levels to be present at the input terminals $\left(V_{in}^{+}, V_{in}^{-}\right)$ at any instant. The switching logic of the dual-buck converter is tabulated in Table 2.5, from which it is apparent each switching device is only required to block half of the DC-link voltage.

Switching combination				**Terminal voltage**	
S_{A1}	S_{A2}	S_{A3}	S_{A4}	V_{in}^{+}	V_{in}^{+}
1	0	0	1	$V_{dc}/2$	$-V_{dc}/2$
1	0	1	0	$V_{dc}/2$	0
0	1	1	0	0	0
0	1	0	1	0	$-V_{dc}/2$

Table 2.5: Switching combination and terminal voltage of dual-buck converter

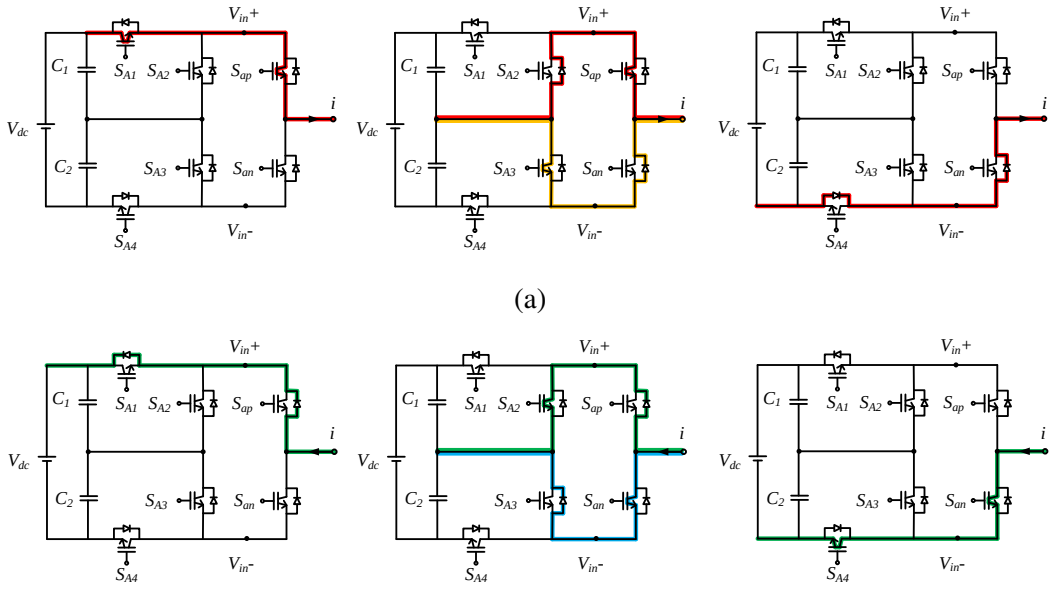

Figure 2.11: Current commutation during switching for (a) positive and (b) negative output current of the 3L-SNPC inverter.

The second part is a two-level inverter. It employs six switching devices, each capable of blocking the full DC-link voltage. Altogether, only ten switching devices are utilized, realizing an advantage relative to the T-type inverter. The two-level inverter fed by the dual-buck converter source produces the three-level output at the inverter output terminals (a, b, c). The current commutation during switching for positive and negative phase-a output current of the 3L-SNPC inverter is shown in Figure 2.11.

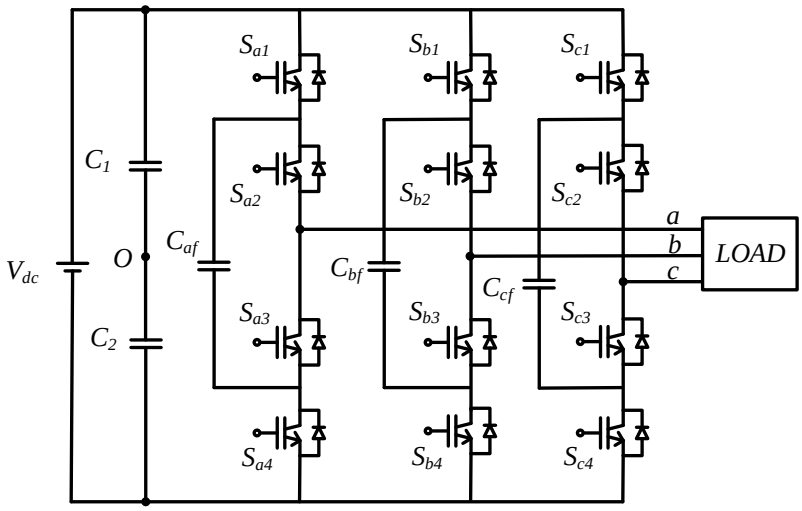

Figure 2.12: Circuit diagram of the 3L-FC inverter

2.3 Flying Capacitors Inverters

Figure 2.12 shows the main circuit of the three-level flying capacitor (3L-FC) inverter [35]. Each phase leg of the 3L-FC inverter consists of four switching devices along with their anti-parallel diodes and one floating capacitor to clamp the voltage. The floating capacitor is initially charged to $V_{dc}/2$. According to the switching combinations of $(S_{a1} - S_{a4})$ tabulated in Table 2.6, the possible voltage across the inverter output terminals *'a'* and the point *'O'* can be $V_{dc}/2, -V_{dc}/2$ or 0. Therefore, the three-level output at the inverter output terminals (a, b, c) can be produced.

The 3L-FC inverter does not have the DC-link capacitor voltages imbalance issue. However, the floating capacitor voltage must be maintained at $V_{dc}/2$. Figure 2.13 shows the current commutation during switching in one phase leg for positive and negative output current. From Figure 2.13, it can be seen that for positive output current the floating capacitor is charged when S_{a1} and S_{a3} are turned on, and is discharged when S_{a2} and S_{a4} are turned off. Therefore, the charge of the floating capacitor can be controlled through proper selection of the switch combination.

Switching combination				V_{aO}
S_{a1}	S_{a2}	S_{a3}	S_{a4}	
1	1	0	0	$V_{dc}/2$
1	0	1	0	0
0	1	0	1	0
0	0	1	1	$-V_{dc}/2$

Table 2.6: Switching combinations for phase leg-*a* of the 3L-FC inverter

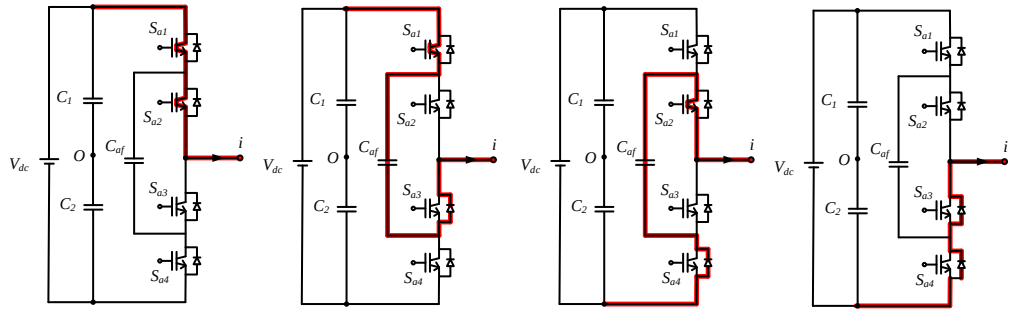

(a)

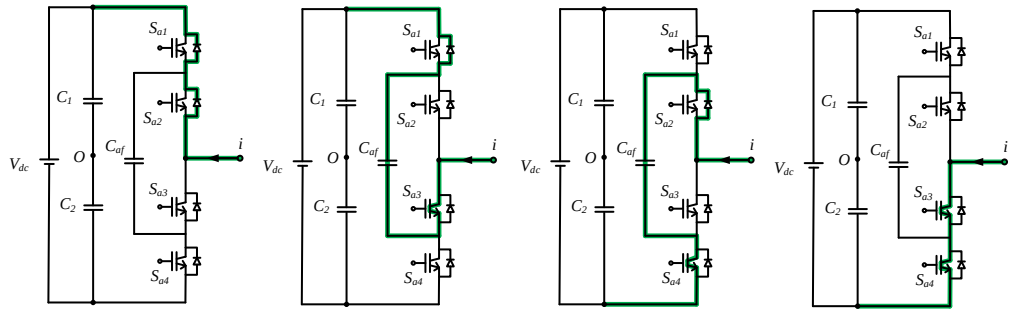

(b)

Figure 2.13: Current commutation during switching for (a) positive and (b) negative output current of the 3L-FC inverter.

The 3L-FC inverter can be extended to higher levels. Figure 2.14 shows one phase leg of the five-level flying capacitor (5L-FC) inverter. The voltage across the inverter output terminal *'a'* and the neutral point *'O'* can be $-V_{dc}/2$,$-V_{dc}/4$, 0, $V_{dc}/4$ and $V_{dc}/2$, depending on the switching combinations of $(S_{a1} - S_{a8})$, as tabulated in Table 2.7. Compared to the 5L-NPC and 5L-ANPC inverters, the 5L-FC inverter has more redundant switching combinations. By proper selection of switching combinations, it is possible to control the clamping capacitor charge. However, assuming that each

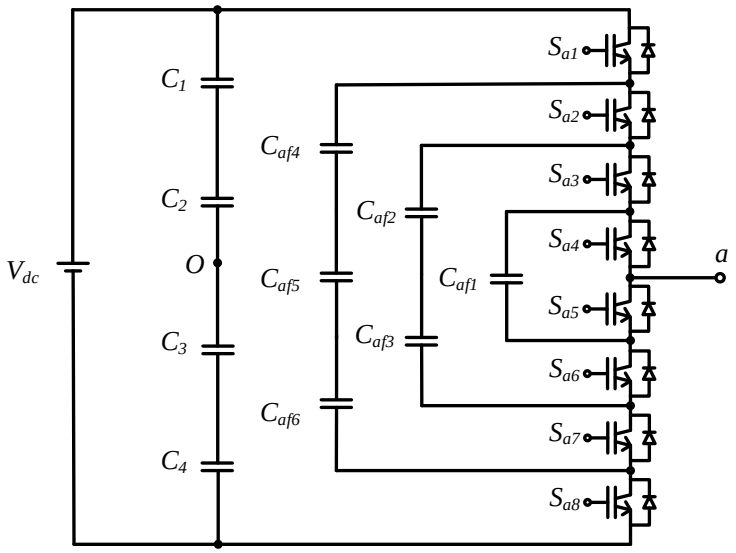

Figure 2.14: Circuit diagram of the 5L-FC inverter

capacitor has the same blocking voltage rating as the switch device, each phase leg of an *m*-level FC inverter requires a total number of $(m-1)(m-2)$ clamping capacitors and $(m-1)$ DC-link capacitors. It can be seen that when *m* is sufficiently high, the structure of the inverter becomes very complex with large number of devices.

Switch combination								V_{aO}
S_{a1}	S_{a2}	S_{a3}	S_{a4}	S_{a5}	S_{a6}	S_{a7}	S_{a8}	
1	1	1	1	0	0	0	0	$V_{dc}/2$
1	1	1	0	1	0	0	0	$V_{dc}/4$
1	0	1	1	0	0	1	0	$V_{dc}/4$
0	1	1	1	0	0	0	1	$V_{dc}/4$
1	0	1	1	0	0	1	0	0
1	0	0	1	0	1	1	0	0
1	1	0	0	1	1	0	0	0
0	1	1	0	1	0	0	1	0
0	1	0	1	0	1	0	1	0
0	0	1	1	0	0	1	1	0
1	0	0	0	1	1	1	0	$-V_{dc}/4$
0	0	1	0	1	0	1	1	$-V_{dc}/4$
0	0	0	1	0	1	1	1	$-V_{dc}/4$
0	0	0	0	1	1	1	1	$-V_{dc}/2$

Table 2.7: Switching combinations for phase leg-*a* of the 5L-FC inverter

Compared to NPC inverters, FC inverters have found less industrial penetration. This is mainly because a higher switching frequency are necessary to keep the capacitors properly balanced [28]. In addition, this topology also requires initialization of the floating capacitor voltages.

2.4 Cascaded Inverters

The cascaded multilevel inverter is suitable for high-power applications due to its modular structure that allows higher voltage operation with low-voltage semiconductor devices. It can be classified into three categories: symmetrical cascaded H-bridge, asymmetrical cascaded H-bridge and modular.

The symmetrical cascaded H-bridge (CHB) inverter topology [52, 53] is based on the series connection of single phase H-bridge inverters with separate DC sources. The required inverter pole voltage can be synthesized by the addition of the voltage generated by the different cells. If each phase leg has *N* cells, the symmetrical CHB inverter can produces $(2N + 1)$ voltage levels. Consider a five-level symmetrical CHB shown in Figure 2.15-(a) as an example. This topology consists of two series-connected single phase H-bridge inverters with two separate DC sources. The inverter produces five voltage levels $2V_{dc}$, V_{dc}, 0, $-V_{dc}$ and $-2V_{dc}$ across the inverter output terminals *'a'* and the point *'O'*, depending on the switching combinations of $(S_{a1} - S_{a8})$.

The asymmetrical CHB inverter is proposed in [54]. This topology has a very similar structure compared to the symmetrical CHB inverter. The only difference is that each single phase H-bridge cell in one phase leg has different voltage levels, as shown in Figure 2.15-(b). With N cells in one phase leg, the asymmetrical CHB produces $\left(2^{N+1} - 1\right)$ voltage levels. Thus with the same number of cells, the asymmetrical CHB produces more voltage levels than the symmetrical CHB inverter. However, due to the

difference in DC source supply to each cell, the device rating for each cell is different.

Another topology is the modular inverter [55], as shown in Figure 2.16. This topology consists of series-connected two-level single-phase half-bridge along with their parallel floating capacitor. Further, H-bridge cells have been proposed [53, 56, 57]. With *N* cells in one phase leg (*N* must be even), the modular inverter produces $(2N - 1)$ voltage levels at the inverter output terminals. Unlike the CHB inverters, the modular inverter does not require isolated DC sources. However, the floating capacitors voltage balance need to be controlled.

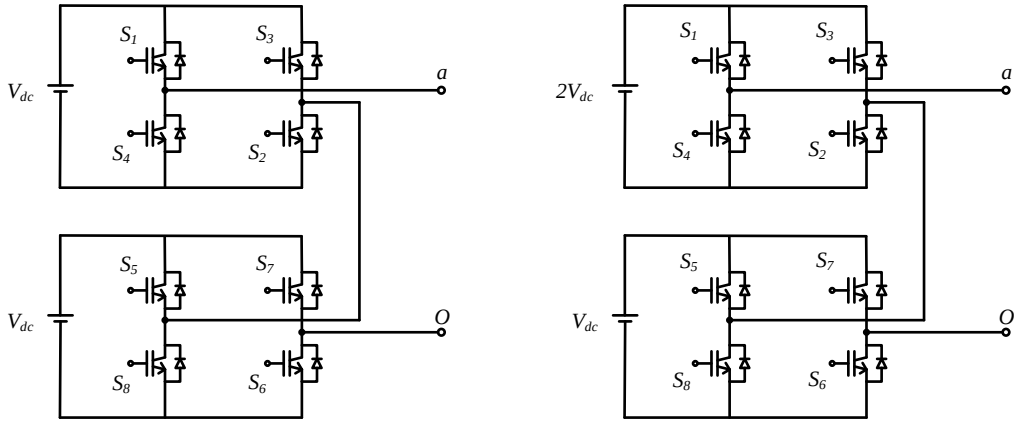

Figure 2.15: Circuit diagram of the (a) symmetrical CHB, and (b) asymmetrical CHB inverters.

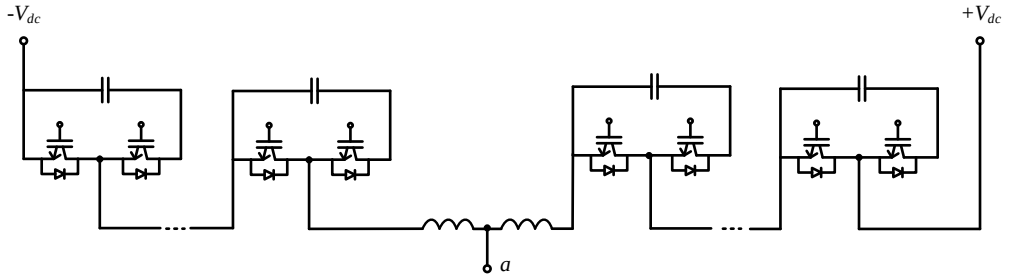

Figure 2.16: Circuit diagram of the modular inverter

2.5 Comparison between the 3L-NPC, T-type and 3L-SNPC inverters

2.5.1 Number of components

Table 2.8 shows the comparison between the 3L-NPC, T-type and 3L-SNPC inverters. It can be seen that the 3L-NPC inverter has highest total number of semiconductor devices and each active switch has to block only half of the DC-link voltage. In contrast, the total number of devices is smallest for the 3L-SNPC inverter. Compared to the T-type inverter, 3L-SNPC inverter has the same number of active switches that have to block full DC-link voltage, but less number of switches that have to block half of the DC-link voltage. Therefore, this feature makes the 3L-SNPC inverter very suitable for EV applications. The issue of neutral point voltage imbalance for NPC inverters are investigated in the next section.

Description	3L-NPC	T-type	3L-SNPC
Number of DC-link capacitor	2	2	2
Number of active switch	12	12	10
Number of passive switch	18	12	10
Number of switch that has to block $V_{dc}/2$	12	6	4
Number of switch that has to block V_{dc}	0	6	6

Table 2.8: A comparison between 3L-NPC, T-type and 3L-SNPC inverters

2.5.2 Neutral Point Voltage Balancing

The operating status of the switching devices can be represented by switching states. A switching state POO denotes that the output terminal *'a'* is connected to the point *'P'* while the output terminals *'b'* and *'c'* are connected to the point *'O'* . The 3L-SNPC has twenty-one switching states, as shown in Table 2.9. The terminal phase voltages

No.	Switching states			Output phase voltages			Voltage space vectors		
				V_{an}	V_{bn}	V_{cn}	Mag.	Angle	Vector
I	Zero voltage vectors								
1	P	P	P	0	0	0	0	0	0
2	O	O	O						
3	N	N	N						
II	Small voltage vectors								
4	P	O	O	$V_{dc}/3$	$-V_{dc}/6$	$-V_{dc}/6$	$V_{dc}/3$	0	V_{S1}
5	O	N	N						
6	P	P	O	$V_{dc}/6$	$V_{dc}/6$	-$V_{dc}/3$	$V_{dc}/3$	$\pi/3$	V_{S2}
7	O	O	N						
8	O	P	O	-$V_{dc}/6$	$V_{dc}/3$	$-V_{dc}/6$	$V_{dc}/3$	$2\pi/3$	V_{S3}
9	N	O	N						
10	O	P	P	-$V_{dc}/3$	$V_{dc}/6$	$V_{dc}/6$	$V_{dc}/3$	π	V_{S4}
11	N	O	O						
12	O	O	P	-$V_{dc}/6$	-$V_{dc}/6$	$V_{dc}/3$	$V_{dc}/3$	$-2\pi/3$	V_{S5}
13	N	N	O						
14	P	O	P	$V_{dc}/6$	-$V_{dc}/3$	$V_{dc}/6$	$V_{dc}/3$	$-\pi/3$	V_{S6}
15	O	N	O						
III	Large voltage vectors								
16	P	N	N	$2V_{dc}/3$	$-V_{dc}/3$	$-V_{dc}/3$	$2V_{dc}/3$	0	V_{L1}
17	P	P	N	$V_{dc}/3$	$V_{dc}/3$	$-2V_{dc}/3$	$2V_{dc}/3$	$\pi/3$	V_{L2}
18	N	P	N	$-V_{dc}/3$	$2V_{dc}/3$	$-V_{dc}/3$	$2V_{dc}/3$	$2\pi/3$	V_{L3}
19	N	P	P	$2V_{dc}/3$	$V_{dc}/3$	$V_{dc}/3$	$2V_{dc}/3$	π	V_{L4}
20	N	N	P	$-V_{dc}/3$	$-V_{dc}/3$	$2V_{dc}/3$	$2V_{dc}/3$	$-2\pi/3$	V_{L5}
21	P	N	P	$V_{dc}/3$	$2V_{dc}/3$	$V_{dc}/3$	$2V_{dc}/3$	$-\pi/3$	V_{L6}

Table 2.9: Switching state combinations of 3L-SNPC inverter

corresponding to each switching state combination can be represented by a voltage space vector using the following transformation

$$\vec{V} = \frac{2}{3}\left(V_{an} + V_{bn}e^{j\frac{2\pi}{3}} + V_{cn}e^{j\frac{4\pi}{3}}\right) \tag{2.1}$$

Based on magnitude, the voltage vectors can be divided into three groups: zero voltage vectors (V_0) , small voltage vectors (V_{Si}) and large voltage vectors (V_{Li}), as shown in Figure 2.17.

For the 3L-SNPC inverter, there are two possible ways to produce a given V_{Si}. For

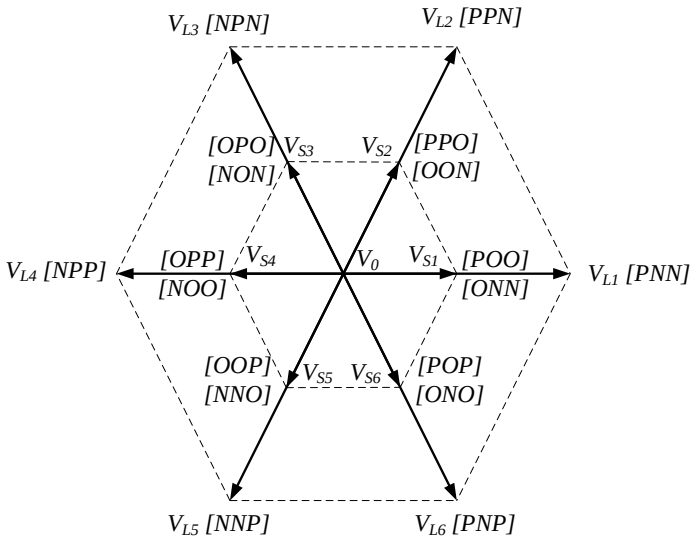

Figure 2.17: Space voltage vectors diagram of the 3L-SNPC

example, the switching state POO and OON are both represented by V_{S1}. The former is produced when the phase *'a'* leg of the two-level inverter is connected to $+V_{dc}/2$, while both phase *'b'* and *'c'* legs are connected to *'O'* . Conversely, the latter is produced, if the phase *'a'* leg of the two-level inverter is connected *'O'* , while both phase *'b'* and *'c'* legs are connected to $-V_{dc}/2$. These two switching states also produce opposite effect on the neutral point voltage. The medium voltage vectors that are present for the 3L-NPC and T-type, do not exist for the 3L-SNPC inverter. This reduces neutral point voltage fluctuations, since medium voltage vectors are known as the main source of this problem [58]. The small voltage vector can be divided into two groups: Group I, including switching states $(POO, PPO, OPO, OPP, OOP, POP)$ and Group II, including switching states $(ONN, OON, NON, NOO, NNO, ONO)$, each of which have opposite effects on the charging and discharging of capacitors C_1 and C_2, as illustrated in Figure 2.18. It is also noted that different V_{Si} produce different neutral point currents, as shown in Table 2.10.

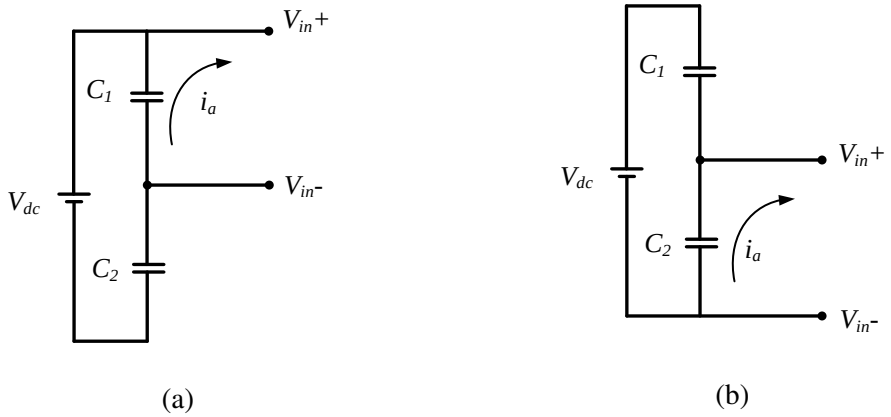

Figure 2.18: Effect on the voltages of capacitors C_1 and C_2 due to switching states (a) POO and (b) ONN.

Voltage space vector	Switching state	Neutral point current
V_{S1}	POO	$-i_a$
	ONN	i_a
V_{S2}	PPO	i_c
	OON	$-i_c$
V_{S3}	OPO	$-i_b$
	NON	i_b
V_{S41}	OPP	i_a
	NOO	$-i_a$
V_{S5}	OOP	$-i_c$
	NNO	i_c
V_{S6}	POP	i_b
	ONO	$-i_b$

Table 2.10: Neutral point current for different V_{Si}

Compared to the 3L-SNPC inverter, T-type and 3L-NPC inverters are able to generate more switching states. Each topology has twenty-seven switching states that can be devided into four groups based on their magnitude: zero voltage vectors (V_0) , small voltage vectors (V_{Si}), medium voltage vectors (V_{Mi}) and large voltage vectors (V_{Li}), as shown in Figure 2.19.

For the T-type and 3L-NPC inverters, V_{Si} and V_{Mi} affect the neutral point balance. Each V_{Mi} can be generated from only one switching state. Therefore, to balance the neutral

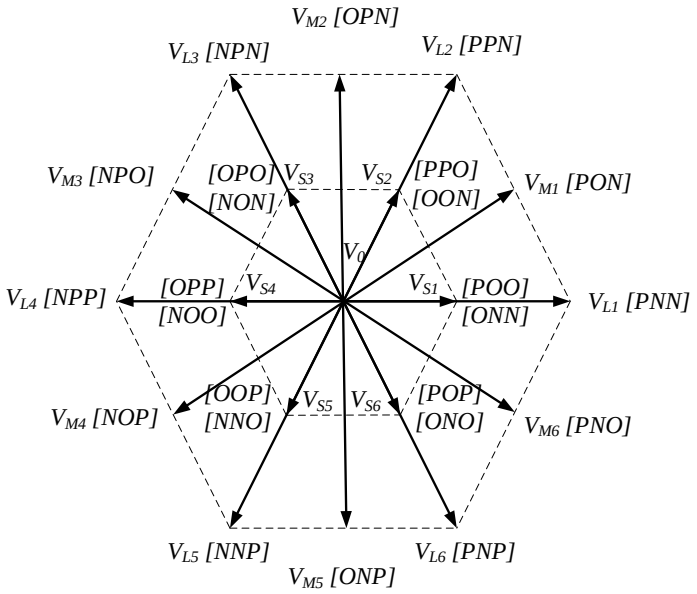

Figure 2.19: Space voltage vectors diagram of the 3L-NPC

point voltage, appropriate combination of switching states must be selected in such a way that the average neutral point current in a duty cycle equals to zero [59]. However, the neutral point current (i_0) caused by V_{Mi} cannot be completely compensated by i_0 generated by V_{Si}, especially at high modulation index and low power factors [58, 59]. Thus, the issue of neutral point voltage imbalance of the T-type and 3L-NPC inverters is more severe than that of the 3L-SNPC inverter.

2.6 Conclusion

A brief review of multilevel topologies for motor drive applications was presented in this chapter. A comparison between the 3L-NPC, 3L-SNPC and T-type inverters was carried out to highlight the advantages of the 3L-SNPC inverter for EV applications. It is also noteworthy that the performance shortcoming of the 3L-SNPC inverter is due to the lack of medium voltage vectors. For example, the conventional SVM method

cannot be applied and, therefore, the existing SVM based-control algorithms for 3L-NPC and T-type inverters-fed IPMSM drive cannot be applied without difficulty and compromise. This issue has been addressed only in [102]. So far, very little research on suitable control strategies for 3L-SNPC inverter-fed IPMSM drive has been presented in literature. This thesis presents several control strategies suited to the 3L-SNPC inverter. In the next chapter, a duty-cycle-control-based DTC is proposed.

Chapter 3

A Duty-cycle-Control-Based DTC Strategy for the 3L-SNPC Inverter-fed IPMSM Drives

3.1 Introduction

A technique providing robustness against machine parameter variations while maintaining fast dynamic response and control structure simplicity is the direct torque control (DTC) strategy [7, 8]. DTC requires neither the SVM block, nor current controllers. Rather, the torque and stator flux are directly regulated by selecting appropriate voltage vectors from a switching table. In addition, the use of hysteresis control facilitates fast torque and stator flux dynamics. Nevertheless, this leads to high torque ripples and a variable switching frequency. A number of modified DTC strategies have been proposed to overcome these drawbacks.

In [60], a SVM-based DTC (SVM-DTC) method is proposed to reduce torque ripple while operating at a constant switching frequency. The magnitude and angle of the

desired voltage vector are calculated from knowledge of the torque and stator flux errors. The desired voltage vector is then synthesized using SVM. The reported experimental results indicate improvements in the torque and stator flux ripple levels. Alternatively, the desired voltage vector can be determined on the basis of the deadbeat control [13]. Akin to the SVM-DTC, a constant switching frequency is attained. Another commonly used method is the predictive DTC in which the desired voltage vector may be calculated to achieve the minimum torque ripple [17]. However, the fixed duration of the desired voltage vector is a drawback, as it limits the reduction in torque ripple that can be attained. An improvement in this respect is proposed in [18, 20] by varying the duration of the applied voltage vector. Experimental results show a significant reduction in torque ripple compared to the method in [17]. Although SVM-DTC and predictive DTC mitigate the aforementioned drawbacks of the conventional DTC, the control structure complexity and machine parameter dependency are unavoidably increased [9]. Duty cycle control method addresses both these issues.

The duty cycle control method for PMSM drives proposed in [9, 10] employs one active voltage vector in conjunction with a zero voltage vector within each sampling cycle to attain torque ripple reduction. The duration of active voltage vector is calculated from the knowledge of the rate of torque variation using various optimization techniques. However, this method necessitates operation at a variable switching frequency. In [61, 62], a modified DTC strategy is proposed to obtain torque ripple reduction at a constant switching frequency. An additional PI torque controller is required to regulate the duration of the applied voltage vector. Thus, the drive performance strongly depends on the selection of PI controller gains.

More recent research has focused on the implementation of DTC with multilevel inverters [12, 63, 64]. Very precise control can be realized through increasing the number of voltage vector selections available, thus reducing the torque and stator flux

ripple [65]. In [30], the 3L-SNPC inverter uses fewer switching devices than the T-type inverter [29, 66], while maintaining a multilevel output. Therefore, it is comparatively advantageous in low-voltage drive applications for which low harmonic distortion in the current output waveforms is required. Moreover, the medium voltage vectors, which are the major source of neutral point capacitor voltage imbalance for the T-type inverter [67, 68], do not exist. This results in lower neutral point voltage fluctuations, improving the motor drive performance. However, experimental validation of the torque ripple minimization of a DTC controlled IPMSM driven by a 3L-SNPC inverter has not been reported.

This chapter proposes a novel strategy that is suited to the 3L-SNPC inverter. A DTC based switching table strategy employing two voltage vectors within each sampling cycle is proposed to reduce the torque ripple without incurring higher dv/dt levels. Furthermore, the issue of neutral point capacitor voltage imbalance is addressed.

This chapter is organized as follows. The mathematical model of IPMSM and analysis of the effect of stator voltage on the torque variation are presented in section 3.2. The proposed DTC strategy is developed in section 3.3. Experimental results in section 3.4 show the effectiveness of the proposed strategy, and section 3.5 provides concluding observations.

3.2 The Effect of Stator Voltage on the Torque Variation

The stator current, stator flux linkage and rotor flux linkage can be presented in the rotor $(d-q)$ and stator flux $(x-y)$ reference frames, as shown in Figure 3.1. In the $(x-y)$ reference frame, the machine voltage equations and electromagnetic torque are given by

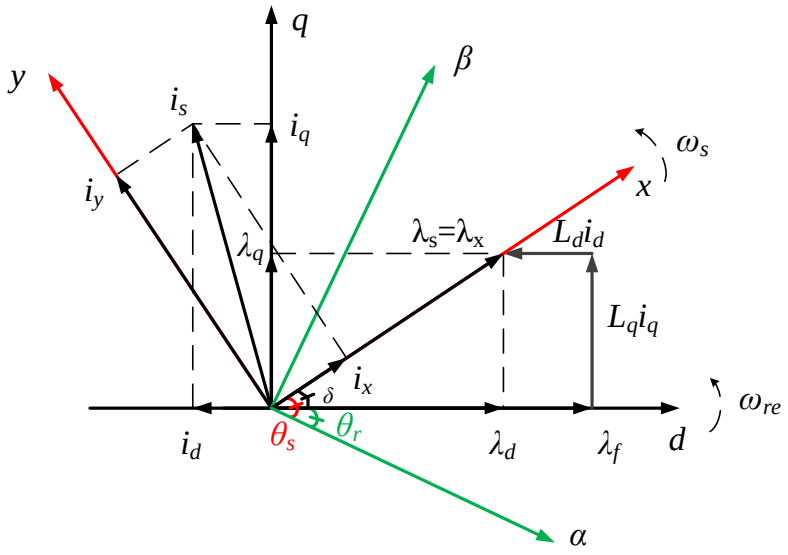

Figure 3.1: Phasor diagram of the stator current and flux linkage in the $(d-q)$ and $(x-y)$ reference frames

$$v_x = R_s i_x + \frac{d\lambda_s}{dt} \tag{3.1}$$

$$v_y = R_s i_y + \lambda_s \omega_s \tag{3.2}$$

$$T_e = \frac{3P}{2} \lambda_s i_y \tag{3.3}$$

where R_s stator resistance

λ_s stator flux linkage

ω_s speed of the stator flux linkage vector

v_x, v_y stator voltages in the $xy-$axes

i_x, i_y stator currents in the $xy-$axes

T_e electromagnetic torque

P number of pole pairs

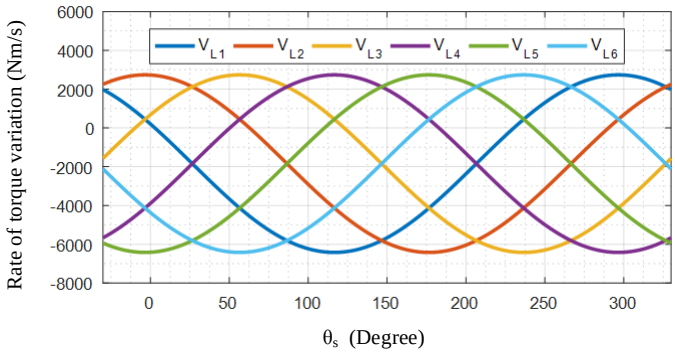

Figure 3.2: Torque variation rate corresponding to V_{Li}

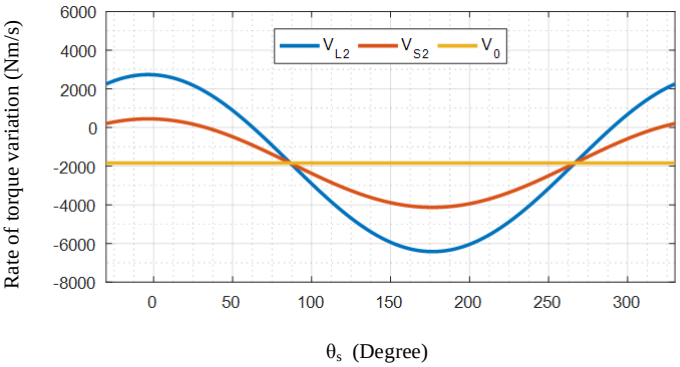

Figure 3.3: Torque variation rate corresponding to V_{Li}, V_{Si} and V_0

The rate of torque variation can be derived from (3.1), (3.2) and (3.3) as:

$$\frac{T_e}{dt} = -\frac{R_s}{L_q}T_e - \frac{3P}{2L_q}\lambda_s\lambda_a \cos\delta\omega_{re} + \frac{3P}{2L_q}\left(\lambda_a \sin\delta v_x + \lambda_a \cos\delta v_y\right) \tag{3.4}$$

where L_d, L_q are the $dq-$ axis inductances, δ is the load angle, $\lambda_a = \lambda_f + (L_d - L_q)i_d$ and is termed as the active flux [69], i_d is the $d-$ axis stator current, λ_f is the permanent magnet flux linkage and ω_{re} is the electrical speed of rotor.

From (3.4), the rate of torque variation is dependent on three terms. The first two terms on the right hand side, which are proportional to the instantaneous torque and rotor electrical speed respectively are always negative. The third term reflects the effect of

stator voltage on the torque variation rate. The rate of torque variation of the IPMSM operating corresponding to different voltage vectors are illustrated in Figures 3.2 and 3.3. It can be observed from these graphs that the rate of torque variation corresponding to V_0 is always negative. In other words, the torque will always decrease whenever V_0 is applied. Furthermore, due to the first two terms on the right hand side of (3.4), the maximum rate of torque reduction is always greater than that of torque increase, regardless of the applied voltage vector. In addition, it can be inferred from Figures 3.2 and 3.3 that if a single voltage vector is applied over the entire sampling cycle, significant torque variations will occur.

3.3 The Proposed DTC Strategy

The block diagram of the proposed DTC strategy is shown in Figure 3.4. The torque and stator flux are estimated from the measured stator currents. The torque and flux error are then calculated and fed to the hysteresis controllers. With the outputs of the torque and flux hysteresis controllers, appropriate voltage vectors will be selected from the switching table. The torque and stator flux are therefore directly controlled to keep the torque and flux error within the hysteresis bands. In order to reduce the torque ripples, a DTC strategy employing two voltage vectors within each sampling cycle is implemented. The duration of each applied voltage vector is determined from the duty cycle calculation block. The speed of the machine is measured, and a PI controller which outputs the torque reference is used for the outer speed control loop. In this section, the key aspects of proposed system are described.

3.3.1 Switching Table

The stator voltage equation of an IPMSM in the stationary $(\alpha - \beta)$ reference frame is given by

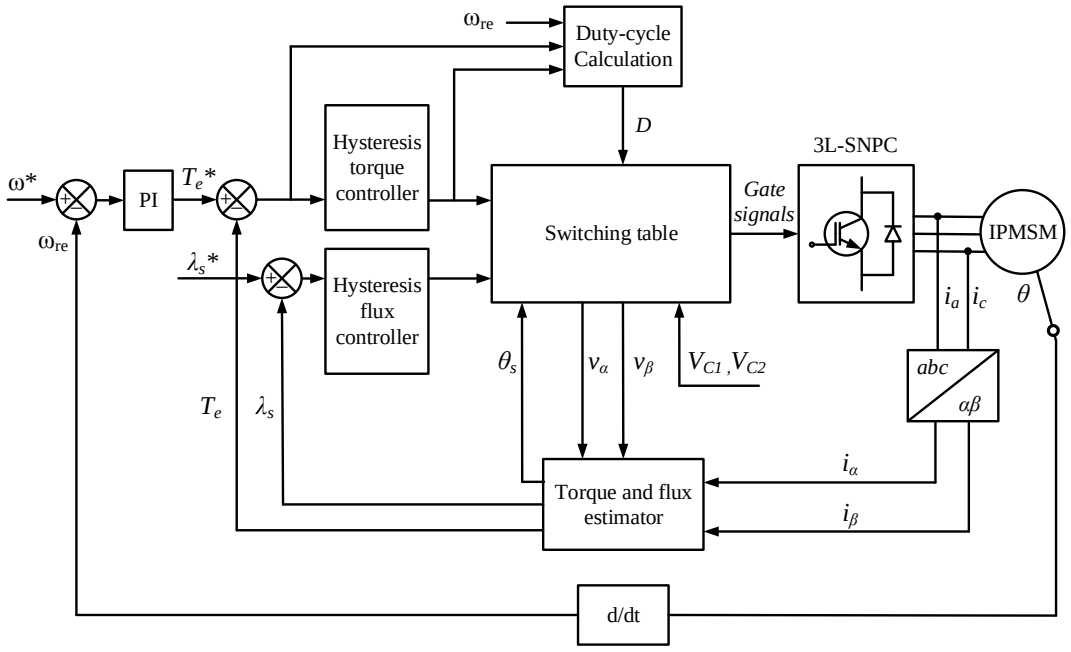

Figure 3.4: Block diagram of the proposed duty-cycle-control-based DTC strategy

$$\boldsymbol{v_s} = R_s \boldsymbol{i_s} + \frac{d\boldsymbol{\lambda_s}}{dt} \tag{3.5}$$

where $\boldsymbol{v_s}$, $\boldsymbol{i_s}$ and $\boldsymbol{\lambda_s}$ are the stator voltage, current and flux linkage vectors in the stationary $(\alpha - \beta)$ reference frame.

The stator flux linkage then can be derived as

$$\boldsymbol{\lambda_s} = \boldsymbol{v_s} t - R_s \int i_s dt + \boldsymbol{\lambda_s}|_{t=0} \tag{3.6}$$

where $\boldsymbol{\lambda_s}|_{t=0}$ is the initial stator flux linkage. Equation (3.6) implies that the tip of the stator flux linkage vector $\boldsymbol{\lambda_s}$ will move in the same direction as the applied voltage vector, if the stator resistance is neglected. The magnitude of $\boldsymbol{\lambda_s}$ can be increased or decreased by selecting an appropriate voltage vector, depending on its direction of rotation. This is illustrated in Figure 3.6.

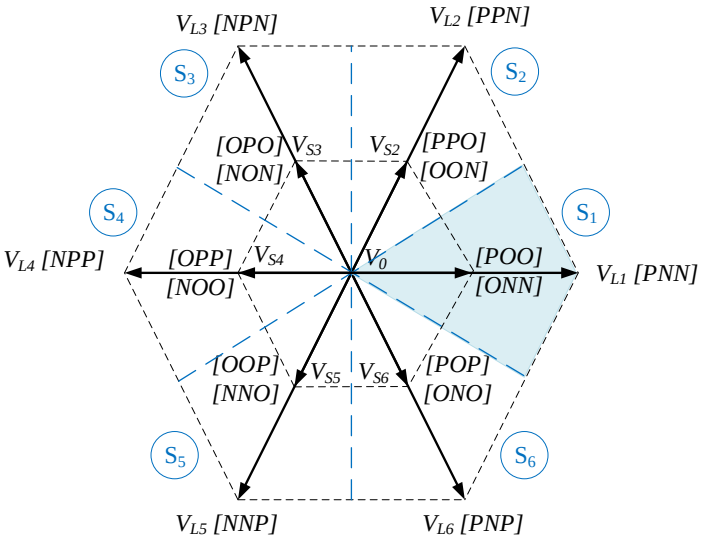

Figure 3.5: Six sectors of the voltage vector diagram

On the other hand, the electromagnetic torque can be expressed in terms of load angle δ, which is the angle between stator flux linkage and rotor flux linkage as

$$T_e = \frac{3P}{4L_dL_q}\lambda_s \left[2L_q\lambda_f \sin\delta - (L_q - L_d)\,\lambda_s \sin 2\delta\right] \tag{3.7}$$

This equation suggests that if the magnitude of stator flux linkage is kept constant, the developed torque can be regulated by varying the load angle δ. In other words, the electromagnetic torque can be controlled by controlling the angular position of the stator flux linkage vector. The load angle can be easily changed due to the fact that the mechanical time constant is much greater than the electrical time constant.

Based on the above analysis, the proposed switching table can be developed. By applying an appropriate voltage vector, the stator flux linkage vector can be regulated in such a way that the amplitude is maintained constant while the torque is controlled by varying the angle between the stator flux vector and rotor flux vector.

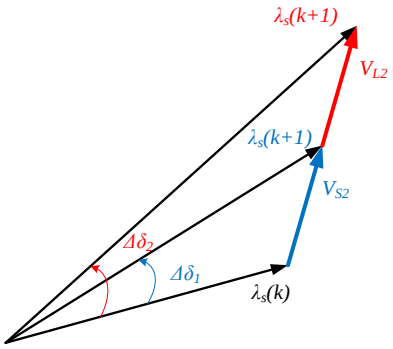

Figure 3.6: Effect of the application of V_{Li} and V_{Si} on the stator flux in case of torque and flux increase

The voltage space vector of 3L-SNPC inverter can be divided into six equal sectors, S_1 to S_6, of 60^0 each, as shown in the Figure 3.5. Sector S_1 spans from -30^0 to 30^0 of the voltage vector diagram. Depending on the torque and stator flux errors, an appropriate voltage vector can be selected. For example, if both torque and stator flux are smaller than the reference value, the voltage vector that increases the amplitude of torque and stator flux will be chosen. Figure 3.6 depicts the effect of the application of large and small voltage vectors on the stator flux in case of torque and flux increase when the stator flux vector $\boldsymbol{\lambda_s}$ lies in sector S_1 and is rotating counter-clockwise. A large voltage vector V_{L2} will be selected if a large increase in torque is required. Conversely, a small voltage vector V_{S2} will be selected if a small increase in torque is required. Once the torque exceeds its reference value, and if the stator flux needs to be increased, voltage vector V_{L6} or V_{S6} is selected to rotate the stator flux vector in the opposite direction, thus reducing the load angle δ and electromagnetic torque T_e.

As mentioned in the preceding section, the high torque ripple of the DTC is a consequence of the application of only one voltage vector within an entire sampling cycle [9]. By applying a non-zero voltage vector in conjunction with a zero-voltage vector, V_0 within the sampling cycle, the torque ripple is reduced. This technique has

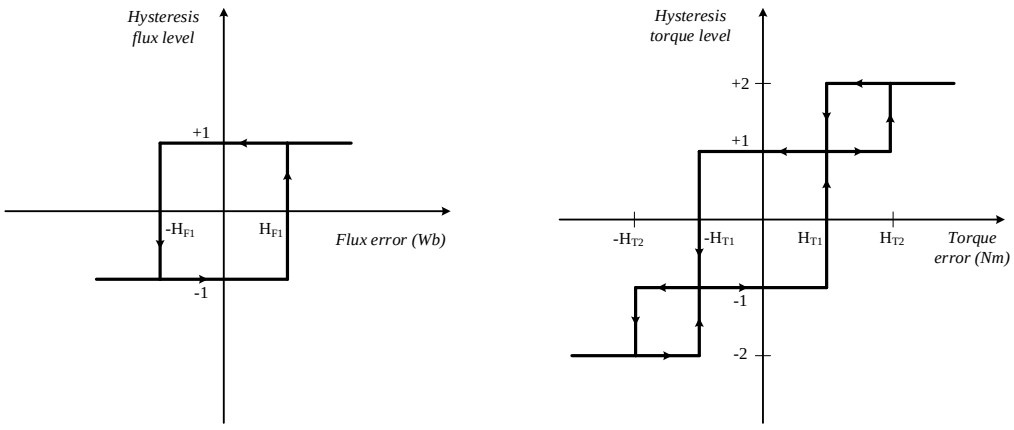

(a) (b)

Figure 3.7: A two-level flux hysteresis controller (a) and a four-level torque hysteresis controller (b).

previously been employed for DTC two-level inverter fed drives [9, 10]. However, and disadvantageously, the direct application of this method to multilevel inverters necessitates higher dv/dt levels, negating the benefits of multilevel inverters [35]. To overcome this issue, modified method is proposed in this paper. This is achieved by restricting the number of allowed voltage vector combinations for any given sampling cycle. Only two possible combinations are allowed: V_{Li} with V_{Si}, and V_{Si} with V_0. Furthermore, the switching pattern always begins and ends with a V_{Si} to enable a transition to adjacent voltage vectors without incurring a high dv/dt level.

Based on the foregoing analysis, a two-level flux hysteresis controller and a four-level torque hysteresis controller as shown in Figure 3.7, which allows for the utilization of all voltage vectors, is proposed. The proposed switching table for the proposed DTC drive is shown in Table 3.1. λ and τ are the hysteresis flux and torque levels respectively. $\lambda = +1$ indicates that the estimated flux is smaller than its reference value and vice versa. The same thing applies to τ.

λ	τ	**Sector**					
		S_1	S_2	S_3	S_4	S_5	S_6
+1	+2	V_{L2}, V_{S2}	V_{L3}, V_{S3}	V_{L4}, V_{S4}	V_{L5}, V_{S5}	V_{L6}, V_{S6}	V_{L1}, V_{S1}
	+1	V_{S2}, V_0	V_{S3}, V_0	V_{S4}, V_0	V_{S5}, V_0	V_{S6}, V_0	V_{S1}, V_0
	-1	V_{S6}, V_0	V_{S1}, V_0	V_{S2}, V_0	V_{S3}, V_0	V_{S4}, V_0	V_{S5}, V_0
	-2	V_{L6}, V_{S6}	V_{L1}, V_{S1}	V_{L2}, V_{S2}	V_{L3}, V_{S3}	V_{L4}, V_{S4}	V_{L5}, V_{S5}
-1	+2	V_{L3}, V_{S3}	V_{L4}, V_{S4}	V_{L5}, V_{S5}	V_{L6}, V_{S6}	V_{L1}, V_{S1}	V_{L2}, V_{S2}
	+1	V_{S3}, V_0	V_{S4}, V_0	V_{S5}, V_0	V_{S6}, V_0	V_{S1}, V_0	V_{S2}, V_0
	-1	V_{S5}, V_0	V_{S6}, V_0	V_{S1}, V_0	V_{S2}, V_0	V_{S3}, V_0	V_{S4}, V_0
	-2	V_{L5}, V_{S5}	V_{L6}, V_{S6}	V_{L1}, V_{S1}	V_{L2}, V_{S2}	V_{L3}, V_{S3}	V_{L4}, V_{S4}

Table 3.1: Proposed Switching Table

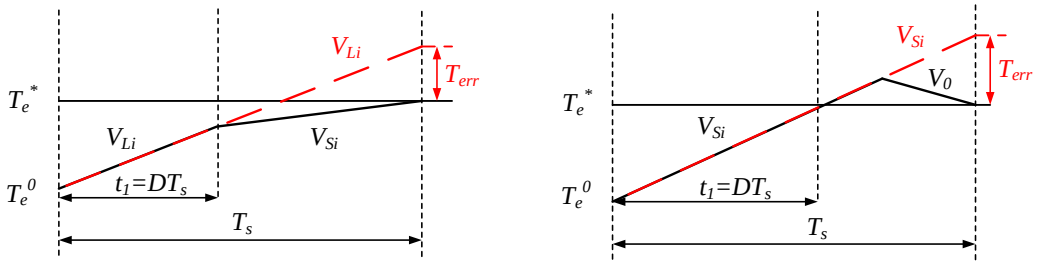

(a) (b)

Figure 3.8: Expected typical steady-state torque response when (a) V_{Li} is used in conjunction with V_{Si} and (b) V_{Si} is used in conjunction with V_0.

3.3.2 Duty Cycle Calculation

For a given voltage vector combination, the voltage vector with the larger magnitude is referred to as the active vector, while the smaller is termed as the passive vector. Figure 3.8 shows the expected steady-state torque responses when V_{Li} is used in conjunction with V_{Si} and V_{Si} is used in conjunction with V_0. The duty cycle of each applied voltage vector within one sampling cycle must be known. There are three methods to determine the duration of the active and passive voltage vectors.

Method 1: The duration of the active vector is determined based on the principle of controlling the instantaneous torque to be equal to the reference value at the end of each sampling cycle [70].

$$T_e(k+1) = T_e^* \tag{3.8}$$

The duration of the active voltage vector can then be obtained as

$$t_1 = \frac{(T_e^* - T_e^0) - s_2 T_s}{s_1 - s_2} \tag{3.9}$$

where T_e^* is the reference torque, T_e^0 is the initial value of instantaneous torque, T_s is the sampling cycle, s_1 and s_2 are the instantaneous rate of torque variation of the active and passive voltage vector respectively. The rate of torque variation in (3.9) can be assumed to be constant within a sampling cycle [71].

Method 2: The duration of the active vector is determined based on the principle of making the mean torque equal to the reference value over a sampling cycle [72].

$$\frac{1}{T_s} \int_{kT_s}^{(k+1)T_s} (T_e^* - T_e)\, dt = 0 \tag{3.10}$$

The duration of the active voltage vector then can be obtained as

$$t_1 = T_s - \sqrt{\frac{T_s}{s_1 - s_2} \left[2\left(T_e^* - T_e^0\right) + s_1 T_s\right]} \tag{3.11}$$

Method 3: The duration of the active vector is determined based on the principle of minimizing root mean square torque ripple over a sampling cycle [71].

$$\frac{1}{T_s} \int_{kT_s}^{(k+1)T_s} \left(T_e^* - T_e^0\right)^2 dt \rightarrow min \tag{3.12}$$

The duration of the active voltage vector then can be obtained as

$$t_1 = \frac{2\left(T_e^* - T_e^0\right) - s_2 T_s}{2s_1 - s_2} \tag{3.13}$$

The rate of torque variation can be determined accurately by using the method in [71], and, hence the accuracy of duty cycle. However, this calculation method is dependent on machine parameters and influenced by one-step delay [73]. Another duty cycle determination method which is much simpler and has been proven by experimental results is presented in [9]. The effect of machine speed has been taken into account in this method.

In this work, the duty cycle for which the active vector is applied is determined in a manner that minimizes the difference between T_e^* and T_e at the end of the sampling cycle, and the rate of torque variation is determined using the theoretical background described in [9]. The duty cycle D of the active voltage vector can be obtained from (3.9) as

$$D = \frac{\left(T_e^* - T_e^0\right) - s_2 T_s}{\left(s_1 - s_2\right) T_s} \tag{3.14}$$

Based on the proposed method two voltage vector combinations are possible. The duty cycle for which the active vector is applied will differ for each combination. For instance, with the combination of V_{Li} as the active vector, V_{Si} as the passive vector, and a hysteresis torque level equal to +2, the rate of torque variation of V_{Li} and V_{Si} at zero and rated speed are given by

$$s_{1(zero)} = s_0; s_{1(rated)} = \gamma s_0 \tag{3.15}$$

$$s_{2(zero)} = 0.5 s_0; s_{1(rated)} = (\gamma - 0.5) s_0 \tag{3.16}$$

where s_0 is the rate of torque variation at zero speed and γ is the ratio of the rate of

torque variation at rated speed to that zero speed. The common expressions for the rate of torque variation s_1 and s_2 are given by

$$s_1 = s_0 + \frac{(\gamma - 1)s_0}{\omega_{rated}}\omega_{re} \tag{3.17}$$

$$s_2 = 0.5s_0 + \frac{(\gamma - 1)s_0}{\omega_{rated}}\omega_{re} \tag{3.18}$$

where ω_{rated} is the rated speed of motor. Through substituting (3.17) and (3.18) into (3.14) the duty cycle of the active vector is

$$D = \frac{(T_e^* - T_e^0) - 0.5k_a - k_b\omega_{re}}{0.5k_a} \tag{3.19}$$

where,

$$k_a = s_0 T_s \tag{3.20}$$

$$k_b = \frac{(\gamma - 1)}{\omega_{rated}} s_0 T_s \tag{3.21}$$

A similar process can be applied for second voltage vector combination, as well as the situation of negative hysteresis torque level. These scenarios are summarized in Table 3.2. For the parameters listed in Table 3.2, s_0 and γ can be easily estimated from machine parameters using (3.4). Knowing s_0 and γ, allows k_a and k_b to be determined from (3.20) and (3.21). These control parameters need to be adjusted on-line in order to achieve the best dynamic response.

3.3.3 Neutral Point Voltage Balancing

According to the preceding section, the small voltage vectors can be used to balance the neutral point voltage. Since the direction of the neutral point current affects the neutral point voltage, its information is vital. Instead of direct measurement or estimation

Voltage vector combination	τ	D
V_{Li} and V_{Si}	+2	$\frac{(T_e^* - T_e^0) - 0.5k_a - k_b\omega_{re}}{0.5k_a}$
	-2	$\frac{(T_e^* - T_e^0) + 0.5k_a - k_b\omega_{re}}{-0.5k_a}$
V_{Si} and V_0	+1	$\frac{(T_e^* - T_e^0) - k_b\omega_{re}}{0.5k_a}$
	-1	$\frac{(T_e^* - T_e^0) - k_b\omega_{re}}{-0.5k_a}$

Table 3.2: Duty cycle of the active vector for different voltage vector combinations

from the switching states, this paper uses a simple, yet effective method, deducing the direction of the neutral point current from the sign of the motor power. Since the torque and speed information is readily available, the proposed DTC algorithm uses the motor power P_m (product of torque and speed), in conjunction with the measured capacitor voltages V_{C1} and V_{C2} to select the appropriate small voltage vectors. For example, if V_{S1} is chosen, $\Delta V_C = V_{C1} - V_{C2}$ and machine power are positive, then switching state POO is selected. This will result in the discharging of C_1 and charging of C_2, thus reducing $|\Delta V_C|$.

3.4 Experimental Results

The proposed DTC strategy is implemented using a Texas instruments TI F28335 digital signal processor. The IPMSM is mechanically coupled to a DC machine acting as a load. Experimental results are gathered using dSPACE DS1106. The corresponding experimental setup and machine parameters are shown in appendix A. For comparison purposes, the performance of the DTC strategy without duty cycle control is also presented. The sampling frequency for both DTC methods is set to 10 kHz. The 3L-SNPC inverter is implemented using SEMIKRON SK50GBB066T and SK50GD12T4T IGBT modules with SKHI 71 drivers, and C_1 and C_2 are each implemented using $200\mu F$ MKP type capacitors.

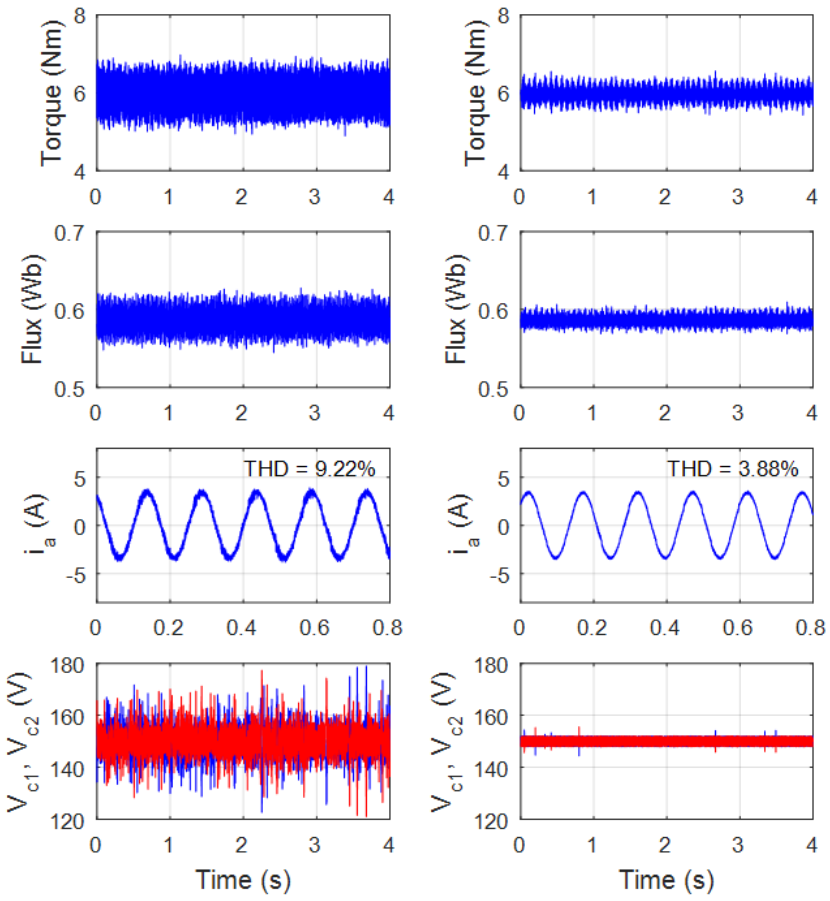

Figure 3.9: Steady-state torque, stator flux, stator current and DC-link capacitor voltages at 200 rpm under the DTC strategy (a) without and (b) with duty cycle control

3.4.1 Steady-state Performance

Figure 3.9 presents the steady-state torque responses at 200 rpm with a rated load of 6 Nm. It can be seen that the torque ripples are significantly reduced for the proposed duty-cycle-control-based DTC strategy. Numerically, the torque ripples are reduced by more than 50% compared to that of the DTC strategy without duty cycle control. Noticeably, the total harmonic distortion (THD) of the stator current is smaller for the proposed duty-cycle-control-based DTC strategy. However, this reduction is less

significant at high operating speeds, as shown in Figure 3.10, for which the back EMF is large compared to the applied voltage.

From Figures 3.9 and 3.10, it also can be concluded that while the capacitor voltages are well balanced for both strategies, the latter shows smaller capacitor voltage fluctuation at the steady state, due to lower harmonic content in the stator currents.

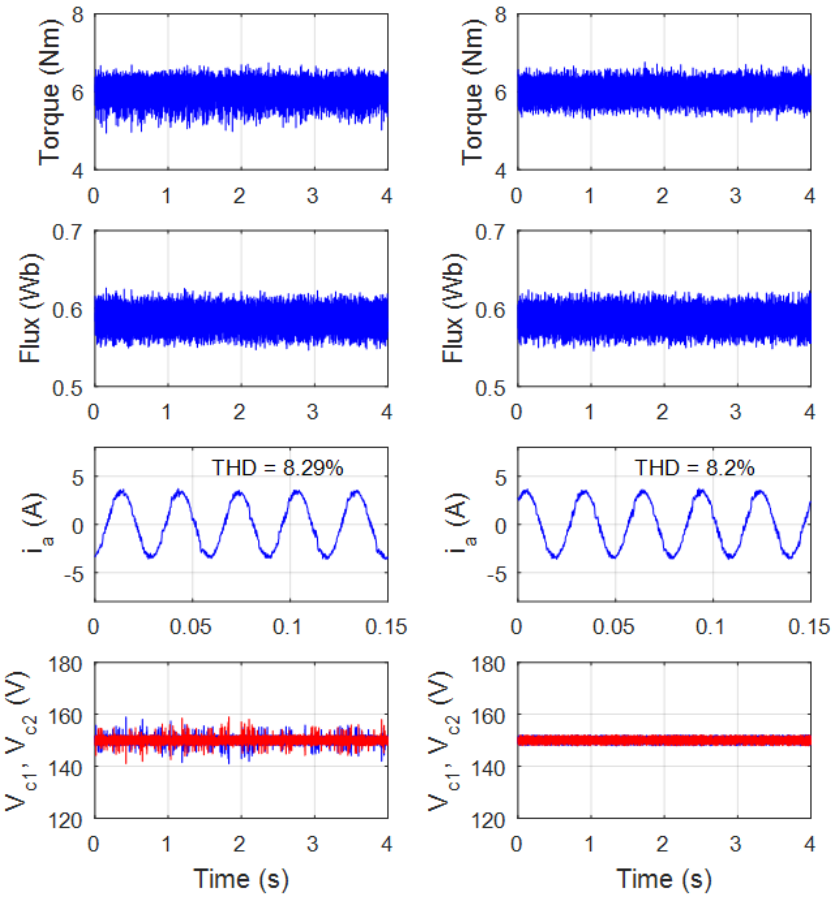

Figure 3.10: Steady-state torque, stator flux, stator current and DC-link capacitor voltages at 1000 rpm under the DTC strategy (a) without and (b) with duty cycle control.

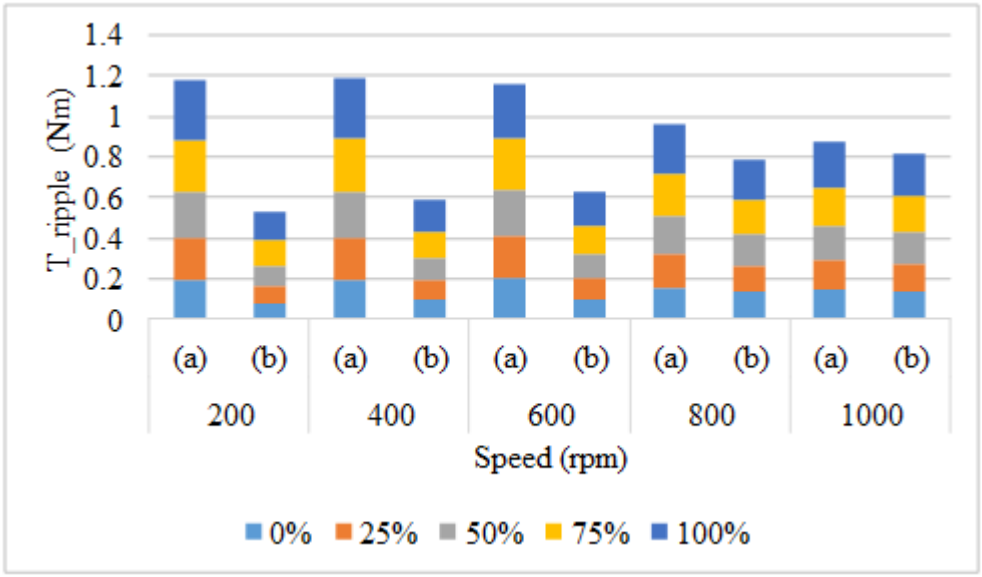

Figure 3.11: Torque ripples at different operating speeds with 0%, 25%, 50%, 75% and 100% of rated load under the DTC strategy (a) without and (b) with duty cycle control.

Figure 3.11 illustrates the torque ripples at different operating speeds with 0%, 25%, 50%, 75% and 100% of rated load for both strategies. It can be observed that the torque ripples are smaller for the DTC strategy with duty cycle control under all load conditions, and therefore proving the feasibility of the proposed method.

3.4.2 Speed Transient Performance

Figure 3.12 illustrates a comparison of the dynamic speed reversal from -1000 rpm to +1000 rpm between the DTC strategy with and without duty cycle control. While both methods yield similar performances, the torque ripples are noticeably smaller for the latter. Identical speed reversal duration is observed for two strategies, which demonstrates the excellent dynamic response of the proposed algorithm. The speed, torque, flux as well as the capacitor voltages are well regulated during transient of speed reversal. There are transient imbalances of the capacitor voltages V_{C1} and V_{C2} as shown

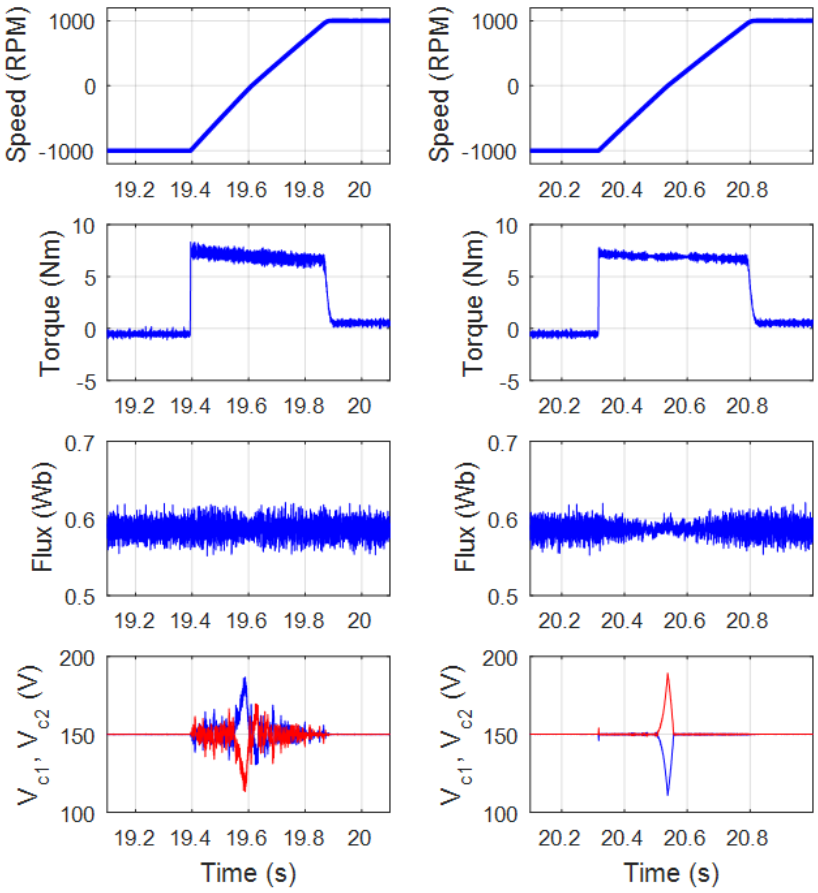

Figure 3.12: Speed, torque, stator flux and DC-link capacitor voltages during speed reversal under the DTC strategy (a) without and (b) with duty cycle control.

in the fourth subplot of Fig. 15(b). However, the imbalances are controllable since the converging of V_{C1} and V_{C2} to their average value is observed to be within tens of milliseconds.

3.4.3 Load Transient Performance

Figure 2.15 presents the transient performance of the drive with sudden full-load application. It can be observed that the stability of the drive is well-maintained with

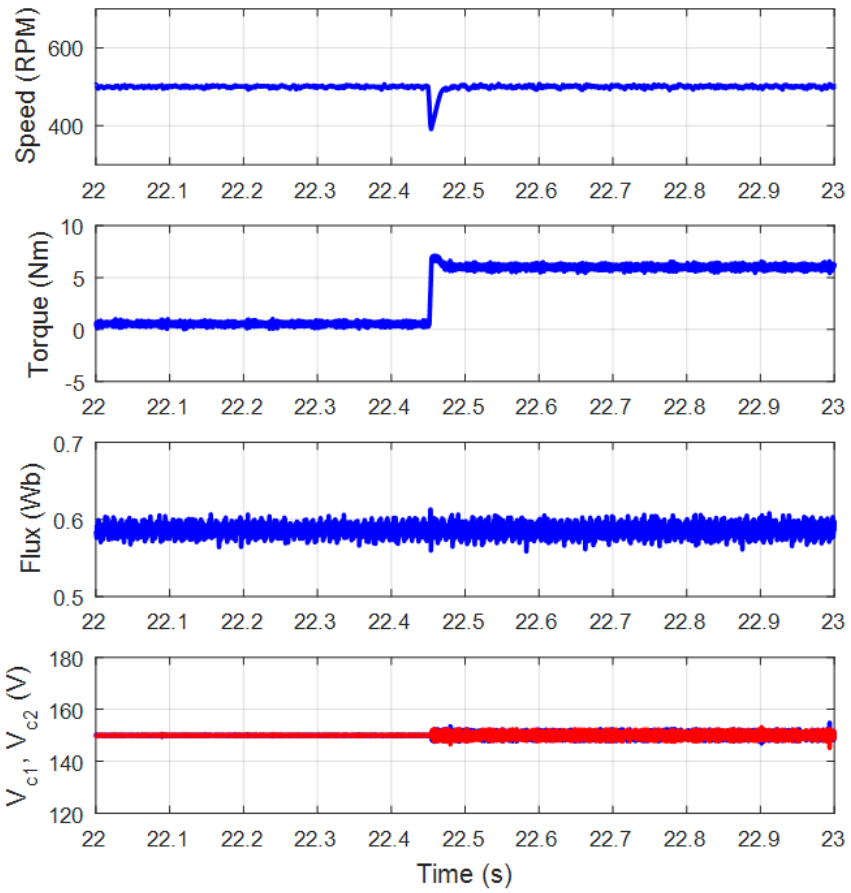

Figure 3.13: Speed, torque, flux and capacitor voltages responses when a sudden load is applied at 500RPm under the DTC with duty cycle control.

excellent torque and flux performance. Simultaneously, the DC-link capacitor voltages are balanced.

3.5 Conclusion

This chapter proposes a duty-cycle-control-based DTC strategy for an IPMSM driven by a 3L-SNPC inverter. The torque ripple reduction is achieved by using two voltage vectors within each sampling cycle. By controlling the instantaneous torque to be equal

to its reference value, the duration of each of the applied voltage vectors is determined. In addition, by measuring the capacitor voltages and manipulating the redundant states of the small voltage vectors, the neutral point voltage is controlled. The experimental results included show that the proposed duty-cycle-control-based DTC strategy achieves better performance when compared to the non-duty cycle-based DTC strategy.

Chapter 4

A Duty-Cycle-Control-Based PTC Strategy for the 3L-SNPC Inverter-fed IPMSM Drives

4.1 Introduction

In the previous chapter, a DTC strategy for IPMSM driven by 3L-SNPC have been proposed. This is a hysteresis control method, whereby a torque hysteresis controller and a flux hysteresis controller are used, to directly control the electromagnetic torque and stator flux within the hysteresis bands. Another direct control method, which recently has received a lot of research attentions, is the predictive torque control (PTC) [74, 75]. Compared to DTC, PTC has a simpler control structure, yet maintains the advantage of a fast dynamic response [24]. The PTC algorithm is based on the concept of using the knowledge of the stator currents and rotor speed at current state to predict the electromagnetic torque and stator flux in the future state. Then, the most appropriate voltage vector that minimises the predetermined cost function and hence, the torque error is selected. However, high torque ripple levels are incurred, because of the use

of only one voltage vector within each sampling cycle [23]. Due to the importance of reducing torque ripple significant research effort exists in the area, largely focused on two-level inverter fed PTC [19, 21, 23, 76–84].

In this chapter, a PTC strategy with torque ripple reduction suitable for a 3L-SNPC inverter-driven IPMSM is proposed. To reduce the torque ripples, a duty-cycle-control-based PTC strategy is implemented. With the knowledge of the torque error and speed of the motor, the duration of the application of the optimal voltage vector within one sampling cycle is calculated. A different voltage vector is then applied for the remainder of the sampling cycle. The voltage vectors are selected to minimize the torque ripples and simultaneously balance the two DC-link capacitor voltages. Moreover, the motor model used in the proposed method pertain to the stationary $(\alpha - \beta)$ reference frame, thereby avoiding computationally intensive rotary coordinate transformations.

This chapter is organized as follows. Section 4.2 presents the mathematical model of the IPMSM, and design equations of the proposed PTC strategy is presented in section 4.3. Section 4.4 presents experimental results validating the effectiveness of the proposed strategy, and section 4.5 provides concluding remarks.

4.2 Mathematical Model of IPMSM in the stationary $(\alpha - \beta)$ reference frame

The IPMSM is modelled in the stationary $(\alpha - \beta)$ reference frame with the stator voltage and electromagnetic torque given by

$$\boldsymbol{v_s} = R_s \boldsymbol{i_s} + \frac{d\boldsymbol{\lambda_s}}{dt} \tag{4.1}$$

$$\boldsymbol{T_e} = \frac{3}{2} P \left(\boldsymbol{\lambda_s} \times \boldsymbol{i_s} \right) \tag{4.2}$$

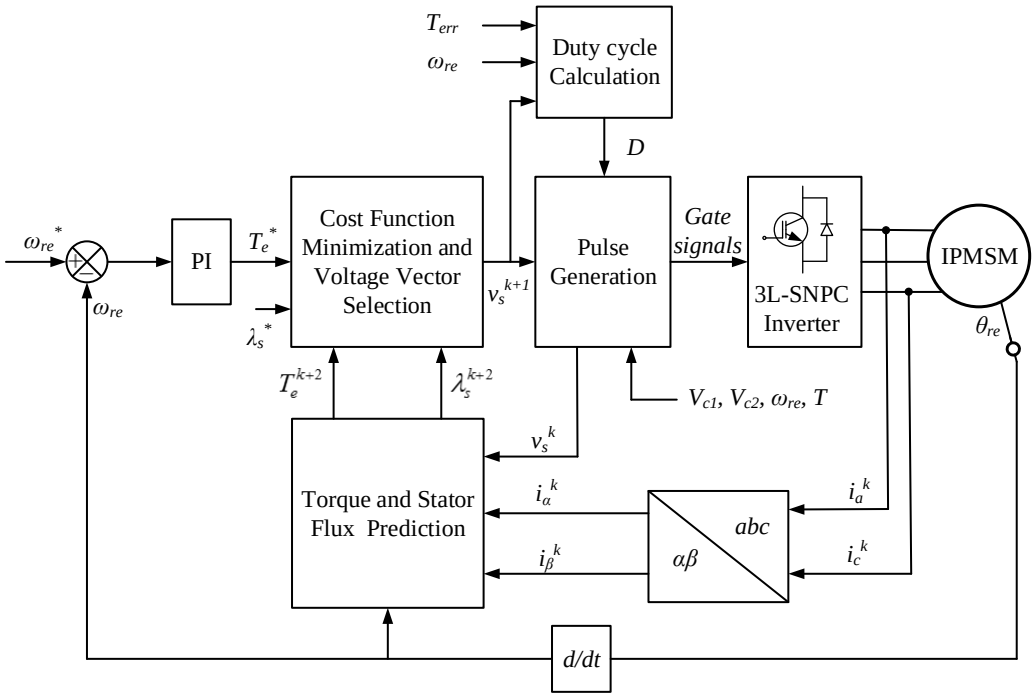

Figure 4.1: Block diagram of the proposed duty-cycle-control-based PTC strategy

where $\boldsymbol{v_s}$, $\boldsymbol{i_s}$ and $\boldsymbol{\lambda_s}$ are the stator voltage, current and flux linkage vectors in the stationary $(\alpha - \beta)$ reference frame.

4.3 The Proposed PTC Strategy

The block diagram of the proposed PTC strategy for IPMSM is shown in Figure 4.1. The control algorithm consists of four main steps: stator flux estimation, stator flux and torque prediction, cost function minimization and voltage vector selection, and duty cycle calculation. The stator currents and motor speed are sampled at the present sampling cycle k to predict the torque and stator flux at the next two sampling cycles for a finite number of voltage vectors. Subsequently, the voltage vector that minimizes the predetermined cost function is chosen and applied to the stator. However, due to the application of the optimal voltage vector over the whole sampling cycle, the error

between the predicted torque and the torque reference is significant. To further reduce the torque error, a duty-cycle-control-based PTC strategy is implemented. From the information of the torque error $T_{err} = T_e^* - T_e$ where T_e^* is the torque reference, the duration of the optimal voltage vector within one sampling cycle is determined. The optimal voltage vector is applied for that time interval while another voltage vector fills the remainder of the sampling cycle.

4.3.1 Stator Flux Estimation

The stator flux at the current sampling cycle $\boldsymbol{\lambda_s}^k$ can be estimated using the stator resistance R_s, and the information of the stator flux, applied voltage vector and stator current vectors from the previous sampling cycle as

$$\boldsymbol{\lambda_s}^k = \boldsymbol{\lambda_s}^{k-1} + T_s \left(\boldsymbol{v_s}^{k-1} - R_s \boldsymbol{i_s}^{k-1} \right) \tag{4.3}$$

where T_s is the sampling cycle.

4.3.2 Stator Flux and Torque Prediction

Based on the measured stator currents and estimated stator flux at the current sampling cycle k, the stator flux at the next sampling cycle $k+1$ can be predicted as

$$\boldsymbol{\lambda_s}^{k+1} = \boldsymbol{\lambda_s}^k + T_s \left(\boldsymbol{v_s}^k - R_s \boldsymbol{i_s}^k \right) \tag{4.4}$$

In order to predict the torque, a prediction of the stator current at sampling cycle $k+1$ is needed, and can be obtained using

$$\frac{d\boldsymbol{i_s}}{dt} = -\frac{R_s}{L_q}\boldsymbol{i_s} + j\frac{\omega_{re}}{L_q}\left(\boldsymbol{\lambda_s} - L_q \boldsymbol{i_s}\right) + \frac{1}{L_q}\boldsymbol{v_s} \tag{4.5}$$

where L_q and ω_{re} represent the stator inductance in $q-$axis and the electrical speed of rotor, respectively.

By using the Euler forward method, the prediction of the stator current is derived as

$$\boldsymbol{i_s}^{k+1} = \left(1 - T_s\frac{R_s}{L_q}\right)\boldsymbol{i_s}^{k} + jT_s\frac{\omega_{re}}{L_q}\left(\boldsymbol{\lambda_s}^{k} - L_q\boldsymbol{i_s}^{k}\right) + \frac{T_s}{L_q}\boldsymbol{v_s}^{k} \tag{4.6}$$

From (4.4) and (4.6), the torque prediction at the sampling cycle $k+1$ can be calculated as

$$\boldsymbol{T_e}^{k+1} = \frac{3}{2}P\left(\boldsymbol{\lambda_s^{k+1}} \times \boldsymbol{i_s}^{k+1}\right) \tag{4.7}$$

In practical implementation, the one-step delay increases the torque ripples. By shifting forward one sampling cycle for the prediction of torque, this time delay can be compensated [23]. The torque prediction at the sampling cycle $k+2$ can therefore be calculated as

$$\boldsymbol{T_e}^{k+2} = \frac{3}{2}P\left(\boldsymbol{\lambda_s}^{k+2} \times \boldsymbol{i_s}^{k+2}\right) \tag{4.8}$$

where the prediction of the stator flux $\boldsymbol{\lambda_s^{k+2}}$, and stator current $\boldsymbol{i_s}^{k+2}$ are obtained from

$$\boldsymbol{\lambda_s}^{k+2} = \boldsymbol{\lambda_s}^{k+1} + T_s\left(\boldsymbol{v_s}^{k+1} - R_s\boldsymbol{i_s}^{k+1}\right) \tag{4.9}$$

$$\boldsymbol{i_s}^{k+2} = \left(1 - T_s\frac{R_s}{L_q}\right)\boldsymbol{i_s}^{k+1} + jT_s\frac{\omega_{re}}{L_q}\left(\boldsymbol{\lambda_s}^{k+1} - L_q\boldsymbol{i_s}^{k+1}\right) + \frac{T_s}{L_q}\boldsymbol{v_s}^{k+1} \tag{4.10}$$

4.3.3 Cost Function Minimization and Voltage Vector Selection

The 3L-SNPC inverter allows thirteen voltage vectors to be chosen, including V_{Li}, V_{Si} (for i = 0 to 6), and V_0. The voltage vector that minimizes the cost function J will be

selected and applied in the next sampling cycle [23].

$$J = |T_e^* - T_e^{k+2}| + k_f||\lambda_s^*| - |\lambda_s^{k+2}|| \tag{4.11}$$

where k_f denotes the weighting factor. k_f needs to be adjusted in order to achieve the best dynamic response. A starting point to select k_f is given by

$$k_f = \frac{T_{rated}}{\lambda_{rated}} \tag{4.12}$$

where T_{rated} and λ_{rated} are the rated electromagnetic torque and stator flux respectively [25].

4.3.4 Duty Cycle Calculation

The concept of duty cycle control method presented in the previous chapter are incorporated into the proposed PTC strategy. The duration t_1 of the optimal voltage vector can be obtained as

$$t_1 = DT_s = \frac{(T_e^* - T_e^0) - s_2 T_s}{s_1 - s_2} \tag{4.13}$$

D is the duty cycle of the optimal voltage vector, T_e^0 is the initial value of instantaneous torque, s_1 and s_2 are instantaneous rate of torque variation of the optimal and second voltage vector respectively. The rate of torque variation in (4.13) can be assumed to be constant within a sampling cycle [71].

There are two possible voltage vector combinations while there are two possible signs of the torque error. Thus, there are four possible scenarios with different duty cycles for the optimal voltage vector. For example, with the scenario of V_{Li} as the optimal vector,

V_{Si} as the second vector, and T_{err} is positive, the expressions for rate of torque variation s_1 and s_2 are given by

$$s_1 = s_0 + \frac{(\gamma - 1)s_0}{\omega_{rated}}\omega_{re} \tag{4.14}$$

$$s_2 = 0.5s_0 + \frac{(\gamma - 1)s_0}{\omega_{rated}}\omega_{re} \tag{4.15}$$

where s_0 is the rate of torque variation at zero speed, γ is the ratio of the rate of torque variation at rated speed to that at zero speed and ω_{rated} is the rated speed of rotor. Substituting (4.14) and (4.15) into (4.13) yields the duty cycle of the optimal voltage vector.

$$D = \frac{(T_e^* - T_e^0) - 0.5k_a - k_b\omega_{re}}{0.5k_a} \tag{4.16}$$

where,

$$k_a = s_0 T_s \tag{4.17}$$

$$k_b = \frac{(\gamma - 1)}{\omega_{rated}} s_0 T_s \tag{4.18}$$

A similar process can be applied for second voltage vector combination, as well as the situation of negative torque error. These scenarios are summarized in Table 4.1. The rate of torque variation s_0 and coefficient γ can be estimated using (16). With the knowledge of s_0 and γ, the coefficients k_a and k_b can be calculated from (4.17) and (4.18). These control parameters then need to be adjusted on-line in order to achieve the best dynamic response.

Voltage vector combination	T_{err}	D
V_{Li} and V_{Si}	Positive	$\frac{(T_e^* - T_e^0) - 0.5k_a - k_b\omega_{re}}{0.5k_a}$
	Negative	$\frac{(T_e^* - T_e^0) + 0.5k_a - k_b\omega_{re}}{-0.5k_a}$
V_{Si} and V_0	Positive	$\frac{(T_e^* - T_e^0) - k_b\omega_{re}}{0.5k_a}$
	Negative	$\frac{(T_e^* - T_e^0) - k_b\omega_{re}}{-0.5k_a}$

Table 4.1: Duty cycle of the optimal vector for different voltage vector combinations.

4.3.5 Neutral Point Voltage Balancing

For the 3L-SNPC inverter, only V_{Si} affects the neutral point voltage. Therefore, whenever V_{Si} is applied, an appropriate switching state can be selected according to the difference between the two capacitor voltages $\Delta V_C = V_{C1} - V_{C2}$ and the and the sign of the machine power P_m, to reduce the imbalance. If $\Delta V_C > 0$ and $P_m > 0$, the V_{Si} in Group I will be selected. This will result in the discharging of C_1 and charging of C_2, thus reducing $|\Delta V_C|$. For the case when $\Delta V_C > 0$ and $P_m < 0$, the V_{Si} in Group II will be selected.

4.3.6 Control Flow of the Proposed PTC Algorithm

The proposed control algorithm can be summarized in the following sequence.

- Step 1: Estimate the stator flux $\boldsymbol{\lambda_s}^k$ from the information of $\boldsymbol{\lambda_s}^{k-1}$, $\boldsymbol{v_s}^{k-1}$ and $\boldsymbol{i_s}^{k-1}$ using (4.3). It is noteworthy that $\boldsymbol{v_s}^{k-1}$ is the combination of the applied optimal voltage vector and second voltage vector.

- Step 2: Measure the stator current $\boldsymbol{i_s}^k$ and rotor speed ω_{re}^k; and predict the stator flux $\boldsymbol{\lambda_s}^{k+1}$ and stator current $\boldsymbol{i_s}^{k+1}$ using (4.4) and (4.6) respectively.

- Step 3: For each voltage vector, calculate the predicted the torque T_e^{k+2} and stator flux $\boldsymbol{\lambda_s}^{k+2}$ using (4.8) and (4.9). Then, calculate the cost function using (4.11).

- Step 4: Find the smallest cost function and determine the optimal voltage vector. Then, calculate the duration of the optimal voltage vector using equations in Table 4.1, and determine second voltage vector. If V_{Si} is selected, an appropriate switching state that reduces the difference between the two DC-link capacitor voltages will be chosen.

- Step 5: Generate control signals. Then, return to Step 1.

4.3.7 Robustness to Parameter Variations

It is obvious that the prediction of torque and flux are dependent on the machine parameters. To investigate the robustness of the proposed control method to machine parameter variations, the performance of the predictive torque controller with detuning in the stator resistance R_s and in the $q-$axis inductance L_q are carried out. For this investigation R_s is increased above its nominal value of 100% to emulate increasing resistance with temperature, and L_q is decreased below its nominal value to mimic saturation. Figure 4.2 shows the dynamic torque with different R_s and nominal L_q, while Figure 4.3 shows the response with different L_q and nominal R_s. From these results, it is apparent that the torque response is largely insensitive to parameter variations,

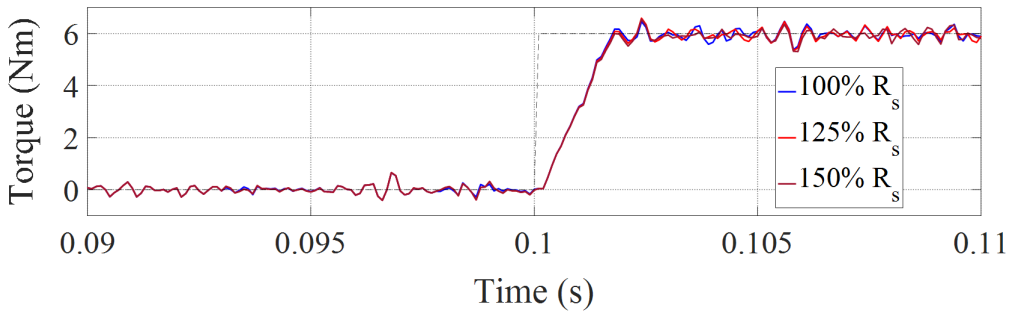

Figure 4.2: Simulation results of the torque dynamics with different detuning in the stator resistance for the duty-cycle-control-based PTC strategy.

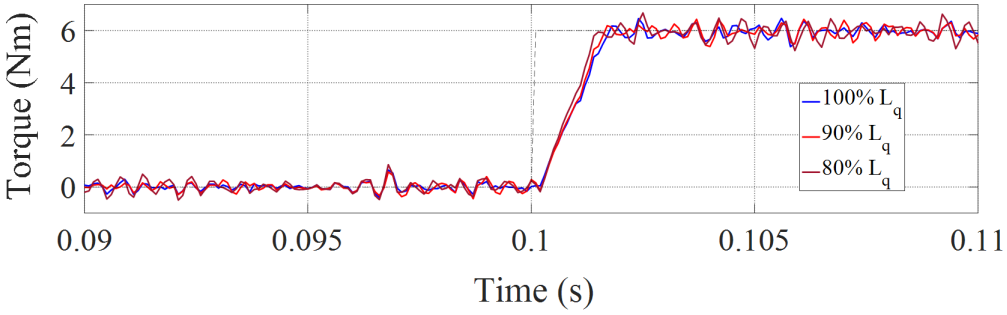

Figure 4.3: Simulation results of the torque dynamics with different detuning in the $q-$axis inductance for the duty-cycle-control-based PTC strategy

illustrating the robustness of the proposed technique.

4.4 Experimental Results

In this section, experimental results are presented to verify the steady-state and transient performance of the proposed duty-cycle-control-based PTC. For comparison purposes, the performance of the PTC strategy without duty cycle control is also presented. Experimental setup and machine parameters are shown in appendix A. The sampling frequency for both strategies is set to 10 kHz.

4.4.1 Steady-state Performance

Figure 4.4 presents the steady-state torque responses at 200 rpm with a rated load of 6 Nm. It can be seen that the torque ripples are significantly reduced for the proposed duty-cycle-control-based PTC strategy. Numerically, the torque ripples are reduced by more than 50% compared to that of the PTC strategy without the duty cycle control. Noticeably, the total harmonic distortion (THD) of the stator current also is smaller for the proposed duty-cycle-control-based PTC. These observations are consistent with the reduction in stator flux ripples. However, this reduction is less significant at high

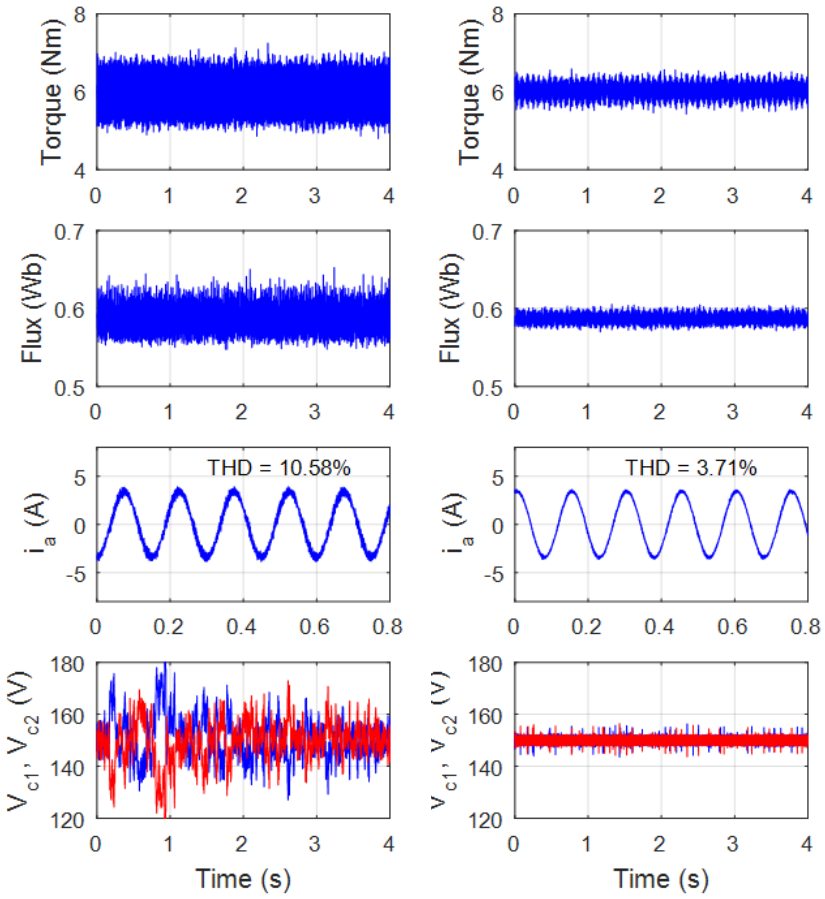

Figure 4.4: Steady-state torque, stator flux, stator current and DC-link capacitor voltages at 200 rpm under the PTC strategy (a) without and (b) with duty cycle control

operating speeds, as shown in Figure 4.5, for which the back EMF is large compared to the applied voltage.

From Figures 4.4 and 4.5, it also can be deduced that while the capacitor voltages are well balanced for both strategies, the duty-cycle-control-based PTC strategy shows smaller capacitor voltage fluctuation at the steady state due to lower harmonic content in the stator currents.

Figure 4.6 illustrates the torque ripples at different operating speeds with 0%, 25%,

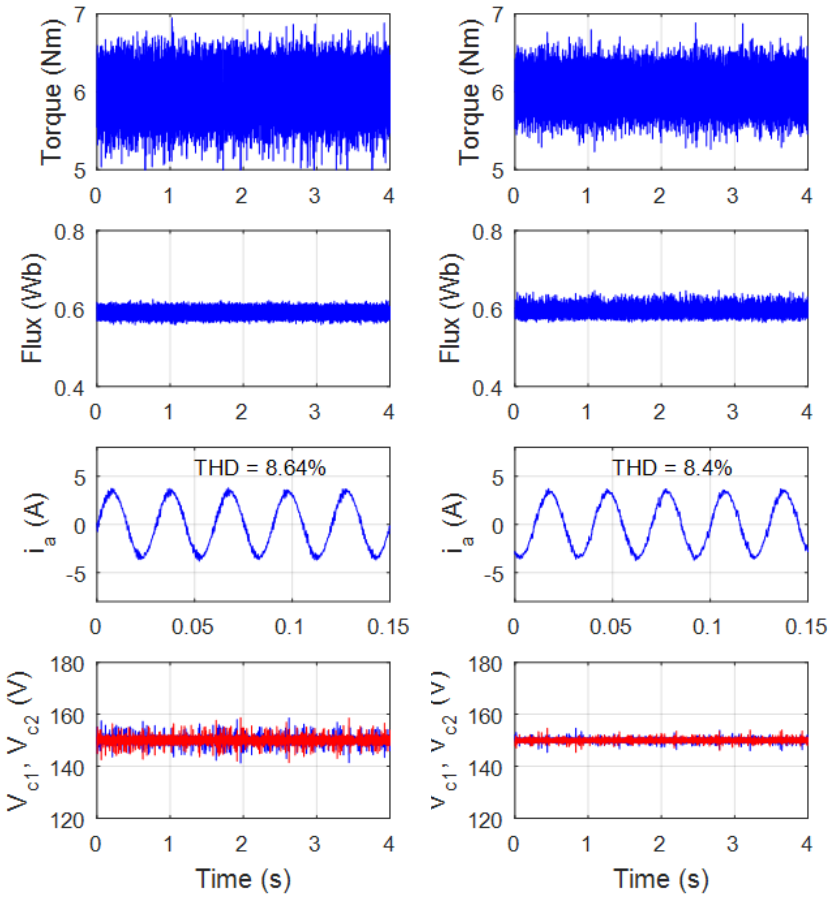

Figure 4.5: Steady-state torque, stator flux, stator current and DC-link capacitor voltages at 1000 rpm under the PTC strategy (a) without and (b) with duty cycle control.

50%, 75% and 100% of rated load for both strategies. It can be observed that the torque ripples are smaller for the PTC strategy with duty cycle control under all load conditions, and therefore proving the feasibility of the proposed method.

4.4.2 Transient Performance

Figure 4.7 illustrates a comparison of the dynamic speed reversal from -1000 RPM to +1000 PRM between the PTC strategy with and without duty cycle control. While

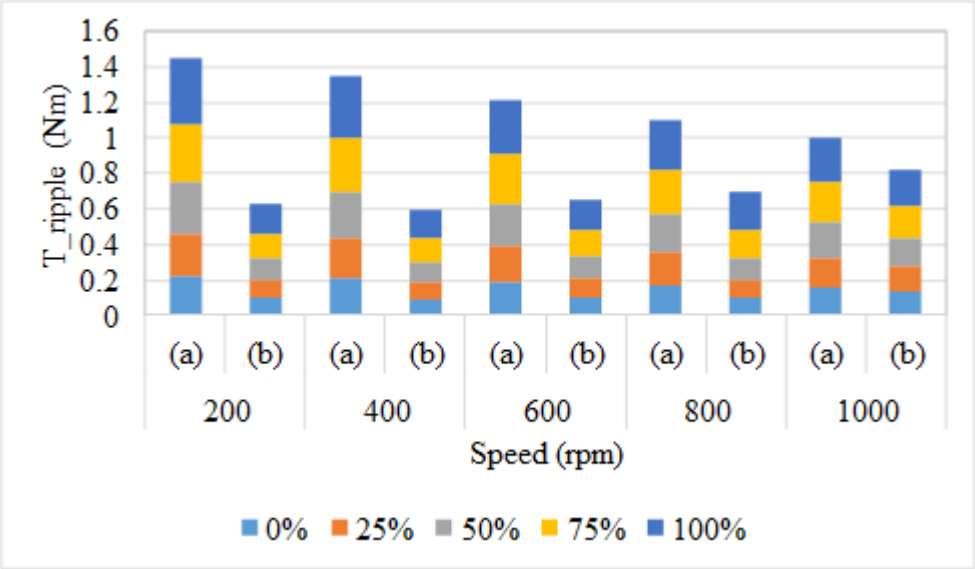

Figure 4.6: Torque ripples at different operating speeds with 0%, 25%, 50%, 75% and 100% of rated load under the PTC strategy (a) without and (b) with duty cycle control.

both methods yield similar performances, the torque ripples are noticeably smaller for the proposed duty-cycle-control-based PTC strategy. The speed, torque, flux as well as the capacitor voltages are well regulated during transient of speed reversal. There are transient imbalances of the capacitor voltages V_{C1} and V_{C2} as shown in the fourth subplot of Figure 4.7. However, the imbalances are controllable since the converging of V_{C1} and V_{C2} to their average value is observed to be within tens of milliseconds.

4.5 Conclusion

In this chapter, an improved PTC strategy that reduces the torque ripples is proposed for an IPMSM driven from a 3L-SNPC inverter. The proposed method significantly reduces the torque and stator flux ripples. The optimal voltage vector is initially selected according to the PTC method. Nevertheless, the application of this voltage vector over the whole sampling cycle inevitably increases the torque ripples. This problem

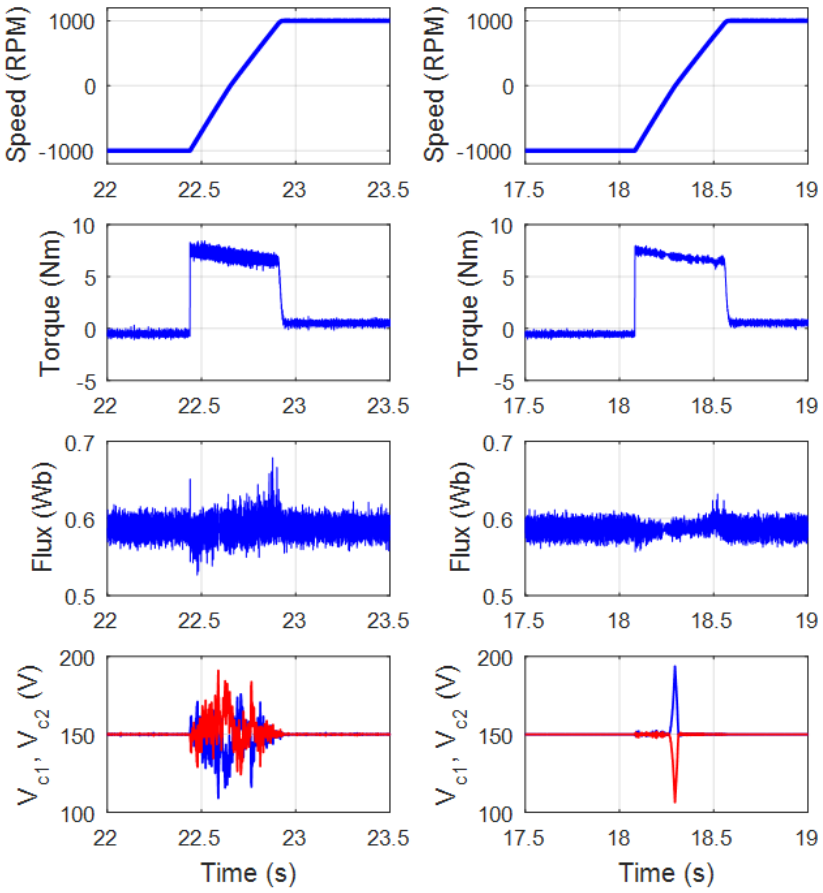

Figure 4.7: Speed, torque, stator flux and DC-link capacitor voltages during speed reversal for the PTC strategy (a) without and (b) with duty cycle control.

is mitigated by the implementation of a simple duty cycle control method, whereby the optimal voltage vector is used in conjunction with the second voltage vector. The duration of both the applied voltage vectors are determined using the knowledge of torque error and motor speed. Neutral point voltage balancing is incorporated into the proposed algorithm. The experimental results show a significant improvement in the torque ripples, thereby confirming the effectiveness of the proposed method.

Chapter 5

A Torque-Regulator-Based DTC Strategy for the 3L-SNPC Inverter-fed IPMSM Drives

5.1 Introduction

The duty-cycle-control-based DTC strategy for IPMSM driven by a 3L-SNPC inverter has been presented in chapter 3, including details of the theoretical development and experimental verification. Compared to the non-duty-cycle-control DTC strategy, the proposed duty-cycle-control-based DTC strategy achieves smaller torque and stator flux ripples. However, this method necessitates operation at a variable switching frequency. To address this issues, a torque-regulator-based DTC strategy is proposed in this chapter. The proposed strategy employs a PI torque controller and four triangular-carriers to attain torque ripple reduction at a constant switching frequency. Furthermore, the issue of DC-link capacitor voltages imbalance is also addressed.

This chapter is organized as follows. Section 5.3 presents the design of the torque

regulator. Section 5.4 presents experimental results validating the effectiveness of the proposed strategy, and section 5.5 provides concluding remarks.

5.2 Rate of Torque Variation

In the $(x-y)$ reference frame, the machine voltage equations and electromagnetic torque are given by

$$v_x = R_s i_x + \frac{d\lambda_s}{dt} \tag{5.1}$$

$$v_y = R_s i_y + \lambda_s \omega_s \tag{5.2}$$

$$T_e = \frac{3P}{2}\lambda_s i_y \tag{5.3}$$

where, λ_s is stator flux linkage, ω_s is the speed of stator flux linkage vector, v_x, v_y, i_x, i_y are the stator voltages and stator currents in the $(x-y)$ reference frame, T_e electromagnetic torque, and P number of pole pairs.

The rate of torque variation can be derived from (5.1), (5.2) and (5.3) as

$$\frac{T_e}{dt} = -\frac{R_s}{L_q}T_e - \frac{3P}{2L_q}\lambda_s\lambda_a \cos\delta\omega_{re} + \frac{3P}{2L_q}\left(\lambda_a \sin\delta v_x + \lambda_a \cos\delta v_y\right) \tag{5.4}$$

where L_d, L_q are the $dq-$ axis inductances, δ is the load angle, $\lambda_a = \lambda_f + (L_d - L_q)i_d$ and is termed as the active flux [69], i_d is the $d-$ axis stator current, λ_f is the permanent magnet flux linkage and ω_{re} is the electrical speed of rotor.

It can be observed that the third right hand side term of (5.4) reflects the effect of stator voltage on the rate of torque variation. In addition, it can be inferred that the zero voltage vector always reduces the torque and if a single voltage vector is applied over the entire sampling cycle, significant torque variations will occur.

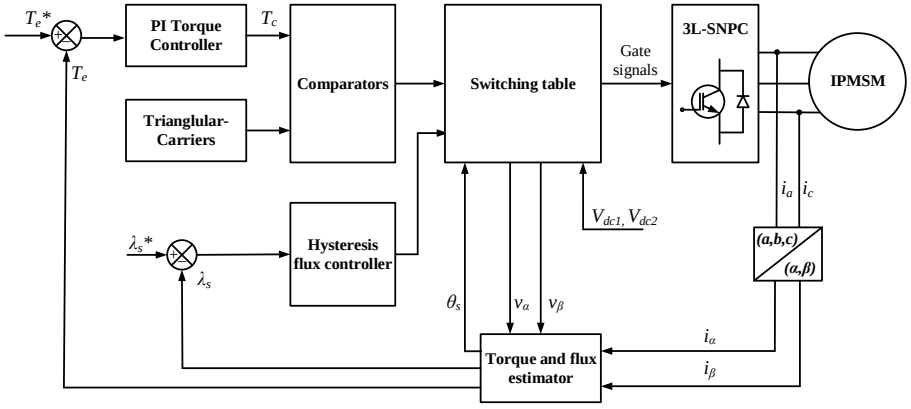

Figure 5.1: Block diagram of the proposed torque-regulator-based DTC strategy

5.3 The Proposed Strategy

The block diagram of the proposed DTC strategy is shown in Figure 5.1. The torque and stator flux linkage are estimated from the measured stator currents. The torque and flux error are then calculated and fed to the controllers. The flux levels are determined by the hysteresis flux controller with knowledge of the flux error. On the other hand, the torque levels are determined by comparing the output of PI torque controller with four triangular-carriers. With knowledge of the torque and flux levels, an appropriate voltage vector will be selected from the switching table. The torque and stator flux are therefore directly controlled. The speed of the machine is measured, and a PI controller which outputs the torque reference is used for the outer speed control loop. In this section, the key aspects of proposed system are described including design of the torque regulator and the guidelines for controller gains selection.

5.3.1 The Proposed Torque Regulator

The torque ripple reduction strategy proposed in this paper is to use a PI controller to negate the large rate of torque variation. To achieve a constant switching frequency, four periodic triangular-carriers are used. The output of the torque controller is compared to

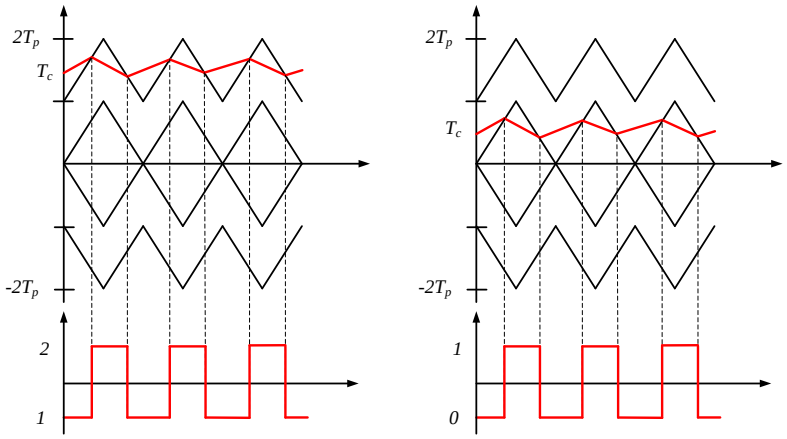

Figure 5.2: Hysteresis logic of the proposed torque regulator.

the triangular-carriers to determine the hysteresis logic of torque control. Figure 5.2 shows the waveform of hysteresis logic with the proposed torque controller. Within each switching cycle, two voltage vectors (VVs) are applied to negate the large rate of torque variation. Depending on the output of the PI torque controller, two allowed possible combinations are (V_{Li}, V_{Si}) and (V_{Si}, V_0). The average rate of torque variation can be expressed as

$$\frac{dT_{e(avg)}}{dt} = D\frac{dT_{e(first\ VV)}}{dt} + (1-D)\frac{dT_{e(second\ VV)}}{dt} \tag{5.5}$$

where D is the duty cycle of the first voltage vector. With an assumption that the stator resistance R_s is neglected, and from the fact that the stator flux linkage is usually controlled to be a constant, it can be inferred from (5.5) that the $x-$component of the stator voltage can be approximated to be zero. Therefore, the average rate of torque variation can be derived from (5.4) and (5.5) as

$$\begin{aligned}\frac{dT_{e(avg)}}{dt} = D\left[-\frac{R_s}{L_q}T_e + \frac{3P}{2L_q}\left(v_{s(first\ VV)} - \lambda_s\omega_{re}\right)\lambda_{ax}\right] \\ + (1-D)\left[-\frac{R_s}{L_q}T_e + \frac{3P}{2L_q}\left(v_{s(second\ VV)} - \lambda_s\omega_{re}\right)\lambda_{ax}\right]\end{aligned} \tag{5.6}$$

where $\lambda_{ax} = \lambda_a \cos\delta$. For instance, when V_{Li} and V_{Si} are used within one switching cycle, the average rate of torque variation can be expressed as

$$\frac{dT_{e(avg)}}{dt} = -\frac{R_s}{L_q}T_e + \frac{3P}{2L_q}\left[\frac{1}{2}\left(D+1\right)v_s - \lambda_s\omega_{re}\right]\lambda_{ax} \tag{5.7}$$

Similarly, the average rate of torque variation when V_{Si} is used in conjunction with V_0 can be derived as

$$\frac{dT_{e(avg)}}{dt} = -\frac{R_s}{L_q}T_e + \frac{3P}{2L_q}\left[\frac{1}{2}Dv_s - \lambda_s\omega_{re}\right]\lambda_{ax} \tag{5.8}$$

5.3.2 Small-Signal Control-to-Output Transfer Function

With knowledge of the average rate of torque variation, the small-signal transfer function of torque controller can be derived by applying small perturbations $\left(\widetilde{D}, \widetilde{T_e}\right)$ around the operating points (D_0, T_e^0), the following can be deduced

$$D = D_0 + \widetilde{D} \tag{5.9}$$

$$T_e = T_e^0 + \widetilde{T_e} \tag{5.10}$$

Substituting (5.9) and (5.10) into (5.7) and (5.8), both instances give

$$\widetilde{T_e}\left(s\right) = \frac{3P\lambda_{ax}v_s}{4L_q\left(s + \frac{R_s}{L_q}\right)}\widetilde{D}\left(s\right) \tag{5.11}$$

5.3.3 PI Torque Controller

The block diagram of the proposed torque regulator is shown in Figure 5.3. K_p and K_i are the proportional and integral gains of the torque PI controller respectively. The closed loop transfer function of the torque regulator is expressed as

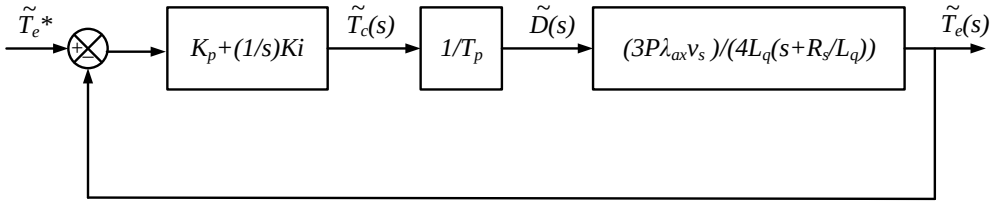

Figure 5.3: Small-signal block diagram of the proposed torque regulator.

$$G(s) = \frac{\widetilde{T_e}(s)}{\widetilde{T_e^*}(s)} = \frac{K(K_p s + K_i)}{s^2 + s\left(KK_p + \frac{R_s}{L_q}\right) + KK_i} \tag{5.12}$$

where,

$$K = \frac{3P\lambda_{ax}v_s}{4L_q T_p} \tag{5.13}$$

From (5.12), it can be observed that the torque control loop is a second-order system. The controller gains can be calculated as

$$K_p = \frac{2\xi\omega_n - \frac{R_s}{L_q}}{K} \tag{5.14}$$

$$K_i = \frac{\omega_n^2}{K} \tag{5.15}$$

where ξ and ω_n are the damping ratio and natural frequency of the system. These parameters can be found from the overshoot $(OS\%)$ and settling time (t_s) of the desired transient response, using (4.16) and (5.17).

$$OS\% = e^{-\frac{\xi\pi}{\sqrt{1-\xi^2}}} \tag{5.16}$$

$$t_s = \frac{4}{\xi\omega_n} \tag{5.17}$$

It is noteworthy that the hysteresis logic of torque control is determined by comparing

the output of the PI torque controller (T_c) with the triangular-carriers. Therefore, the absolute rate of torque variation or slope of T_c must not exceed the absolute slope of the triangular carriers under all working conditions. Since the absolute slope of T_c is mainly influenced by K_p, the following constraint must be satisfied [85]

$$\frac{dT_{carrier}}{dt} \geq max|\frac{dT_e}{dt}|K_p \tag{5.18}$$

The damping ratio and setting time are selected to be 0.7 and 5 ms, respectively, resulting in nature frequency $\omega_n = 1142.86rad/s$. The gains of the PI torque controller calculated from (4.16) and (5.17) is $K_p = 105$ and $K_i = 2.2$. The carrier signals with fixed frequency of 1.5 kHz are used for the proposed algorithm. The absolute peak value of the carriers (T_p) are selected to be 250 that ensures the constraint in (5.18) is satisfied.

5.3.4 Neutral Point Voltage Balancing

As mentioned in the previous chapters, the small voltage vectors can be used to balance the neutral point voltage. Since the direction of the neutral point current affects the neutral point voltage, its information is vital. Instead of direct measurement or estimation from the switching states, this paper uses a simple, yet effective method, deducing the direction of the neutral point current from the sign of the motor power. Since the torque and speed information is readily available, the proposed torque-regulator-based DTC algorithm uses the motor power in conjunction with the measured capacitor voltages V_{C1} and V_{C2} to select the appropriate small voltage vectors. For example, if V_{S1} is chosen, ΔV_C and machine power are positive, then switching state POO is selected. This will result in the discharging of C_1 and charging of C_2, thus reducing $|\Delta V_c|$.

5.3.5 Robustness to parameter variations

It is apparent that the gains of the PI torque controller are dependent on the machine parameters. To investigate the robustness of the proposed torque controller to machine parameter variations, the performance of the torque controller with detuning in the stator resistance R_s and in the $q-$axis inductance L_q are carried out. For this investigation R_s is increased above its nominal value of 100% to emulate increasing resistance with temperature, and L_q is decreased below its nominal value to mimic saturation. Figure 5.4 shows the dynamic torque with different R_s and nominal L_q, while Figure 5.5 shows the response with different L_q and nominal R_s. From these results, it is apparent that the torque response is largely insensitive to parameter variations, illustrating the robustness of the proposed technique.

For any variation in R_s, the transfer function of the torque controller in (5.12) can be expressed as

$$G(s) = \frac{\left(2\xi\omega_n - \frac{R_s}{L_q}\right)s + \omega_n^2}{s^2 + \left(2\xi\omega_n + \frac{R_{s(real)} - R_s}{L_q}\right)s + \omega_n^2} \tag{5.19}$$

where $R_{s(real)}$ is the real value of the stator resistance. By comparing the characteristic

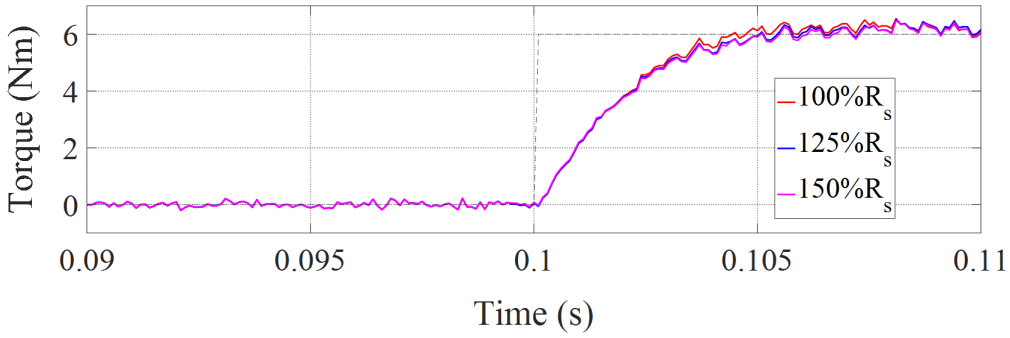

Figure 5.4: Simulation results of the torque dynamics with different detuning in the stator resistance for the torque-regulator-based DTC strategy.

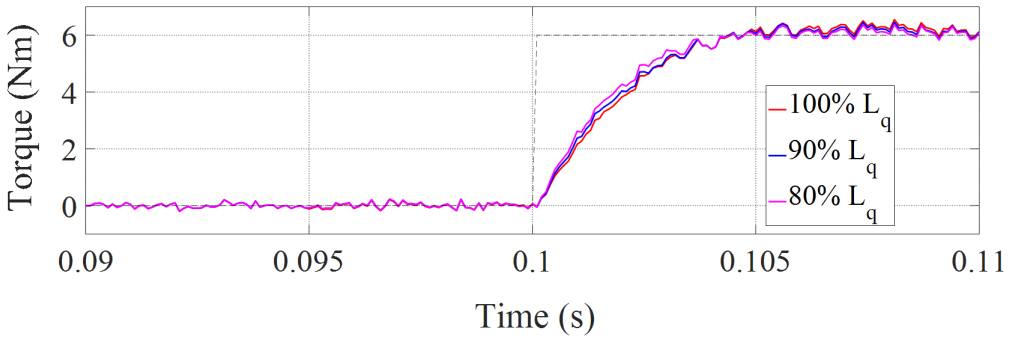

Figure 5.5: Simulation results of the torque dynamics with different detuning in the $q-$axis inductance for the torque-regulator-based DTC strategy

equation of (5.19) and (5.12), it can be seen that the actual damping ratio in (5.19) is increased by the term $\left(R_{s(real)} - R_s\right) / \left(2\omega_n L_q\right)$ which is usually very small, while the natural frequency remains the same. Therefore, the overshoot is marginally reduced while maintaining the rise time for the detuning of R_s as shown in Figure 5.4.

For any variation in L_q, the transfer function of the torque controller can be expressed as

$$G(s) = \frac{\frac{L_q}{L_{q(real)}}\left[\left(2\xi\omega_n - \frac{R_s}{L_q}\right)s + \omega_n^2\right]}{s^2 + \frac{L_q}{L_{q(real)}}2\xi\omega_n + \frac{L_q}{L_{q(real)}}\omega_n^2} \tag{5.20}$$

By comparing the denominator of (5.20) to (5.12), it can be seen that the actual damping ratio and natural frequency are increased by a factor of $\left(L_{q(real)}/L_q\right)^{\frac{1}{2}}$. As a result, the overshoot and rise time are reduced for the detuning of L_q as shown in Figure 5.5.

5.4 Experimental results

In this section, experimental results are presented to verify the steady-state and transient performance of the proposed torque-regulator-based DTC strategy. For comparison purposes, the performance of the DTC strategy without torque regulator control is also

presented. Experimental setup and machine parameters are shown in appendix A. The switching frequency of the proposed strategy is 1.5 kHz while the sampling frequency for both strategies is 10 kHz.

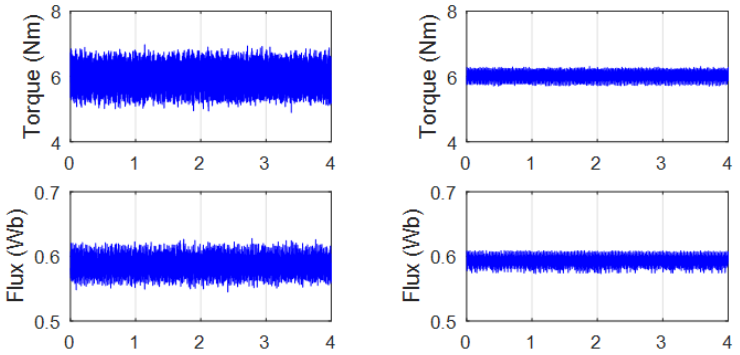

Figure 5.6: Steady-state torque and stator flux at 200 rpm under the DTC strategy (a) without and (b) with torque regulator.

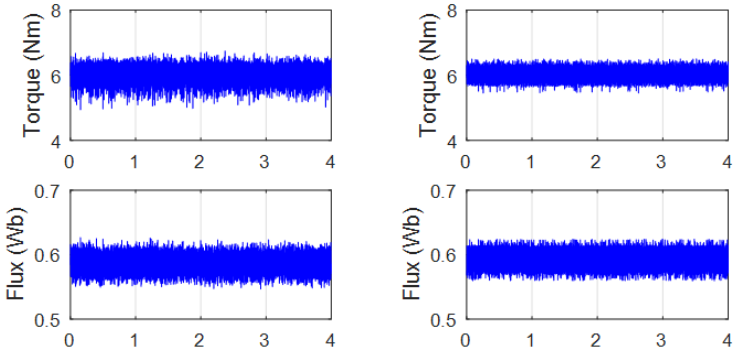

Figure 5.7: Steady-state torque and stator flux at 1000 rpm under the DTC strategy (a) without and (b) with torque regulator.

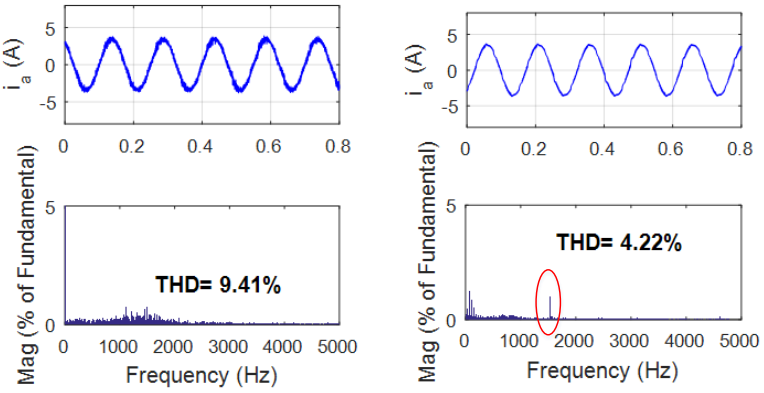

Figure 5.8: Stator flux and its THD at 200 rpm under the DTC strategy (a) without and (b) with torque regulator.

5.4.1 Steady-state Performance

Figure 5.6 presents the steady-state torque responses at 200 rpm with a rated load of 6 Nm. It can be seen that the torque ripples are significantly reduced for the proposed torque-regulator based DTC strategy. Numerically, the torque ripples are reduced by more than 50% compared to that of the DTC strategy without the torque regulator. However, this reduction is less significant at high operating speeds, as shown in Figure 5.7, for which the back EMF is large compared to the applied voltage.

Figure 5.8 and 5.9 illustrate the stator current and its total harmonic distortion (THD) at 200 rpm and 1000 rpm at rated load. It can be seen that the THD of the stator current are smaller for the proposed torque-regulator-based DTC strategy. The frequency spectrum shows the dominant harmonic at 1.5 kHz which corresponds with the switching frequency.

Figure 5.10 shows the DC-link capacitor voltages at different operating speeds. From Figure 5.10, it can be deduced that while the capacitor voltages are well balanced for both strategies, the torque-regulator-based DTC strategy shows smaller capacitor voltage

fluctuation at the steady-state due to lower harmonic content in the stator currents.

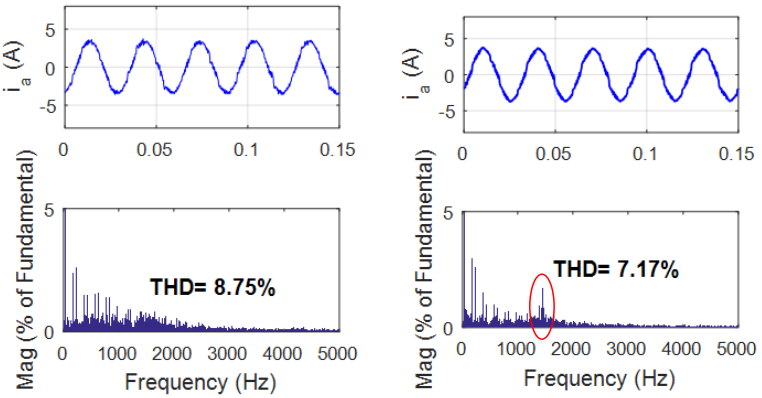

Figure 5.9: Stator flux and its THD at 1000 rpm under the DTC strategy (a) without and (b) with torque regulator.

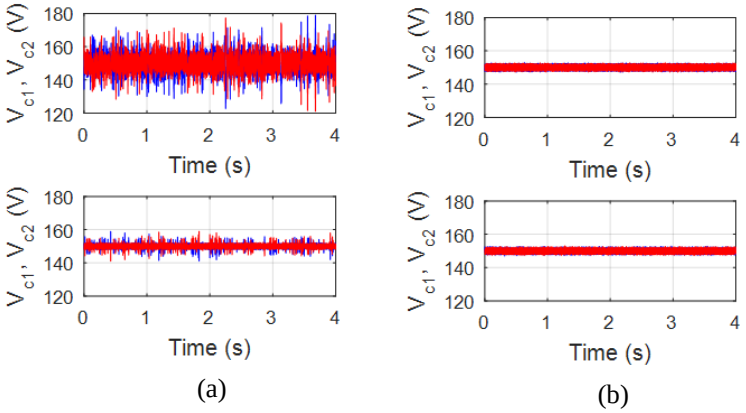

Figure 5.10: DC-link capacitor voltage at 200rpm (top) and 1000 rpm (bottom) under the DTC strategy (a) without and (b) with torque regulator.

5.4.2 Transient Performance

The excellent dynamic response of the proposed drive can be appreciated from Figure 5.11. Figure 5.11 shows drive acceleration from -1000 rpm to +1000 rpm at no-load.

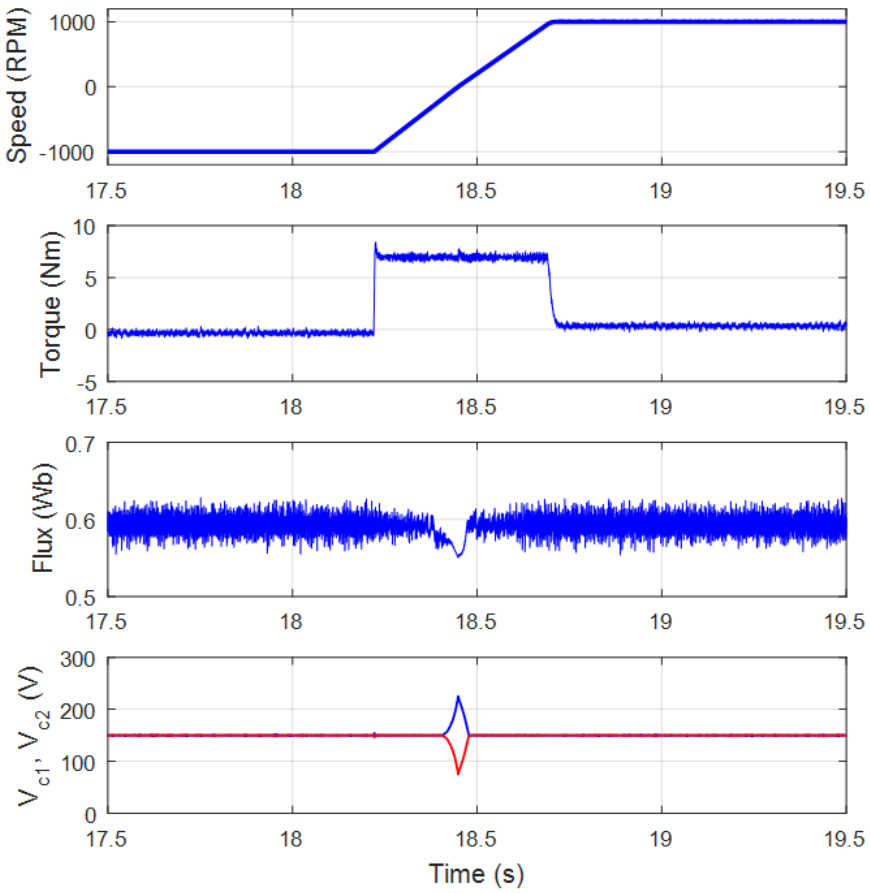

Figure 5.11: Speed, torque, stator flux and DC-link capacitor voltages during speed reversal from -1000 rpm to 1000 rpm under the proposed DTC strategy.

Conversely, the transient performance of the drive with sudden full-load application is depicted in Figure 5.12. In both cases, the stability of the drive is preserved with excellent torque and flux performance. Simultaneously, the neutral point voltage balance is maintained. In the instance of motor acceleration in Figure 5.11, the capacitor voltages initially deviate, before rapidly converging. Load application ostensibly has very little effect on the neutral point voltage, as can be seen from Figure 5.12. The capacitor voltages exhibit larger fluctuations as the load is applied, because the motor current increases. Consequently, the larger neutral point current has a greater charging and

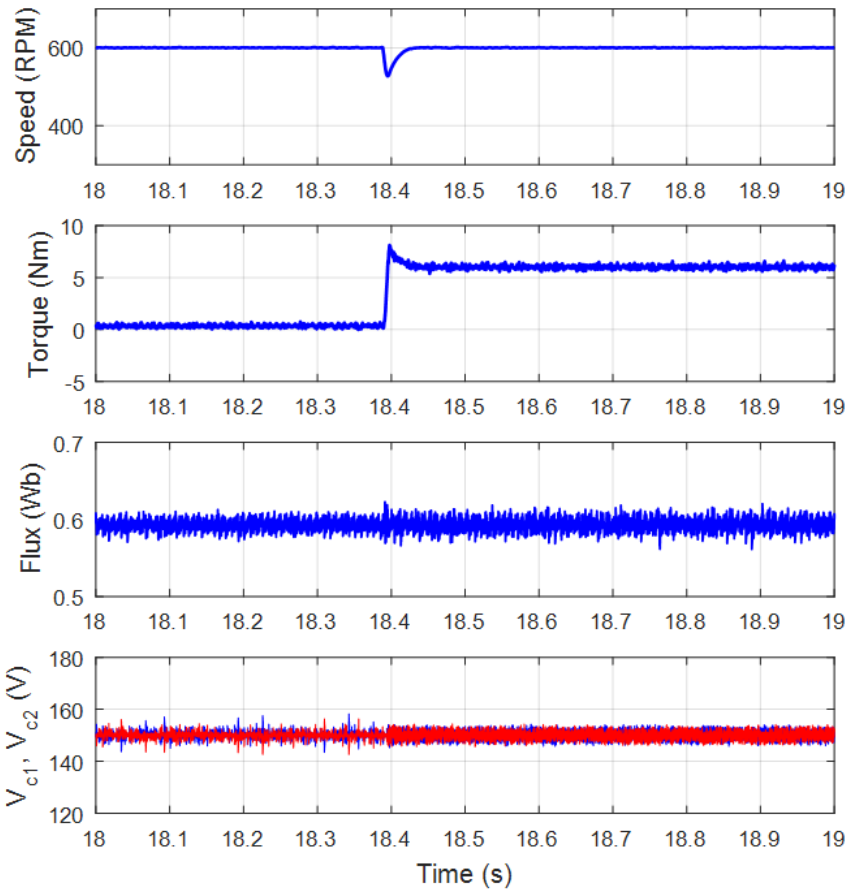

Figure 5.12: Speed, torque, stator flux and DC-link capacitor voltages when a sudden load is applied under the proposed DTC strategy.

discharging effect on the capacitors. Nevertheless, both the capacitor voltages are balanced, within a low tolerance level.

5.5 Conclusion

In this paper, a torque-regulator-based DTC strategy was proposed for an IPMSM driven from a 3L-SNPC inverter. Compared to the DTC strategy without torque regulator, the proposed method significantly reduces the torque ripples and attains a constant

switching frequency. By using a PI torque controller, a large rate of torque variation was negated. A constant switching frequency was achieved through a simple four periodic triangular-carriers. Neutral point voltage balancing was incorporated into the proposed algorithm. The experimental results show a significant improvement in the torque ripples, thereby confirming the effectiveness of the proposed method.

Chapter 6

A SVM-Based Dead-beat Predictive Torque Control for the 3L-SNPC Inverter-fed IPMSM Drives

In chapter 4, a duty-cycle-control-based PTC approach have been proposed for IPMSM driven by a 3L-SNPC inverter. The basic idea of this approach is to select one optimal voltage vector to minimize the torque and flux errors in the next sampling cycle. To further reduce the torque ripples, a duty cycle control is implemented. With the knowledge of the torque error and speed of the motor, the duration of the application of the optimal voltage vector within one sampling cycle is calculated. A different voltage vector is then applied for the remainder of the sampling cycle. The voltage vectors are selected to minimize the torque ripples and simultaneously balance the two DC-link capacitor voltages. However, to realize online optimization, the effects of different voltage vectors are iteratively calculated and compared. This implies high computational burden since the prediction and cost function evaluation have to be done for all thirteen voltage vectors. Furthermore, inverter switching frequency is still variable.

To solve the afore-mentioned problems, this chapter proposes a deadbeat PTC (DB-PTC) strategy for IPMSM drives using space vector modulation (SVM). The proposed DB-PTC strategy maintains low computational complexity since iterative optimization is not needed. Moreover, it fully exploits the advantage of 3L-SNPC inverter while ensuring smooth voltage vector transition and minimizing switching losses through a novel SVM scheme. The SVM algorithm is developed specifically for the 3L-SNPC inverter, and that overcomes the problem of a lack of medium voltage vectors. The algorithm involves selecting the switching sequence in a manner to assure pole voltages can only change by one voltage level at most during each voltage vector transition. In addition, the algorithm assures that all reference voltage vectors confined to the hexagonal limit of the inverter can be synthesized. Further, the neutral point voltage balancing within a low tolerance level is guaranteed, while continuously generating the reference voltage vector.

The rest of this chapter is organized as follows: Section 6.1 presents the mathematical model of IPMSM and the proposed DB-PTC. Then, the proposed novel SVM for 3L-SNPC inverter is presented in section 6.2. Experimental results are shown in section 6.3 to demonstrate the effectiveness of the proposed method. Finally, the conclusion is drawn in section 6.6.

6.1 The Proposed DB-PTC Strategy

The IPMSM can be modelled in the stationary $(\alpha - \beta)$ reference frame as

$$L_q \frac{d\boldsymbol{i_s}}{dt} = -R_s \boldsymbol{i_s} + j\omega_{re}(\boldsymbol{\lambda_s} - L_q \boldsymbol{i_s}) + \boldsymbol{v_s} \tag{6.1}$$

$$\frac{d\boldsymbol{\lambda_s}}{dt} = \boldsymbol{v_s} - R_s \boldsymbol{i_s} \tag{6.2}$$

$$\boldsymbol{T_e} = \frac{3}{2} P(\boldsymbol{\lambda_s} \times \boldsymbol{i_s}) \tag{6.3}$$

where $\boldsymbol{v_s}$ stator voltage vector with $\boldsymbol{v_s} = \begin{bmatrix} v_{s\alpha} & v_{s\beta} \end{bmatrix}^T$

$\boldsymbol{i_s}$ stator current vector with $\boldsymbol{i_s} = \begin{bmatrix} i_{s\alpha} & i_{s\beta} \end{bmatrix}^T$

$\boldsymbol{\lambda_s}$ stator flux linkage vector with $\boldsymbol{\lambda_s} = \begin{bmatrix} \lambda_{s\alpha} & \lambda_{s\beta} \end{bmatrix}^T$

By discretizing (6.1)-(6.3) via forward Euler method and re-writing them in scalar forms, equations (6.4)-(6.6) can be derived.

$$\begin{bmatrix} i_{s\alpha}^{k+1} \\ i_{s\beta}^{k+1} \end{bmatrix} = \begin{bmatrix} 1 - \frac{R_s}{L_q} T_s & -\omega_{re} T_s \\ \omega_{re} T_s & 1 - \frac{R_s}{L_q} T_s \end{bmatrix} \begin{bmatrix} i_{s\alpha}^{k} \\ i_{s\beta}^{k} \end{bmatrix} + \begin{bmatrix} 0 & \frac{\omega_{re}}{L_q} T_s \\ -\frac{\omega_{re}}{L_q} T_s & 0 \end{bmatrix} \begin{bmatrix} \lambda_{s\alpha}^{k} \\ \lambda_{s\beta}^{k} \end{bmatrix} + \frac{T_s}{L_q} \begin{bmatrix} v_{s\alpha}^{k} \\ v_{s\beta}^{k} \end{bmatrix} \tag{6.4}$$

$$\begin{bmatrix} \lambda_{s\alpha}^{k+1} \\ \lambda_{s\beta}^{k+1} \end{bmatrix} = \begin{bmatrix} \lambda_{s\alpha}^{k} \\ \lambda_{s\beta}^{k} \end{bmatrix} + T_s \left(\begin{bmatrix} v_{s\alpha}^{k} \\ v_{s\beta}^{k} \end{bmatrix} - R_s \begin{bmatrix} i_{s\alpha}^{k} \\ i_{s\beta}^{k} \end{bmatrix} \right) \tag{6.5}$$

$$T_e^{k+1} = \frac{3}{2} P \left[\lambda_{s\alpha}^{k+1} i_{s\beta}^{k+1} - \lambda_{s\beta}^{k+1} i_{s\alpha}^{k+1} \right] \tag{6.6}$$

where notations k and T_s represent the $k-$th sampling instant and the controller sampling period, respectively.

In real-time digital control, the presence of one-step delay usually leads to increased torque and flux ripples [23]. To compensate for this effect, the torque and flux should be predicted for one more step, i.e. the prediction of $\boldsymbol{\lambda_s}^{k+2}$ and T_e^{k+2} are needed. The torque and flux prediction at the sampling cycle $k+2$ can therefore be calculated as

$$T_e^{k+2} = \frac{3}{2} P \left[\lambda_{s\alpha}^{k+2} i_{s\beta}^{k+2} - \lambda_{s\beta}^{k+2} i_{s\alpha}^{k+2} \right] \tag{6.7}$$

$$|\lambda_s^{k+2}| = \sqrt{(\lambda_{s\alpha}^{k+2})^2 + (\lambda_{s\beta}^{k+2})^2} \tag{6.8}$$

where the prediction value of the stator flux $\boldsymbol{\lambda_s}^{k+2}$, and stator current $\boldsymbol{i_s}^{k+2}$ are obtained

as

$$\begin{bmatrix} i_{s\alpha}^{k+2} \\ i_{s\beta}^{k+2} \end{bmatrix} = \begin{bmatrix} 1-\frac{R_s}{L_q}T_s & -\omega_{re}T_s \\ \omega_{re}T_s & 1-\frac{R_s}{L_q}T_s \end{bmatrix} \begin{bmatrix} i_{s\alpha}^{k+1} \\ i_{s\beta}^{k+1} \end{bmatrix} + \begin{bmatrix} 0 & \frac{\omega_{re}}{L_q}T_s \\ -\frac{\omega_{re}}{L_q}T_s & 0 \end{bmatrix} \begin{bmatrix} \lambda_{s\alpha}^{k+1} \\ \lambda_{s\beta}^{k+1} \end{bmatrix} + \frac{T_s}{L_q} \begin{bmatrix} v_{s\alpha}^{k+1} \\ v_{s\beta}^{k+1} \end{bmatrix} \tag{6.9}$$

$$\begin{bmatrix} \lambda_{s\alpha}^{k+2} \\ \lambda_{s\beta}^{k+2} \end{bmatrix} = \begin{bmatrix} \lambda_{s\alpha}^{k+1} \\ \lambda_{s\beta}^{k+1} \end{bmatrix} + T_s \left(\begin{bmatrix} v_{s\alpha}^{k+1} \\ v_{s\beta}^{k+1} \end{bmatrix} - R_s \begin{bmatrix} i_{s\alpha}^{k+1} \\ i_{s\beta}^{k+1} \end{bmatrix} \right) \tag{6.10}$$

Based on the relations $T_e^* = T_e^{k+2}$ and $|\lambda_s^*| = |\lambda_s^{k+2}|$ imposed by deadbeat technique, the expressions of $v_{s\alpha}^{k+1}$ and $v_{s\beta}^{k+1}$ can be derived correspondingly. This is because the values of two variables can be fixed with the presence of two governing equations. As a consequence, the desired reference voltage vector can be directly computed, eliminating the necessity of iteratively searching for the optimal voltage vector [14]. This contributes to greatly reduce the computational burden especially for multilevel inverter fed machine drives with numerous candidate voltage vectors. Theoretically, the application of multiple voltage vectors to precisely synthesize the reference voltage vector in each sampling cycle will generate much smaller torque and flux ripples compared to the usage of only one or two voltage vectors for reference voltage vector synthesis in the previous proposed PTC approaches. For better illustration, the derivation of $v_{s\alpha}^{k+1}$ and $v_{s\beta}^{k+1}$ are given as follows, where notations M_1, M_2, N_1, N_2 are introduced for simplicity.

$$M_1 = \lambda_{s\alpha}^{k+1} - T_s R_s i_{s\alpha}^{k+1} \tag{6.11}$$

$$M_2 = \lambda_{s\beta}^{k+1} - T_s R_s i_{s\beta}^{k+1} \tag{6.12}$$

$$N_1 = \left(1 - \frac{R_s}{L_q}T_s\right) i_{s\alpha}^{k+1} - \omega_{re}T_s i_{s\beta}^{k+1} + \frac{\omega_{re}T_s}{L_q}\lambda_{s\beta}^{k+1} \tag{6.13}$$

$$N_2 = \left(1 - \frac{R_s}{L_q}T_s\right) i_{s\beta}^{k+1} + \omega_{re}T_s i_{s\alpha}^{k+1} - \frac{\omega_{re}T_s}{L_q}\lambda_{s\alpha}^{k+1} \tag{6.14}$$

By using the above notations, the predicted stator current at $(k+2)-$th sampling instant is expressed as

$$i_{s\alpha}^{k+2} = N_1 + \frac{T_s v_{s\alpha}^{k+1}}{L_q} \tag{6.15}$$

$$i_{s\beta}^{k+2} = N_2 + \frac{T_s v_{s\beta}^{k+1}}{L_q} \tag{6.16}$$

Then, the deadbeat torque and flux governing rules are re-expressed as (6.17) and (6.18), respectively.

$$T_e^* = \frac{3P}{2}\left[\left(M_1 + T_s v_{s\alpha}^{k+1}\right) i_{s\beta}^{k+2} - \left(M_2 + T_s v_{s\beta}^{k+1}\right) i_{s\alpha}^{k+2}\right] \tag{6.17}$$

$$|\lambda_s^*| = \sqrt{\left(M_1 + T_s v_{s\alpha}^{k+1}\right)^2 + \left(M_2 + T_s v_{s\beta}^{k+1}\right)^2} \tag{6.18}$$

From (6.17), the relation between $v_{s\alpha}^{k+1}$ and $v_{s\beta}^{k+1}$ can be figured out as

$$v_{s\beta}^{k+1} = \mu_1 + \mu_2 v_{s\alpha}^{k+1} \tag{6.19}$$

where μ_1, μ_2 are constants given by

$$\mu_1 = \frac{\frac{2T_e^*}{3P} - M_1 N_2 + M_2 N_1}{\frac{M_1}{L_q} - N_1} \tag{6.20}$$

$$\mu_2 = \frac{\frac{M_2}{L_q} - N_2}{\frac{M_1}{L_q} - N_1} \tag{6.21}$$

Substituting (6.19) into (6.18) and re-arranging the terms, the voltage vector governing equation is derived as

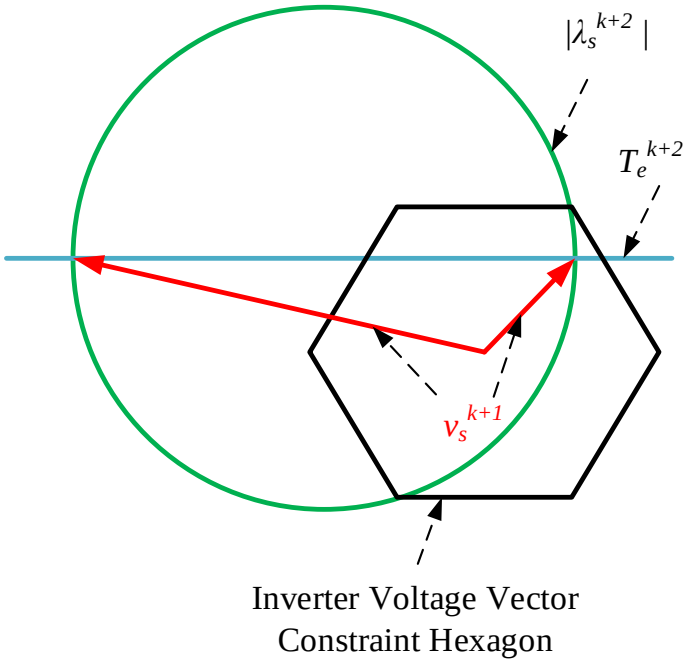

Figure 6.1: Possible voltage vectors and voltage limit imposed by inverter.

$$\left(1+\mu_2^2\right)\left(v_{s\alpha}^{k+1}\right)^2+2\left(M_1+M_2\mu_2+\mu_1\mu_2\right)v_{s\alpha}^{k+1}+ \\ +\left(\mu_1^2+2M_2\mu_1+M_1^2+M_2^2-|\lambda_s^*|^2\right)=0 \quad (6.22)$$

Obviously, there are two solutions for $v_{s\alpha}^{k+1}$. The smaller solution is chosen since the larger one generally results in a synthesized voltage vector that exceeds the voltage limit of DC/AC inverter as illustrated by Figure 6.1. After the determination of $v_{s\alpha}^{k+1}$, $v_{s\beta}^{k+1}$ is obtained via (6.22). Thus, the reference voltage vector is determined and will be subsequently synthesized by SVM.

The block diagram of the proposed DB-PTC strategy is shown in Figure 6.2. The torque and stator flux linkage are estimated from the measured stator currents. The reference voltage vector are determined by the deadbeat predictive torque controller

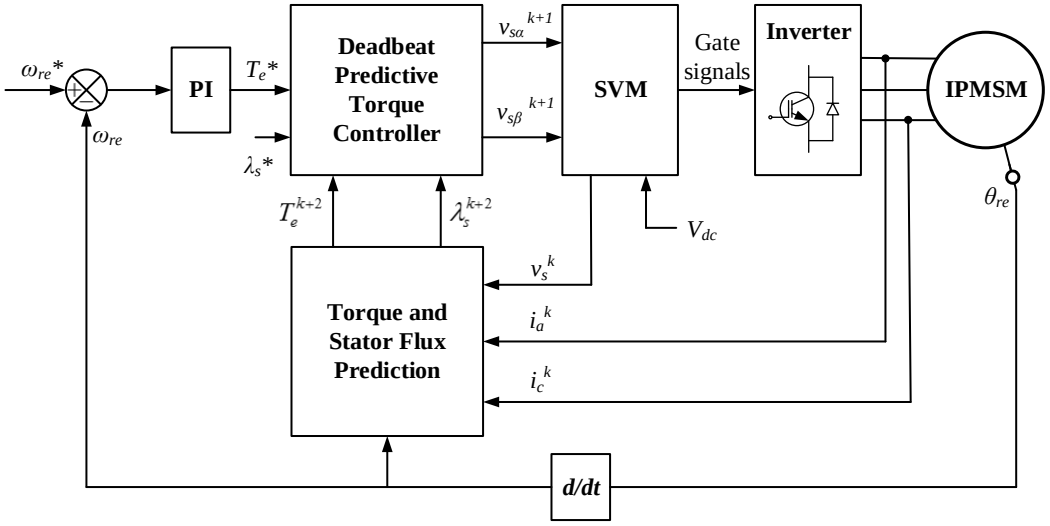

Figure 6.2: Diagram of the proposed DB-PTC strategy.

with knowledge of the torque and flux references. The reference voltage vector are then synthesised using SVM. The speed of the machine is measured, and a PI controller which outputs the torque reference is used for the outer speed control loop.

6.2 Proposed Space Vector Modulation

It is noteworthy that the 3L-SNPC inverter has less possible switching states than T-type and NPC inverters. In particular, medium voltage vectors cannot be generated. This means conventional SVM algorithms [59, 86–101], cannot be applied. So far, this issue has been addressed only in [102], with the report of an SVM technique suited to the 3L-SNPC inverter. This involved dividing each sector of the space vector diagram into two regions, allowing the reference voltage vector to be synthesized using three voltage vectors in a first region, and four in a second. This inevitably means that for some reference voltage vectors, more switching instances than necessary are required if capacitor voltage balancing capability is maximized. In addition, operation under closed loop control was not considered, and experimental results under only one steady-state

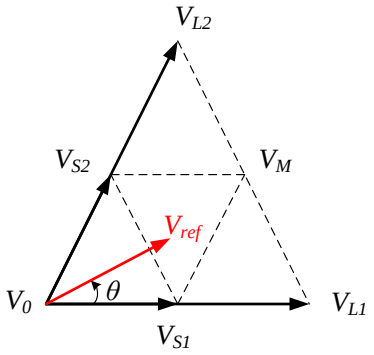

Figure 6.3: Triangular regions in the first sector S_1 of the space voltage vector diagram for the NPC and T-type inverters.

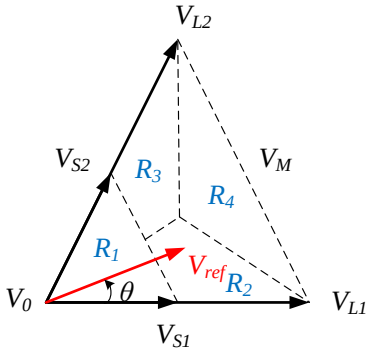

Figure 6.4: Regions in the first sector S_1 of the space voltage vector diagram for the 3L-SNPC inverter

loaded condition were presented. This is important, as the capacitor voltages may not be balanced under all load conditions, especially during load dynamics [58]. The approach proposed in this chapter is an advancement in all these respects.

Essentially, the SVM entails synthesizing the reference voltage vector (V_{ref}), from the three nearest voltage vectors that form the region in which V_{ref} is located. For the NPC and the T-type inverters, the region resembles a triangle and there are a total of four regions within each sector, as shown in Figure 6.3. Without loss of generality,

Region	**Sector**					
	S_1	S_2	S_3	S_4	S_5	S_6
R_1	V_0	V_0	V_0	V_0	V_0	V_0
	V_{S1}	V_{S2}	V_{S3}	V_{S4}	V_{S5}	V_{S6}
	V_{S2}	V_{S3}	V_{S4}	V_{S5}	V_{S6}	V_{S1}
R_2	V_{S1}	V_{S2}	V_{S3}	V_{S4}	V_{S5}	V_{S6}
	V_{S2}	V_{S3}	V_{S4}	V_{S5}	V_{S6}	V_{S1}
	V_{L1}	V_{L2}	V_{L3}	V_{L4}	V_{L5}	V_{L6}
R_3	V_{S1}	V_{S2}	V_{S3}	V_{S4}	V_{S5}	V_{S6}
	V_{S2}	V_{S3}	V_{S4}	V_{S5}	V_{S6}	V_{S1}
	V_{L2}	V_{L3}	V_{L4}	V_{L5}	V_{L6}	V_{L1}
R_4	V_{S1}	V_{S2}	V_{S3}	V_{S4}	V_{S5}	V_{S6}
	V_{S2}	V_{S3}	V_{S4}	V_{S5}	V_{S6}	V_{S1}
	V_{L1}	V_{L2}	V_{L3}	V_{L4}	V_{L5}	V_{L6}
	V_{L2}	V_{L3}	V_{L4}	V_{L5}	V_{L6}	V_{L1}

Table 6.1: Voltage vectors enclosing the four regions in each sector of the 3L-SNPC inverter

only the first sector, S_1, is portrayed. Note that these regional divisions within every sector are only made possible by the existence of the medium voltage vector, V_M. As mentioned above, this approach is inappropriate for the 3L-SNPC inverter, due to the unavailability of medium voltage vectors. Therefore, and given the constraint that pole voltages (v_a, v_b, v_c) are only allowed to change by one level for every voltage vector transition, the sector is divided as shown in Figure 6.4.

6.2.1 Region Determination

In Figure 6.4, sector S_1 is chosen as an example and is divided into four regions of R_1 to R_4. The other sectors can be divided in the same manner using the enclosing voltage vectors as summarized in Table 6.1.

By referring to Figure 6.4, it is seen that regions R_1, R_2, R_3 and R_4 are enclosed by the voltage vectors tabulated in the first column of table 6.1. Hence, for a given reference voltage vector V_{ref}, the determination of its region depends on its magnitude $|V_{ref}|$

and phase angle θ. Define the modulation index $m = \frac{|V_{ref}|}{\frac{2}{3}V_{dc}}$. Then, the constraints that determine the region location of V_{ref} are given by

$$R_1 \colon m \leq \frac{\sqrt{3}}{2\left(\sqrt{3}\cos\theta + \sin\theta\right)}; \quad 0^0 \leq \theta < 60^0 \tag{6.23}$$

$$R_2 \colon \frac{\sqrt{3}}{2\left(\sqrt{3}\cos\theta + \sin\theta\right)} < m \leq \frac{1}{\sqrt{3}\sin\theta + \cos\theta}; \quad 0^0 \leq \theta < 30^0 \tag{6.24}$$

$$R_3 \colon \frac{\sqrt{3}}{2\left(\sqrt{3}\cos\theta + \sin\theta\right)} < m \leq \frac{1}{2\cos\theta}; \quad 30^0 \leq \theta < 60^0 \tag{6.25}$$

$$R_4 \colon \begin{cases} \frac{1}{\sqrt{3}\sin\theta+\cos\theta} < m \leq \frac{\sqrt{3}}{\sqrt{3}\cos\theta+\sin\theta}; & 0^0 \leq \theta < 30^0 \\ \frac{1}{2\cos\theta} < m \leq \frac{\sqrt{3}}{\sqrt{3}\cos\theta+\sin\theta}; & 30^0 \leq \theta < 60^0 \end{cases} \tag{6.26}$$

6.2.2 Duty Cycle Computation

V_{ref} can always be expressed as a vector sum of the individual large, small and zero voltage that parameterize the sector in which V_{ref} dwells.

$$m\angle\theta = \left(d_1 + \frac{d_3}{2}\right)1\angle 0^0 + \left(d_2 + \frac{d_4}{2}\right)1\angle 60^0 + \left(d_0 + \frac{d_3}{2} + \frac{d_4}{2}\right)0 \tag{6.27}$$

where d_1 and d_2 denote the duty cycles of the large voltage vectors V_1 and V_2, respectively, d_3 and d_4 are the duty cycles of the small voltage vectors V_{S1} and V_{S2}, respectively, while d_0 signifies the duty cycle of the zero vector V_0. Individual duty cycles can only take on values in between zero and unity. Moreover, the sum of the duty cycles must always be 1.

$$0 \leq d_0, d_1, d_2, d_3, d_4 \leq 1 \tag{6.28}$$

$$d_0 + d_1 + d_2 + d_3 + d_4 = 1 \tag{6.29}$$

Equation (6.27) can be rewritten as

$$m\angle\theta = D_1\left(1\angle 0^0\right) + D_2\left(1\angle 60^0\right) + D_0(0) \tag{6.30}$$

where,

$$D_1 = d_1 + \frac{d_3}{2} \tag{6.31}$$

$$D_2 = d_2 + \frac{d_4}{2} \tag{6.32}$$

$$D_0 = d_0 + \frac{d_3}{2} + \frac{d_4}{2} \tag{6.33}$$

Note that (6.30) is identical to that of the two level inverter. Thus, the following relationships apply.

$$D_1 = d_1 + \frac{d_3}{2} = \frac{2}{\sqrt{3}} m \sin\left(60^0 - \theta\right) \tag{6.34}$$

$$D_2 = d_2 + \frac{d_4}{2} = \frac{2}{\sqrt{3}} m \sin\theta \tag{6.35}$$

$$D_0 = d_0 + \frac{d_3}{2} + \frac{d_4}{2} = 1 - D_1 - D_2 \tag{6.36}$$

Now, the individual duty cycles are uniquely determined by the region that V_{ref} lies in.

6.2.2.1 Region R_1

If V_{ref} lies in region R_1, voltage vectors V_0, V_{S1} and V_{S2} will be applied with duty cycles d_0, d_3 and d_4, respectively. Consequently, $d_1 = d_2 = 0$ and (6.30)-(6.36) dictate

that

$$d_3 = \frac{4}{\sqrt{3}} m \sin\left(60^0 - \theta\right) \tag{6.37}$$

$$d_4 = \frac{4}{\sqrt{3}} m \sin\theta \tag{6.38}$$

$$d_0 = 1 - \frac{4}{\sqrt{3}} m \left[sin\left(60^0 - \theta\right) - \sin\theta\right] \tag{6.39}$$

6.2.2.2 Region R_2

If V_{ref} is located in region R_2, voltage vectors V_{L1}, V_{S1} and V_{S2} will be applied with duty cycles d_1, d_3 and d_4, respectively. As such, $d_0 = d_2 = 0$ and from (6.30)-(6.36)

$$d_1 = \frac{4}{\sqrt{3}} m \left[sin\left(60^0 - \theta\right) + \sin\theta\right] - 1 \tag{6.40}$$

$$d_3 = 2 - \frac{4}{\sqrt{3}} m \left[sin\left(60^0 - \theta\right) + 2\sin\theta\right] \tag{6.41}$$

$$d_4 = \frac{4}{\sqrt{3}} m \sin\theta \tag{6.42}$$

6.2.2.3 Region R_3

If V_{ref} is situated in region R_3, voltage vectors V_{L2}, V_{S1} and V_{S2} will be applied with duty cycles d_2, d_3 and d_4 respectively. As a result, $d_0 = d_1 = 0$ and (6.30)-(6.36) demand that:

$$d_2 = \frac{4}{\sqrt{3}} m \left[sin\left(60^0 - \theta\right) + \sin\theta\right] - 1 \tag{6.43}$$

$$d_3 = \frac{4}{\sqrt{3}} m \sin\left(60^0 - \theta\right) \tag{6.44}$$

$$d_3 = 2 - \frac{4}{\sqrt{3}} m \left[2sin\left(60^0 - \theta\right) + \sin\theta\right] \tag{6.45}$$

6.2.2.4 Region R_4

If V_{ref} is positioned in region R_4, voltage vectors V_{L1}, V_{L2}, V_{S1} and V_{S2} will be applied with duty cycles d_1, d_2, d_3 and d_4, respectively. Under this circumstance, only $d_0 = 0$ and there are only three independent equations for four independent variables. Mathematically, an infinite number of solutions exist. However, only those satisfying the constraints stipulated by (6.28) and (6.29) are realizable. Thus, the duty cycles d_1, d_2, d_3 and d_4 cannot be chosen at will and further mathematical manipulation is required. With respect to (6.36), define

$$d_3 = 2\lambda D_0 \tag{6.46}$$

$$d_4 = 2\left(1-\lambda\right) D_0 \tag{6.47}$$

where $0 \leq \lambda \leq 1$. Now, according to (6.34) and (6.35),

$$D_1 \geq \frac{d_3}{2} \tag{6.48}$$

$$D_2 \leq \frac{d_4}{2} \tag{6.49}$$

Combining (6.46)-(6.49) with (6.36) yields

$$\frac{1-D_1-2D_2}{1-D_1-D_2} \leq \lambda \leq \frac{D_1}{1-D_1-D_2} \tag{6.50}$$

Since $0 \leq \lambda \leq 1$, the following relation holds

$$max\left(0, \frac{1-D_1-2D_2}{1-D_1-D_2}\right) \leq \lambda \leq min\left(1, \frac{D_1}{1-D_1-D_2}\right) \tag{6.51}$$

Theoretically, any value λ that satisfies (6.51) is realizable. However, note that (6.51) is

a dynamic constraint, as the values D_1 and D_2 change continuously and it is improbable that a static λ value will satisfy (6.51) under all operating conditions. Hence, to ensure that (6.51) is always satisfied, λ is chosen as

$$\lambda = \frac{1}{2}\left(max\left(0, \frac{1 - D_1 - 2D_2}{1 - D_1 - D_2}\right) + min\left(1, \frac{D_1}{1 - D_1 - D_2}\right)\right] \tag{6.52}$$

which is the average value of its upper and lower bounds. The reason is that such an average value tends to balance the application of V_{S1} and V_{S2} through the balancing of their corresponding duty cycle d_3 and d_4. Therefore, it is guaranteed that both of the two small voltage vectors are applied with sufficient time duration during vector transitions instead of using only one of them, respecting the smooth voltage vector switching criteria.

The individual duty cycles d_1, d_2, d_3 and d_4 can now be simultaneously determined from (6.34)-(6.36) ,(6.46) and (6.47) as

$$d_1 = D_1 - \lambda D_0 \tag{6.53}$$

$$d_2 = D_2 - (1 - \lambda) D_0 \tag{6.54}$$

$$d_3 = 2\lambda D_0 \tag{6.55}$$

$$d_4 = 2(1 - \lambda) D_0 \tag{6.56}$$

where D_0, D_1, D_2 are computed by (6.34)-(6.36) using the values of m and θ.

6.2.3 Switching Sequence

To minimize the number of switching events and respect the smooth voltage vector switching criteria [103] at every sampling instant, it is paramount for the SVM to traverse only the adjacent voltage vectors in each region. As such, for each region R_1 to

R_4, the following switching sequence is applied.

$$R_1 : V_0 \rightarrow V_{S1} \rightarrow V_{S2} \rightarrow V_0 \rightarrow V_{S2} \rightarrow V_{S1} \rightarrow V_0 \tag{6.57}$$

$$R_2 : V_{S2} \rightarrow V_{S1} \rightarrow V_{L1} \rightarrow V_{S1} \rightarrow V_{S2} \tag{6.58}$$

$$R_3 : V_{S1} \rightarrow V_{S2} \rightarrow V_{L2} \rightarrow V_{S2} \rightarrow V_{S1} \tag{6.59}$$

$$R_4 : V_{S1} \rightarrow V_{L1} \rightarrow V_{S1} \rightarrow V_{S2} \rightarrow V_{L2} \rightarrow V_{S2} \tag{6.60}$$

The foregoing analysis can be repeated for the remaining five sectors with identical results. Their corresponding voltage vectors are shown in Table 6.1.

6.2.4 Neutral Point Voltage Balancing

The small voltage vectors are used in all the four regions and they can be applied to balance the neutral point voltage. Whenever V_{Si} is applied, an appropriate switching state can be selected according to the difference between the two capacitor voltages $\Delta V_C = V_{C1} - V_{C2}$ and the and the sign of the machine power P_m, to reduce the imbalance. If $\Delta V_C > 0$ and $P_m > 0$, the V_{Si} in Group I will be selected. This will result in the discharging of C_1 and charging of C_2, thus reducing $|\Delta V_C|$. For the case when $\Delta V_C > 0$ and $P_m < 0$, the V_{Si} in Group II will be selected.

6.2.5 Robustness to Parameter Variations

It is clear that the prediction of torque and flux are dependent on the machine parameters. To investigate the robustness of the proposed control method to machine parameter variations, the performance of the predictive torque controller with detuning in the $q-$axis inductance L_q and in the stator resistance R_s are carried out. For this investigation L_q is decreased below its nominal value to mimic saturation, and R_s is increased above its

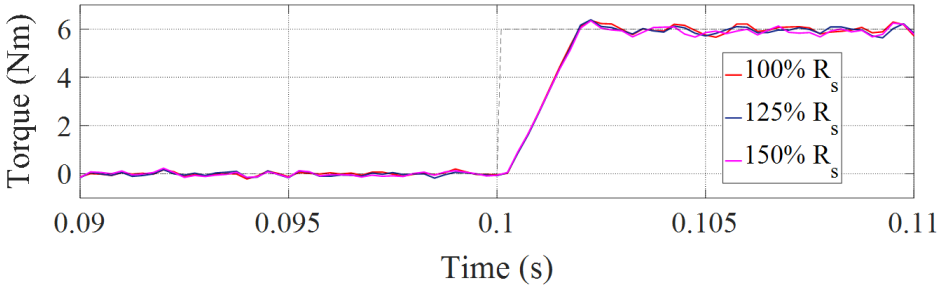

Figure 6.5: Simulation results of the torque dynamics with different detuning in the stator resistance for the DB-PTC strategy.

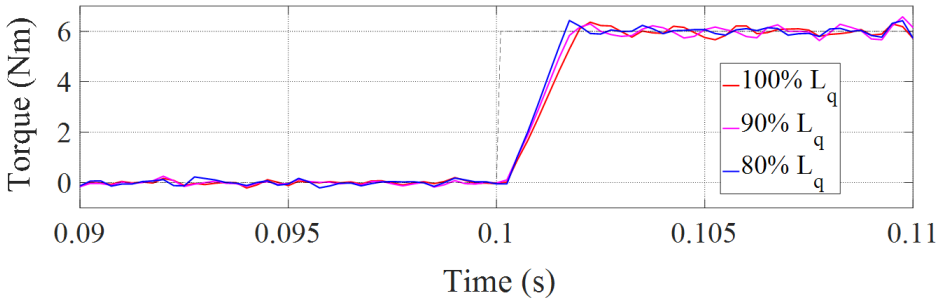

Figure 6.6: Simulation results of the torque dynamics with different detuning in the $q-$axis inductance for the DB-PTC strategy

nominal value of 100% to emulate increasing resistance with temperature. Figure 6.5 shows the dynamic torque with different R_s and nominal L_q, while Figure 6.6 shows the response with different L_q and nominal R_s. From these results, it is apparent that the torque response is largely insensitive to parameter variations, illustrating the robustness of the proposed technique.

6.3 Experimental results

To verify the validity of the proposed method, experiments are carried out in this section. Experimental setup and machine parameters are shown in appendix A. The sampling frequency is set to be 4 kHz. Both the steady-state and transient experimental results

are analyzed.

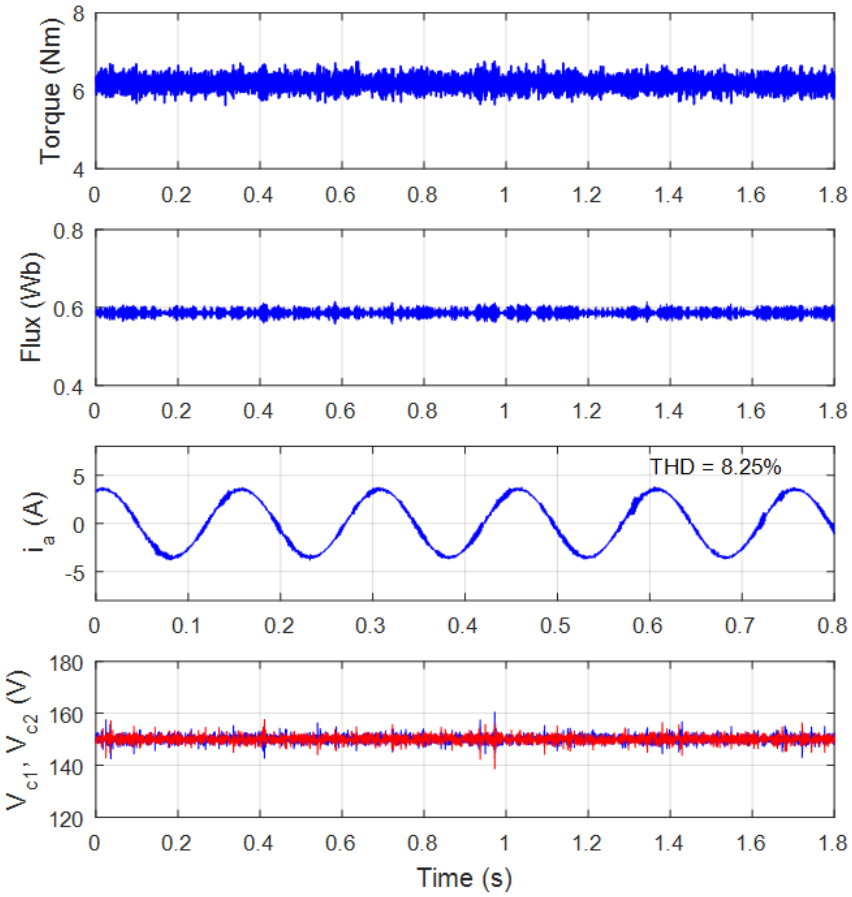

Figure 6.7: Steady-state torque and stator flux at 200 rpm under the DB-PTC strategy.

6.4 Steady-state Performance

Firstly, the steady-state performance of the proposed DB-PTC with SVM is investigated under the rated load of 6 Nm. The tests are carried out for both high speed operation at 1000 rpm and low speed operation at 200 rpm. The results are shown in Figure 6.7 and 6.8, respectively. From Figure 6.7, it is observable that the motor speed, torque

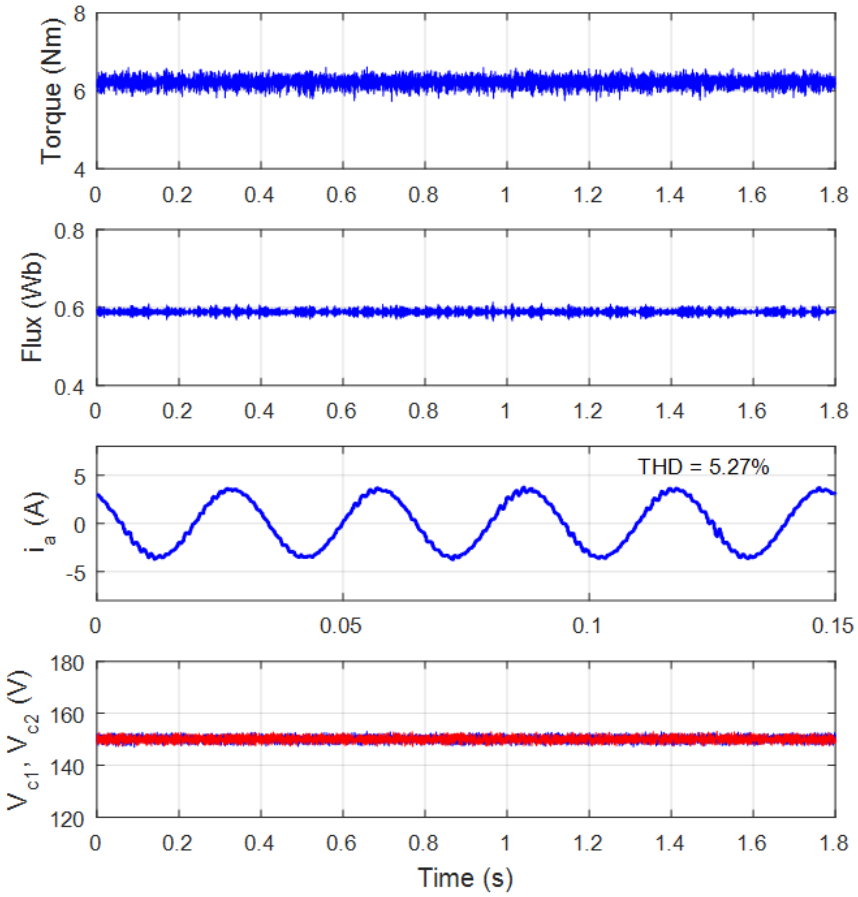

Figure 6.8: Steady-state torque and stator flux at 1000 rpm under the DB-PTC strategy.

and flux are effectively regulated by the proposed DB-PTC. Small torque and flux ripples are achieved by the proposed method under both high speed and low speed operations. Noticeably, the torque and flux ripples are generally higher under low speed operations, which is common for all control approaches due to the low back EMF in low speed region. Moreover, the capacitor voltages V_{C1} and V_{C2} are effectively balanced in steady-states as depicted by the fourth subplots of Figure 6.7 and 6.8. This indicates the effectiveness of the proposed SVM on neutral point voltage balancing.

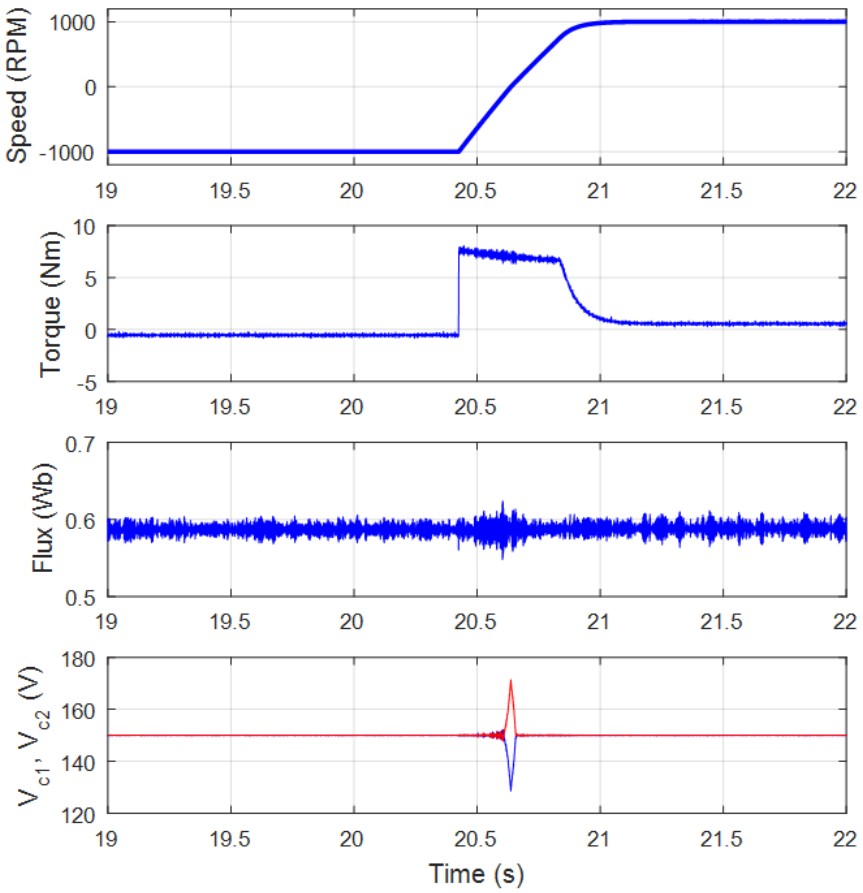

Figure 6.9: Torque and stator flux responses during speed reversal under the DB-PTC strategy.

6.5 Transient Performance

To study the transient speed performance of the proposed method, speed reversal test is carried out. The result is illustrated in Figure 6.9. It is seen from this Figure that the speed, torque, flux as well as the capacitor voltages are well regulated during the transient of speed reversal. Meanwhile, small torque and flux ripples are obtained. Indeed, there are transient imbalances of the capacitor voltages V_{C1} and V_{C2} as shown in the fourth subplot of Figure 6.9. However, the imbalances are controllable since

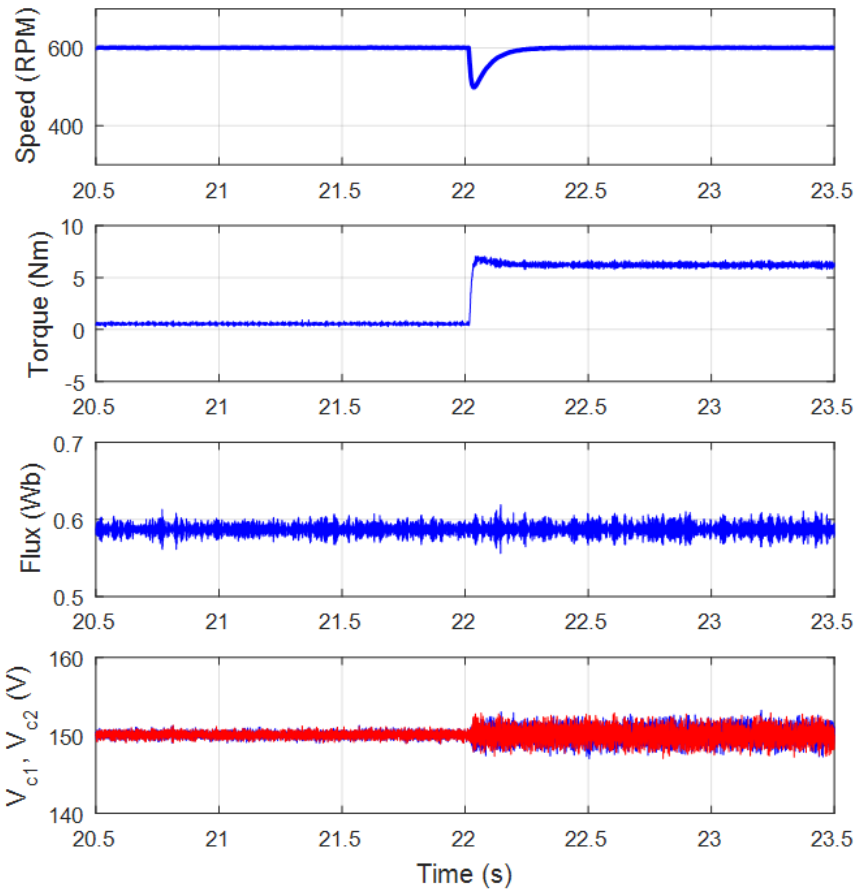

Figure 6.10: Steady-state torque and stator flux at when a sudden load is applied at 600 rpm under the DB-PTC strategy.

the converging of V_{C1} and V_{C2} to their average value is observed to be within tens of milliseconds.

Performance of the proposed SVM based DB-PTC is further examined under the scenario of step load change. The results are shown in Figure 6.10. From this Figure, it is visible that the proposed method achieves smooth speed, torque and flux regulation with balanced capacitor voltages during the transient of full-load step change.

6.6 Conclusion

A DB-PTC strategy for the 3L-SNPC inverter-fed IPMSM drives was proposed in this chapter. The proposed strategy greatly diminishes the torque and flux ripples through the adoption of SVM, predictions and one cycle delay compensation. It requires neither coordinate transformation nor iterative optimization, therefore reducing the computational burden. In addition, the advantage of 3L-SNPC inverter is fully exploited while ensuring smooth voltage vector transition and minimizing switching losses through a novel SVM scheme. The experimental results show small torque and stator flux ripples, thereby confirming the effectiveness of the proposed method.

Chapter 7

A comparison of DTC Strategies for PMSM driven by a 3L-SNPC Inverter

7.1 Introduction

In the previous chapters, several control strategies for the 3L-SNPC inverter-fed IPMSM drive have been presented. Detailed theoretical analysis and experimental verification have been provided to prove the feasibility of each proposed strategy. To further study their performances, a comparison of those strategies is carried out in this chapter. The comparison is conducted on the basis of several criteria: torque and flux ripples, stator current total harmonic distortions, capacitor voltage ripples, and robustness to machine parameters.

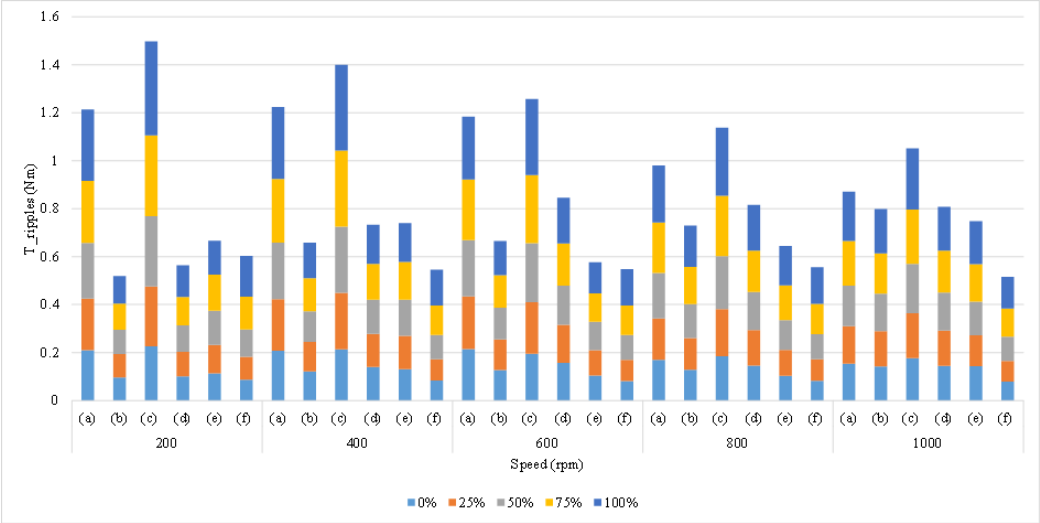

Figure 7.1: Torque ripples at different speeds with 0%, 25%, 50%, 75% and 100% of rated load under the (a) DTC without duty cycle control (b) DTC with duty cycle control (c) PTC without duty cycle control (d) PTC with duty cycle control (e) torque-regulator-based DTC and (f) DB-PTC.

7.2 Comparative Evaluation

7.2.1 Steady-state Performance

Figures 7.1 and 7.2 show the torque and flux ripples at different speeds with 0%, 25%, 50%, 75% and 100% of rated load for all strategies. It can be seen that the torque and flux ripple levels are very similar at low operating speed for the duty-cycle-control-based DTC, duty-cycle-control-based PTC and torque-regulator-based DTC strategies, for which the sampling of the controller is set to be 10 kHz. Numerically, the torque and flux ripples are reduced by more than 50% compared to that of the DTC and PTC strategies without duty cycle control. A similar steady-state torque and flux responses are observed for the DB-PTC strategy. However, it is achieved with such a lower sampling frequency at 4 kHz. At higher operating speed, the proposed duty-cycle-control-based DTC, duty-cycle-control-based PTC and torque-regulator-control based DTC also have identical steady-state torque and flux responses. However, compared

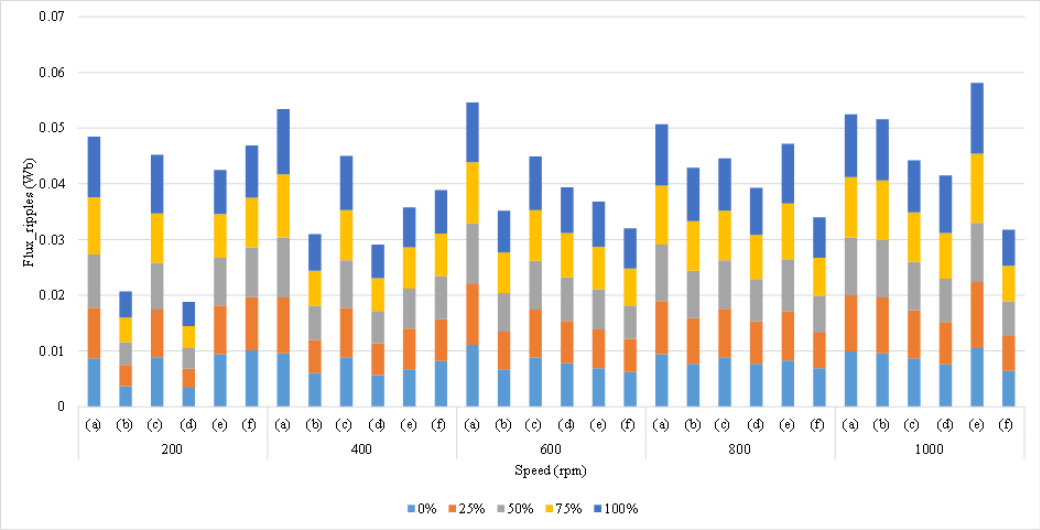

Figure 7.2: Flux ripples at different speeds with 0%, 25%, 50%, 75% and 100% of rated load under the (a) DTC without duty cycle control (b) DTC with duty cycle control (c) PTC without duty cycle control (d) PTC with duty cycle control (e) torque-regulator-based DTC and (f) DB-PTC.

to the DTC and PTC strategies without duty cycle control, the improvement becomes less significant. It is mainly because of the back EMF is large compared to the applied voltage at high operating speed. The smallest torque and flux ripples are observed for the proposed DB-PTC strategy. Clearly, this is achieved through the adoption of SVM.

Figure 7.3 illustrates the total harmonic distortion (THD) of stator current at different operating speeds and load conditions for all proposed strategies. It can be seen that the THD of the stator current are similar for the proposed duty-cycle-control-based DTC, duty-cycle-control-based PTC and torque-regulator-based DTC. Compared to the DTC and PTC strategies without duty cycle control, the reduction in the THD of the stator current is significant. In addition, it can be seen from Figure 7.3 that although the sampling frequency of the DB-PTC strategy is set to be smaller than the remainder strategies, it is still able to produce stator current with a comparable quality at low operating speed and even better at high operating speed.

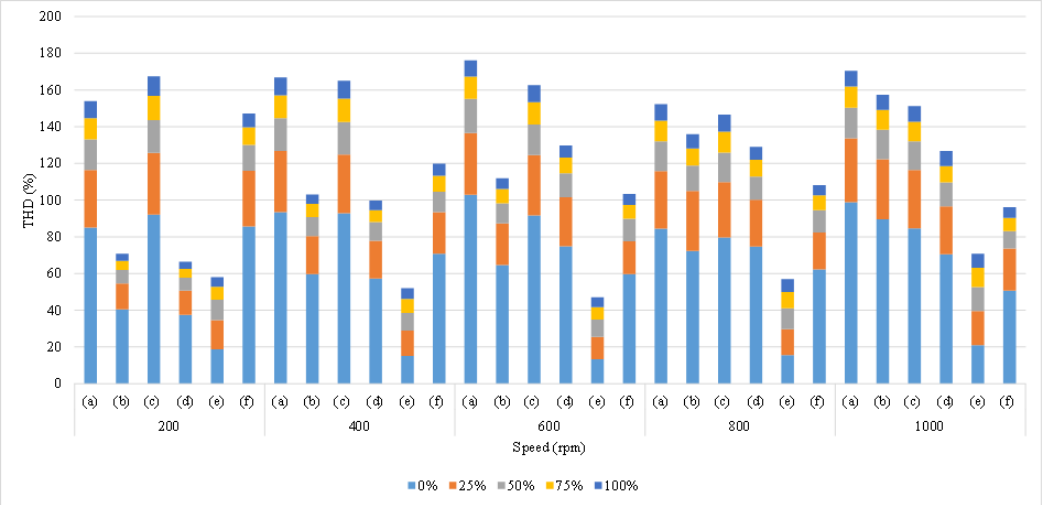

Figure 7.3: Total harmonic distortions of the stator current at different speeds with 0%, 25%, 50%, 75% and 100% of rated load under the (a) DTC without duty cycle control (b) DTC with duty cycle control (c) PTC without duty cycle control (d) PTC with duty cycle control (e) torque-regulator-based DTC and (f) DB-PTC.

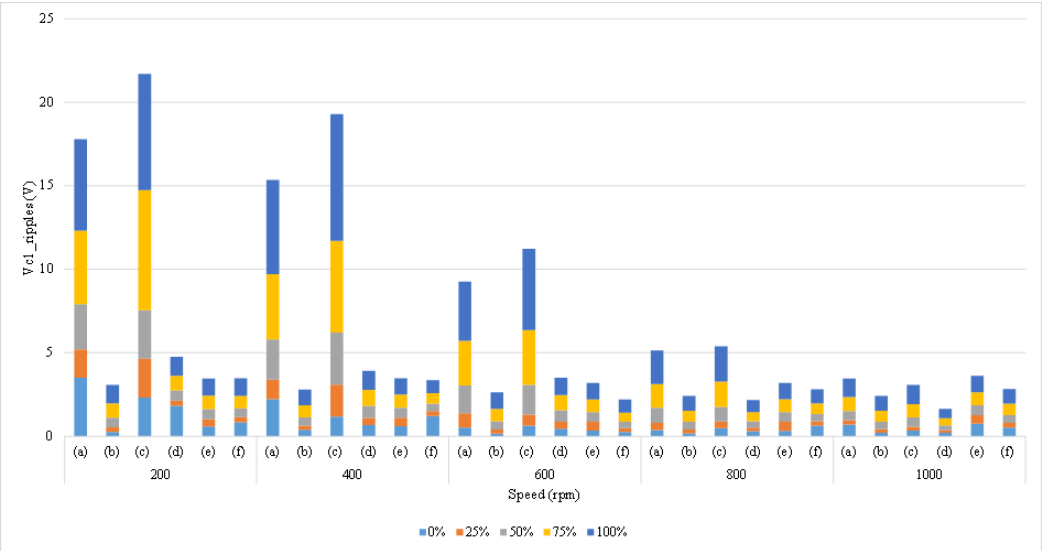

Figure 7.4: Capacitor ripples at different speeds with 0%, 25%, 50%, 75% and 100% of rated load under the (a) DTC without duty cycle control (b) DTC with duty cycle control (c) PTC without duty cycle control (d) PTC with duty cycle control (e) torque-regulator-based DTC and (f) DB-PTC.

Figure 7.4 shows capacitor voltage ripples at different speeds and load conditions for all proposed strategies. Largest capacitor voltage ripples are observed for the DTC and PTC without duty cycle control. Despite different operating speeds and load conditions, the capacitor voltage ripples are minimized for the remainder strategies and while not shown in Figure 7.4, the average capacitor voltages are always maintained equal to half the DC-link voltage of 150 V each.

7.2.2 Dynamic Performance

Figure 7.5 illustrates the dynamic torque reversal from -6 Nm to +6 Nm at zero speed for all proposed strategies. As apparent, the torque-regulator-based DTC strategy gives slowest dynamic torque response among all control strategies. This is due to the nature characteristic of the PI torque controller. In contrast, identical excellent dynamic responses are observed for the remainder strategies.

7.2.3 Robustness to Parameter Variations

It is obvious that the prediction of torque and flux of the proposed DB-PTC and PTC with duty cycle, the gains of the PI torque controller of the torque-regulator-based DTC, and the duty ratio determination of the DTC with duty cycle control strategy are all dependent on the machine parameters. From the results presented in the previous chapters, it is apparent that the torque response is largely insensitive to parameter variations illustrating the robustness of the proposed methods. The DTC without duty cycle control strategy are very robust to parameter variations, due to the use of simple hysteresis controllers.

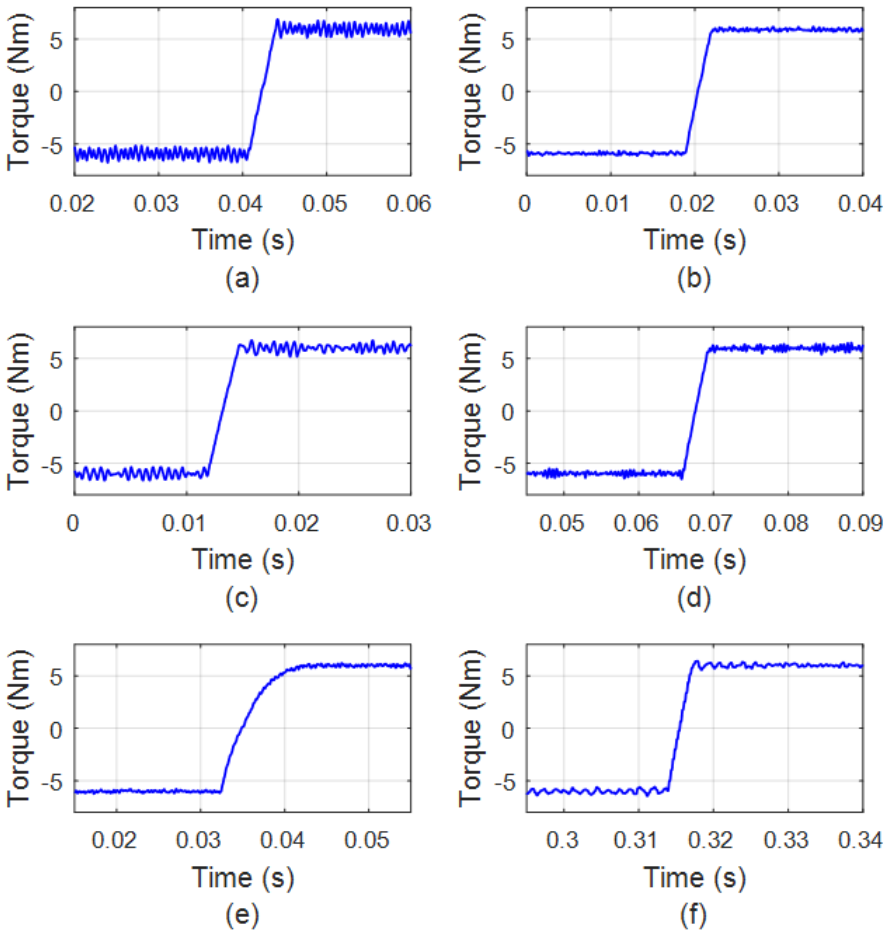

Figure 7.5: Dynamic torque response during torque reversal under the (a) DTC without duty cycle control (b) DTC with duty cycle control (c) PTC without duty cycle control (d) PTC with duty cycle control (e) torque-regulator-based DTC and (f) DB-PTC.

7.3 Conclusion

A performance comparison of all proposed strategies was presented in this chapter. It is proven that the DB-PTC strategy achieves the best steady-state performances at all range of operating speeds while maintains an excellent dynamic response. Both the duty-cycle-control-based DTC and PTC has a very similar performance at steady-state

and dynamic operations. The torque ripples of those strategies are significantly reduced compared to that of the DTC and PTC without duty cycle control at low operating speeds. This reduction is less significant at high operating speeds. A similar steady-state performance is achieved with torque-regulator-based DTC strategy. However, the torque dynamic response is slower because of the presence of the PI torque controller.

Chapter 8

Conclusions and Suggestions for Future Works

8.1 Conclusions

In this thesis, several DTC strategies for IPMSM driven by a 3L-SNPC inverter have been proposed. In comparison to the T-type and NPC inverters, the 3L-SNPC uses fewer switching devices to generate a multilevel waveform. This makes the 3L-SNPC inverter attractive for low-voltage motor drive applications. However, and to date, it has received comparatively little research attention, particularly in relation to suitable control strategies. The work described in this thesis addresses this shortcoming. A summary of analytical and experiment studies carried out and conclusions drawn from these studies are outlined in the rest of this section.

In Chapter 1, an introduction of the EV and IPMSM drives were presented. The main control strategies including FOC, DTC and PTC for IPMSM were also briefly reviewed. Then, a survey on the multilevel inverter topologies for motor drive applications was studied in Chapter 2. The basic working principles and related major issues for each

multilevel topology were also briefly presented. Since this thesis focused on the DTC of IPMSM, a duty-cycle-control-based DTC strategy with torque ripple reduction suited to the 3L-SNPC inverter was first proposed in Chapter 3. It utilised both torque and flux hysteresis controllers, and employed two voltage vectors within each sampling cycle. The duty cycle of each applied voltage vector was calculated with knowledge of the torque error and speed of the rotor. Experimental results were shown this strategy achieved smaller torque and flux ripple than a DTC strategy without duty cycle control.

A second proposed method is based on PTC strategies, as presented in Chapter 4. It utilised knowledge of stator currents and rotor speed in the current state to predict the electromagnetic torque and stator flux in the future state. Then, and accordingly, the most appropriate voltage vector that minimised a predetermined cost function was selected. To further reduce the torque error, the concept of duty-cycle-control was incorporated, in addition to a neutral point balancing technique. However, this proposed method, and that preceding, necessitate operation at a variable switching frequency. To address this issue, a torque-regulator-based DTC and a SVM based DB-PTC strategies were proposed.

As presented in Chapter 5, the proposed torque-regulator-based DTC strategy employed a PI torque controller and four triangular-carriers to attain torque ripple reduction at a constant switching frequency. The hysteresis torque levels were determined by comparing the output of a PI torque controller with four triangular-carriers. With knowledge of the torque and flux levels, an appropriate voltage vector was selected allowing torque and stator flux to be directly controlled. By this method, the PI torque controller negated large rate of torque variations, while periodic triangular-carriers were used to achieve a constant switching frequency.

Alternatively, the proposed DB-PTC strategy achieved a constant switching frequency through the adoption of a novel SVM, as presented in Chapter 6. The desired voltage

vector was determined on the basis of deadbeat control and synthesized using SVM. The proposed SVM algorithm was developed specifically for the 3L-SNPC inverter, and overcomes the problem of a lack of medium voltage vectors for this inverter type. The algorithm involved selecting the switching sequence in a manner to assure pole voltages can only change by one voltage level at most during each voltage vector transition. In addition, the algorithm assured that all reference voltage vectors confined to the hexagonal limit of the inverter could be synthesized. With the adoption of SVM, the torque and flux ripple levels were significantly reduced.

Finally, a comparison of all proposed strategies was undertaken in chapter 7. It was demonstrated that the DB-PTC strategy attains excellent steady-state and dynamic responses at all range of operating speeds and load conditions. Both the duty-cycle-control-based DTC and duty-cycle-control-based PTC strategies had a very similar performances. The torque ripples of those strategies were significantly reduced compared to that of the DTC and PTC without duty cycle control at low operating speeds. However, this reduction was less significant at high operating speeds. A similar steady-state performance was attained with torque regulator based DTC strategy. Nonetheless, the torque dynamic response was sluggish due to the presence of the PI torque controller.

All proposed strategies in this thesis represent a contribution to knowledge. The study has resulted in the publication of two IEEE conference papers and six transactions papers are currently under review, as shown in Appendix B.

8.2 Suggestions for Future Work

The finished work on this thesis focus on the DTC strategies for IPMSM driven by a 3L-SNPC inverter. All proposed strategies are studied thoroughly. However, to further exploits the advantages of the 3L-SNPC inverter for high-efficiency low-voltage

applications, the total switching losses as well as drive efficiency must be considered and compared to that of the T-type inverter-fed IPMSM drives. Moreover, fault detection, diagnostic and tolerant operation for the 3L-SNPC inverter are also important and should be investigated in the future.

References

[1] Z. Yang, F. Shang, I. P. Brown, and M. Krishnamurthy, "Comparative study of interior permanent magnet, induction, and switched reluctance motor drives for ev and hev applications," *IEEE Transactions on Transportation Electrification*, vol. 1, no. 3, pp. 245–254, Oct 2015.

[2] Y. Lin, K. Hu, T. Yeh, and C. Liaw, "An electric-vehicle ipmsm drive with interleaved front-end dc/dc converter," *IEEE Transactions on Vehicular Technology*, vol. 65, no. 6, pp. 4493–4504, June 2016.

[3] A. Choudhury, P. Pillay, and S. S. Williamson, "Modified dc-bus voltage-balancing algorithm based three-level neutral-point-clamped ipmsm drive for electric vehicle applications," *IEEE Transactions on Industrial Electronics*, vol. 63, no. 2, pp. 761–772, Feb 2016.

[4] E. Sulaiman, T. Kosaka, and N. Matsui, "High power density design of 6-slot–8-pole hybrid excitation flux switching machine for hybrid electric vehicles," *IEEE Transactions on Magnetics*, vol. 47, no. 10, pp. 4453–4456, Oct 2011.

[5] T. D. Do, H. H. Choi, and J. Jung, "Nonlinear optimal dtc design and stability analysis for interior permanent magnet synchronous motor drives," *IEEE/ASME Transactions on Mechatronics*, vol. 20, no. 6, pp. 2716–2725, Dec 2015.

[6] F. Blaschke, "The principle of field orientation as applied to the new transvektor closed-loop control system for rotating-field machines," *Siemens Review*, vol. 34, pp. 217–220, 1972.

[7] L. Zhong, M. F. Rahman, W. Y. Hu, and K. W. Lim, "Analysis of direct torque control in permanent magnet synchronous motor drives," *IEEE Transactions on Power Electronics*, vol. 12, no. 3, pp. 528–536, May 1997.

[8] L. Zhong, M. F. Rahman, W. Y. Hu, K. W. Lim, and M. A. Rahman, "A direct torque controller for permanent magnet synchronous motor drives," *IEEE Transactions on Energy Conversion*, vol. 14, no. 3, pp. 637–642, Sept 1999.

[9] Y. Ren, Z. Q. Zhu, and J. Liu, "Direct torque control of permanent-magnet synchronous machine drives with a simple duty ratio regulator," *IEEE Transactions on Industrial Electronics*, vol. 61, no. 10, pp. 5249–5258, Oct 2014.

[10] Y. Zhang and J. Zhu, "A novel duty cycle control strategy to reduce both torque and flux ripples for dtc of permanent magnet synchronous motor drives with switching frequency reduction," *IEEE Transactions on Power Electronics*, vol. 26, no. 10, pp. 3055–3067, Oct 2011.

[11] C. Xia, J. Zhao, Y. Yan, and T. Shi, "A novel direct torque control of matrix converter-fed pmsm drives using duty cycle control for torque ripple reduction," *IEEE Transactions on Industrial Electronics*, vol. 61, no. 6, pp. 2700–2713, June 2014.

[12] D. Mohan, X. Zhang, and G. H. B. Foo, "A simple duty cycle control strategy to reduce torque ripples and improve low-speed performance of a three-level inverter fed dtc ipmsm drive," *IEEE Transactions on Industrial Electronics*, vol. 64, no. 4, pp. 2709–2721, April 2017.

[13] J. S. Lee, C. Choi, J. Seok, and R. D. Lorenz, "Deadbeat-direct torque and flux control of interior permanent magnet synchronous machines with discrete time stator current and stator flux linkage observer," *IEEE Transactions on Industry Applications*, vol. 47, no. 4, pp. 1749–1758, July 2011.

[14] Y. Wang, X. Wang, W. Xie, F. Wang, M. Dou, R. M. Kennel, R. D. Lorenz, and D. Gerling, "Deadbeat model-predictive torque control with discrete space-vector modulation for pmsm drives," *IEEE Transactions on Industrial Electronics*, vol. 64, no. 5, pp. 3537–3547, May 2017.

[15] A. H. Abosh, Z. Q. Zhu, and Y. Ren, "Reduction of torque and flux ripples in space vector modulation-based direct torque control of asymmetric permanent magnet synchronous machine," *IEEE Transactions on Power Electronics*, vol. 32, no. 4, pp. 2976–2986, April 2017.

[16] Z. Zeng, C. Zhu, X. Jin, W. Shi, and R. Zhao, "Hybrid space vector modulation strategy for torque ripple minimization in three-phase four-switch inverter-fed pmsm drives," *IEEE Transactions on Industrial Electronics*, vol. 64, no. 3, pp. 2122–2134, March 2017.

[17] H. Zhu, X. Xiao, and Y. Li, "Torque ripple reduction of the torque predictive control scheme for permanent-magnet synchronous motors," *IEEE Transactions on Industrial Electronics*, vol. 59, no. 2, pp. 871–877, Feb 2012.

[18] Y. Cho, K. Lee, J. Song, and Y. I. Lee, "Torque-ripple minimization and fast dynamic scheme for torque predictive control of permanent-magnet synchronous motors," *IEEE Transactions on Power Electronics*, vol. 30, no. 4, pp. 2182–2190, April 2015.

[19] Y. Zhang and H. Yang, "Two-vector-based model predictive torque control without weighting factors for induction motor drives," *IEEE Transactions on Power Electronics*, vol. 31, no. 2, pp. 1381–1390, Feb 2016.

[20] M. H. Vafaie, B. M. Dehkordi, P. Moallem, and A. Kiyoumarsi, "A new predictive direct torque control method for improving both steady-state and transient-state operations of the pmsm," *IEEE Transactions on Power Electronics*, vol. 31, no. 5, pp. 3738–3753, May 2016.

[21] Y. Zhang and H. Yang, "Model predictive torque control of induction motor drives with optimal duty cycle control," *IEEE Transactions on Power Electronics*, vol. 29, no. 12, pp. 6593–6603, Dec 2014.

[22] M. H. Vafaie, B. M. Dehkordi, P. Moallem, and A. Kiyoumarsi, "Minimizing torque and flux ripples and improving dynamic response of pmsm using a voltage vector with optimal parameters," *IEEE Transactions on Industrial Electronics*, vol. 63, no. 6, pp. 3876–3888, June 2016.

[23] Y. Zhang and H. Yang, "Generalized two-vector-based model-predictive torque control of induction motor drives," *IEEE Transactions on Power Electronics*, vol. 30, no. 7, pp. 3818–3829, July 2015.

[24] M. Habibullah, D. D. Lu, D. Xiao, and M. F. Rahman, "Finite-state predictive torque control of induction motor supplied from a three-level npc voltage source inverter," *IEEE Transactions on Power Electronics*, vol. 32, no. 1, pp. 479–489, Jan 2017.

[25] Y. Zhang, H. Yang, and B. Xia, "Model predictive torque control of induction motor drives with reduced torque ripple," *IET Electric Power Applications*, vol. 9, no. 9, pp. 595–604, 2015.

[26] S. A. Davari, D. A. Khaburi, and R. Kennel, "An improved fcs–mpc algorithm for an induction motor with an imposed optimized weighting factor," *IEEE Transactions on Power Electronics*, vol. 27, no. 3, pp. 1540–1551, March 2012.

[27] F. Wang, S. A. Davari, Z. Chen, Z. Zhang, D. A. Khaburi, J. Rodríguez, and R. Kennel, "Finite control set model predictive torque control of induction machine with a robust adaptive observer," *IEEE Transactions on Industrial Electronics*, vol. 64, no. 4, pp. 2631–2641, April 2017.

[28] S. Kouro, M. Malinowski, K. Gopakumar, J. Pou, L. G. Franquelo, B. Wu, J. Rodriguez, M. A. Perez, and J. I. Leon, "Recent advances and industrial applications of multilevel converters," *IEEE Transactions on Industrial Electronics*, vol. 57, no. 8, pp. 2553–2580, Aug 2010.

[29] M. Schweizer and J. W. Kolar, "Design and implementation of a highly efficient three-level t-type converter for low-voltage applications," *IEEE Transactions on Power Electronics*, vol. 28, no. 2, pp. 899–907, Feb 2013.

[30] R. Rojas, T. Ohnishi, and T. Suzuki, "Simple structure and control method for a neutral-point-clamped pwm inverter," in *Conference Record of the Power Conversion Conference - Yokohama 1993*, April 1993, pp. 26–31.

[31] M. Kerler, P. Burda, M. Baumann, and M. Lienkamp, "A concept of a high-energy, low-voltage ev battery pack," in *2014 IEEE International Electric Vehicle Conference (IEVC)*, Dec 2014, pp. 1–8.

[32] J. Rodriguez, S. Bernet, B. Wu, J. O. Pontt, and S. Kouro, "Multilevel voltage-source-converter topologies for industrial medium-voltage drives," *IEEE Transactions on Industrial Electronics*, vol. 54, no. 6, pp. 2930–2945, Dec 2007.

[33] L. G. Franquelo, J. Rodriguez, J. I. Leon, S. Kouro, R. Portillo, and M. A. M. Prats, "The age of multilevel converters arrives," *IEEE Industrial Electronics Magazine*, vol. 2, no. 2, pp. 28–39, June 2008.

[34] J. Rodriguez, L. G. Franquelo, S. Kouro, J. I. Leon, R. C. Portillo, M. . M. Prats, and M. A. Perez, "Multilevel converters: An enabling technology for high-power applications," *Proceedings of the IEEE*, vol. 97, no. 11, pp. 1786–1817, Nov 2009.

[35] J. Rodriguez, J.-S. Lai, and F. Z. Peng, "Multilevel inverters: a survey of topologies, controls, and applications," *IEEE Transactions on Industrial Electronics*, vol. 49, no. 4, pp. 724–738, Aug 2002.

[36] R. H. Baker and L. H. Bannister, "Electric power converter," *U.S. Patent 3,867,643*, Feb. 1975.

[37] A. Nabae, I. Takahashi, and H. Akagi, "A new neutral-point-clamped pwm inverter," *IEEE Transactions on Industry Applications*, vol. IA-17, no. 5, pp. 518–523, Sept 1981.

[38] J. Rodriguez, S. Bernet, P. K. Steimer, and I. E. Lizama, "A survey on neutral-point-clamped inverters," *IEEE Transactions on Industrial Electronics*, vol. 57, no. 7, pp. 2219–2230, July 2010.

[39] P. Barbosa, P. Steimer, L. Meysenc, M. Winkelnkemper, J. Steinke, and N. Celanovic, "Active neutral-point-clamped multilevel converters," in *2005 IEEE 36th Power Electronics Specialists Conference*, June 2005, pp. 2296–2301.

[40] E. Burguete, J. López, and M. Zabaleta, "New five-level active neutral-point-clamped converter," *IEEE Transactions on Industry Applications*, vol. 51, no. 1, pp. 440–447, Jan 2015.

[41] J.-S. Lai and F. Z. Peng, "Multilevel converters-a new breed of power converters," *IEEE Transactions on Industry Applications*, vol. 32, no. 3, pp. 509–517, May 1996.

[42] X. Kou, K. A. Corzine, and Y. L. Familiant, "Full binary combination schema for floating voltage source multilevel inverters," *IEEE Transactions on Power Electronics*, vol. 17, no. 6, pp. 891–897, Nov 2002.

[43] X. Yuang, H. Stemmler, and I. Barbi, "Self-balancing of the clamping-capacitor-voltages in the multilevel capacitor-clamping-inverter under sub-harmonic pwm modulation," *IEEE Transactions on Power Electronics*, vol. 16, no. 2, pp. 256–263, March 2001.

[44] M. Malinowski, K. Gopakumar, J. Rodriguez, and M. A. Perez, "A survey on cascaded multilevel inverters," *IEEE Transactions on Industrial Electronics*, vol. 57, no. 7, pp. 2197–2206, July 2010.

[45] C. Meyer, C. Romaus, and R. W. DeDoncker, "Five level neutral-point clamped inverter for a dynamic voltage restorer," in *2005 European Conference on Power Electronics and Applications*, Sept 2005, pp. 9 pp.–P.9.

[46] M. Mazuela, I. Baraia, S. Álvarez, I. Atutxa, and D. Madariaga, "Comprehensive analysis of voltage balancing techniques for 5l-npc converters," in *2013 15th European Conference on Power Electronics and Applications (EPE)*, Sept 2013, pp. 1–10.

[47] T. Bruckner, S. Bernet, and H. Guldner, "The active npc converter and its loss-balancing control," *IEEE Transactions on Industrial Electronics*, vol. 52, no. 3, pp. 855–868, June 2005.

[48] J. Li, A. Q. Huang, Z. Liang, and S. Bhattacharya, "Analysis and design of active npc (anpc) inverters for fault-tolerant operation of high-power electrical drives," *IEEE Transactions on Power Electronics*, vol. 27, no. 2, pp. 519–533, Feb 2012.

[49] L. A. Serpa, P. M. Barbosa, P. K. Steimer, and J. W. Kolar, "Five-level virtual-flux direct power control for the active neutral-point clamped multilevel inverter," in *2008 IEEE Power Electronics Specialists Conference*, June 2008, pp. 1668–1674.

[50] J. Meili, S. Ponnaluri, L. Serpa, P. K. Steimer, and J. W. Kolar, "Optimized pulse patterns for the 5-level anpc converter for high speed high power applications," in *IECON 2006 - 32nd Annual Conference on IEEE Industrial Electronics*, Nov 2006, pp. 2587–2592.

[51] F. Kieferndorf, M. Basler, L. A. Serpa, J. . Fabian, A. Coccia, and G. A. Scheuer, "A new medium voltage drive system based on anpc-5l technology," in *2010 IEEE International Conference on Industrial Technology*, March 2010, pp. 643–649.

[52] P. W. Hammond, "A new approach to enhance power quality for medium voltage ac drives," *IEEE Transactions on Industry Applications*, vol. 33, no. 1, pp. 202–208, Jan 1997.

[53] H. Akagi, "Classification, terminology, and application of the modular multilevel cascade converter (mmcc)," *IEEE Transactions on Power Electronics*, vol. 26, no. 11, pp. 3119–3130, Nov 2011.

[54] O. M. Mueller and J. N. Park, "Quasi-linear igbt inverter topologies," in *Proceedings of 1994 IEEE Applied Power Electronics Conference and Exposition - ASPEC'94*, Feb 1994, pp. 253–259 vol.1.

[55] A. Lesnicar and R. Marquardt, "An innovative modular multilevel converter topology suitable for a wide power range," in *2003 IEEE Bologna Power Tech Conference Proceedings,*, vol. 3, June 2003, pp. 6 pp. Vol.3–.

[56] M. Glinka, "Prototype of multiphase modular-multilevel-converter with 2 mw power rating and 17-level-output-voltage," in *2004 IEEE 35th Annual Power Electronics Specialists Conference (IEEE Cat. No.04CH37551)*, vol. 4, June 2004, pp. 2572–2576 Vol.4.

[57] M. Glinka and R. Marquardt, "A new ac/ac multilevel converter family," *IEEE Transactions on Industrial Electronics*, vol. 52, no. 3, pp. 662–669, June 2005.

[58] N. Celanovic and D. Boroyevich, "A comprehensive study of neutral-point voltage balancing problem in three-level neutral-point-clamped voltage source pwm inverters," *IEEE Transactions on Power Electronics*, vol. 15, no. 2, pp. 242–249, March 2000.

[59] S. Busquets-Monge, J. Bordonau, D. Boroyevich, and S. Somavilla, "The nearest three virtual space vector pwm - a modulation for the comprehensive neutral-point balancing in the three-level npc inverter," *IEEE Power Electronics Letters*, vol. 2, no. 1, pp. 11–15, March 2004.

[60] Y. Zhang, J. Zhu, W. Xu, and Y. Guo, "A simple method to reduce torque ripple in direct torque-controlled permanent-magnet synchronous motor by using vectors with variable amplitude and angle," *IEEE Transactions on Industrial Electronics*, vol. 58, no. 7, pp. 2848–2859, July 2011.

[61] G. H. B. Foo and X. Zhang, "Constant switching frequency based direct torque control of interior permanent magnet synchronous motors with reduced ripples and fast torque dynamics," *IEEE Transactions on Power Electronics*, vol. 31, no. 9, pp. 6485–6493, Sept 2016.

[62] X. Zhang and G. H. B. Foo, "A constant switching frequency-based direct torque control method for interior permanent-magnet synchronous motor drives," *IEEE/ASME Transactions on Mechatronics*, vol. 21, no. 3, pp. 1445–1456, June 2016.

[63] D. Mohan, X. Zhang, and G. H. B. Foo, "Three-level inverter-fed direct torque control of ipmsm with torque and capacitor voltage ripple reduction," *IEEE Transactions on Energy Conversion*, vol. 31, no. 4, pp. 1559–1569, Dec 2016.

[64] ——, "Generalized dtc strategy for multilevel inverter fed ipmsms with constant inverter switching frequency and reduced torque ripples," *IEEE Transactions on Energy Conversion*, vol. 32, no. 3, pp. 1031–1041, Sept 2017.

[65] T. Ngo, G. Foo, C. Baguley, D. Mohan, and Z. Xinan, "A novel direct torque control strategy for interior permanent magnet synchronous motors driven by a three-level simplified neutral point clamped inverter," in *2016 IEEE Energy Conversion Congress and Exposition (ECCE)*, Sept 2016, pp. 1–8.

[66] U. Choi, F. Blaabjerg, and K. Lee, "Reliability improvement of a t-type three-level inverter with fault-tolerant control strategy," *IEEE Transactions on Power Electronics*, vol. 30, no. 5, pp. 2660–2673, May 2015.

[67] U. Choi, H. Lee, and K. Lee, "Simple neutral-point voltage control for three-level inverters using a discontinuous pulse width modulation," *IEEE Transactions on Energy Conversion*, vol. 28, no. 2, pp. 434–443, June 2013.

[68] U. Choi, J. Lee, and K. Lee, "New modulation strategy to balance the neutral-point voltage for three-level neutral-clamped inverter systems," *IEEE Transactions on Energy Conversion*, vol. 29, no. 1, pp. 91–100, March 2014.

[69] I. Boldea, M. C. Paicu, and G. Andreescu, "Active flux concept for motion-sensorless unified ac drives," *IEEE Transactions on Power Electronics*, vol. 23, no. 5, pp. 2612–2618, Sept 2008.

[70] F. Niu, B. Wang, A. S. Babel, K. Li, and E. G. Strangas, "Comparative evaluation of direct torque control strategies for permanent magnet synchronous machines," *IEEE Transactions on Power Electronics*, vol. 31, no. 2, pp. 1408–1424, Feb 2016.

[71] J.-K. Kang and S.-K. Sul, "New direct torque control of induction motor for minimum torque ripple and constant switching frequency," *IEEE Transactions on Industry Applications*, vol. 35, no. 5, pp. 1076–1082, Sept 1999.

[72] M. Pacas and J. Weber, "Predictive direct torque control for the pm synchronous machine," *IEEE Transactions on Industrial Electronics*, vol. 52, no. 5, pp. 1350–1356, Oct 2005.

[73] Y. Zhang and J. Zhu, "Direct torque control of permanent magnet synchronous motor with reduced torque ripple and commutation frequency," *IEEE Transactions on Power Electronics*, vol. 26, no. 1, pp. 235–248, Jan 2011.

[74] M. Preindl and S. Bolognani, "Model predictive direct torque control with finite control set for pmsm drive systems, part 1: Maximum torque per ampere operation," *IEEE Transactions on Industrial Informatics*, vol. 9, no. 4, pp. 1912–1921, Nov 2013.

[75] ——, "Model predictive direct torque control with finite control set for pmsm drive systems, part 2: Field weakening operation," *IEEE Transactions on Industrial Informatics*, vol. 9, no. 2, pp. 648–657, May 2013.

[76] T. Wang, C. Liu, G. Lei, Y. Guo, and J. Zhu, "Model predictive direct torque control of permanent magnet synchronous motors with extended set of voltage space vectors," *IET Electric Power Applications*, vol. 11, no. 8, pp. 1376–1382, 2017.

[77] M. Siami, D. A. Khaburi, M. Rivera, and J. Rodríguez, "A computationally efficient lookup table based fcs-mpc for pmsm drives fed by matrix converters," *IEEE Transactions on Industrial Electronics*, vol. 64, no. 10, pp. 7645–7654, Oct 2017.

[78] A. Mora, . Orellana, J. Juliet, and R. Cárdenas, "Model predictive torque control for torque ripple compensation in variable-speed pmsms," *IEEE Transactions on Industrial Electronics*, vol. 63, no. 7, pp. 4584–4592, July 2016.

[79] W. Xie, X. Wang, F. Wang, W. Xu, R. M. Kennel, D. Gerling, and R. D. Lorenz, "Finite-control-set model predictive torque control with a deadbeat solution for pmsm drives," *IEEE Transactions on Industrial Electronics*, vol. 62, no. 9, pp. 5402–5410, Sept 2015.

[80] X. Zhang and B. Hou, "Double vectors model predictive torque control without weighting factor based on voltage tracking error," *IEEE Transactions on Power Electronics*, vol. 33, no. 3, pp. 2368–2380, March 2018.

[81] M. Siami, D. A. Khaburi, and J. Rodríguez, "Torque ripple reduction of predictive torque control for pmsm drives with parameter mismatch," *IEEE Transactions on Power Electronics*, vol. 32, no. 9, pp. 7160–7168, Sept 2017.

[82] O. Sandre-Hernandez, J. Rangel-Magdaleno, and R. Morales-Caporal, "A comparison on finite-set model predictive torque control schemes for pmsms," *IEEE Transactions on Power Electronics*, vol. 33, no. 10, pp. 8838–8847, Oct 2018.

[83] M. Habibullah, D. D. Lu, D. Xiao, and M. F. Rahman, "A simplified finite-state predictive direct torque control for induction motor drive," *IEEE Transactions on Industrial Electronics*, vol. 63, no. 6, pp. 3964–3975, June 2016.

[84] L. Guo, X. Zhang, S. Yang, Z. Xie, L. Wang, and R. Cao, "Simplified model predictive direct torque control method without weighting factors for permanent magnet synchronous generator-based wind power system," *IET Electric Power Applications*, vol. 11, no. 5, pp. 793–804, 2017.

[85] D. Mohan, X. Zhang, and G. H. B. Foo, "Three-level inverter-fed direct torque control of ipmsm with constant switching frequency and torque ripple reduction," *IEEE Transactions on Industrial Electronics*, vol. 63, no. 12, pp. 7908–7918, Dec 2016.

[86] N. Celanovic and D. Boroyevich, "A fast space-vector modulation algorithm for multilevel three-phase converters," *IEEE Transactions on Industry Applications*, vol. 37, no. 2, pp. 637–641, March 2001.

[87] Y. Deng, K. H. Teo, C. Duan, T. G. Habetler, and R. G. Harley, "A fast and generalized space vector modulation scheme for multilevel inverters," *IEEE Transactions on Power Electronics*, vol. 29, no. 10, pp. 5204–5217, Oct 2014.

[88] Y. Deng, Y. Wang, K. H. Teo, and R. G. Harley, "A simplified space vector modulation scheme for multilevel converters," *IEEE Transactions on Power Electronics*, vol. 31, no. 3, pp. 1873–1886, March 2016.

[89] B. P. McGrath, D. G. Holmes, and T. Lipo, "Optimized space vector switching sequences for multilevel inverters," *IEEE Transactions on Power Electronics*, vol. 18, no. 6, pp. 1293–1301, Nov 2003.

[90] A. K. Gupta and A. M. Khambadkone, "A space vector pwm scheme for multilevel inverters based on two-level space vector pwm," *IEEE Transactions on Industrial Electronics*, vol. 53, no. 5, pp. 1631–1639, Oct 2006.

[91] ——, "A general space vector pwm algorithm for multilevel inverters, including operation in overmodulation range," *IEEE Transactions on Power Electronics*, vol. 22, no. 2, pp. 517–526, March 2007.

[92] A. Lewicki, Z. Krzeminski, and H. Abu-Rub, "Space-vector pulsewidth modulation for three-level npc converter with the neutral point voltage control," *IEEE Transactions on Industrial Electronics*, vol. 58, no. 11, pp. 5076–5086, Nov 2011.

[93] A. K. Gupta and A. M. Khambadkone, "A simple space vector pwm scheme to operate a three-level npc inverter at high modulation index including overmodulation region, with neutral point balancing," *IEEE Transactions on Industry Applications*, vol. 43, no. 3, pp. 751–760, May 2007.

[94] P. Chamarthi, P. Chhetri, and V. Agarwal, "Simplified implementation scheme for space vector pulse width modulation ofn-level inverter with online computation of optimal switching pulse durations," *IEEE Transactions on Industrial Electronics*, vol. 63, no. 11, pp. 6695–6704, Nov 2016.

[95] W. Wang, B. Zhang, and F. Xie, "A novel svpwm for three-level npc inverter based on m-mode controllability," *IEEE Transactions on Industrial Electronics*, vol. 65, no. 8, pp. 6055–6065, Aug 2018.

[96] J. Hu, J. Lin, and H. Chen, "A discontinuous space vector pwm algorithm in abc reference frame for multilevel three-phase cascaded h-bridge voltage source inverters," *IEEE Transactions on Industrial Electronics*, vol. 64, no. 11, pp. 8406–8414, Nov 2017.

[97] K. J. Pratheesh, G. Jagadanand, and R. Ramchand, "A generalized-switch-matrix-based space vector modulation technique using the nearest level modulation concept for neutral-point-clamped multilevel inverters," *IEEE Transactions on Industrial Electronics*, vol. 65, no. 6, pp. 4542–4552, June 2018.

[98] E. A. R. E. Ariff, O. Dordevic, and M. Jones, "A space vector pwm technique for a three-level symmetrical six-phase drive," *IEEE Transactions on Industrial Electronics*, vol. 64, no. 11, pp. 8396–8405, Nov 2017.

[99] F. Sebaaly, H. Vahedi, H. Y. Kanaan, N. Moubayed, and K. Al-Haddad, "Design and implementation of space vector modulation-based sliding mode control for grid-connected 3l-npc inverter," *IEEE Transactions on Industrial Electronics*, vol. 63, no. 12, pp. 7854–7863, Dec 2016.

[100] L. Gang, W. Dafang, W. Miaoran, Z. Cheng, and W. Mingyu, "Neutral-point voltage balancing in three-level inverters using an optimized virtual space vector pwm with reduced commutations," *IEEE Transactions on Industrial Electronics*, vol. 65, no. 9, pp. 6959–6969, Sept 2018.

[101] A. Choudhury, P. Pillay, and S. S. Williamson, "Dc-bus voltage balancing algorithm for three-level neutral-point-clamped (npc) traction inverter drive with modified virtual space vector," *IEEE Transactions on Industry Applications*, vol. 52, no. 5, pp. 3958–3967, Sept 2016.

[102] A. Lange and B. Piepenbreier, "Space vector modulation for three-level simplified neutral point clamped (3l-snpc) inverter," in *2017 IEEE 18th Workshop on Control and Modeling for Power Electronics (COMPEL)*, July 2017, pp. 1–8.

[103] Y. Zhang, J. Zhu, Z. Zhao, W. Xu, and D. G. Dorrell, "An improved direct torque control for three-level inverter-fed induction motor sensorless drive," *IEEE Transactions on Power Electronics*, vol. 27, no. 3, pp. 1502–1513, March 2012.

Appendix A

Experimental Setup

The experimental setup is shown in Figure A.1. The IPMSM with Hengstler incremental encoder 5000 pulses per revolution mounted on the rotor shaft is mechanically coupled to a DC machine acting as a load. The machine parameters are shown in Table A.1. The 3L-SNPC inverter is implemented using SEMIKRON SK50GBB066T and SK50GD12T4T IGBT modules with SKHI 71 drivers, DC-link capacitors C_1 and C_2 are each implemented using 200 μF MKP type capacitors, LEM current transducer LA 25-NP, LEM voltage transducer LV 25-P, and protection circuit, as shown in Figure A.2. All control algorithms are implemented using a Texas Instruments TI F28335 digital signal processor which is integrated into the development REN-F28335 super board, as shown in Figure A.3. A signal conditioning low pass filter circuit is specifically designed to make sure that the analogue inputs for the super board are in the range from 0V to 3V. Experimental results are gathered using dSPACE DS1106.

Figure A.1: Experimental setup

Rated power	1.5 kW
Rated torque	6 Nm
Number of pole pairs	2
Stator resistance	4.9 Ω
Permanent magnet flux linkage	0.586 Wb
d-axis inductance	0.0381 H
q-axis inductance	0.0873 H
DC link capacitors	200 $\mu F \times 2$
DC link voltage	300 V

Table A.1: Parameter of the test IPMSM

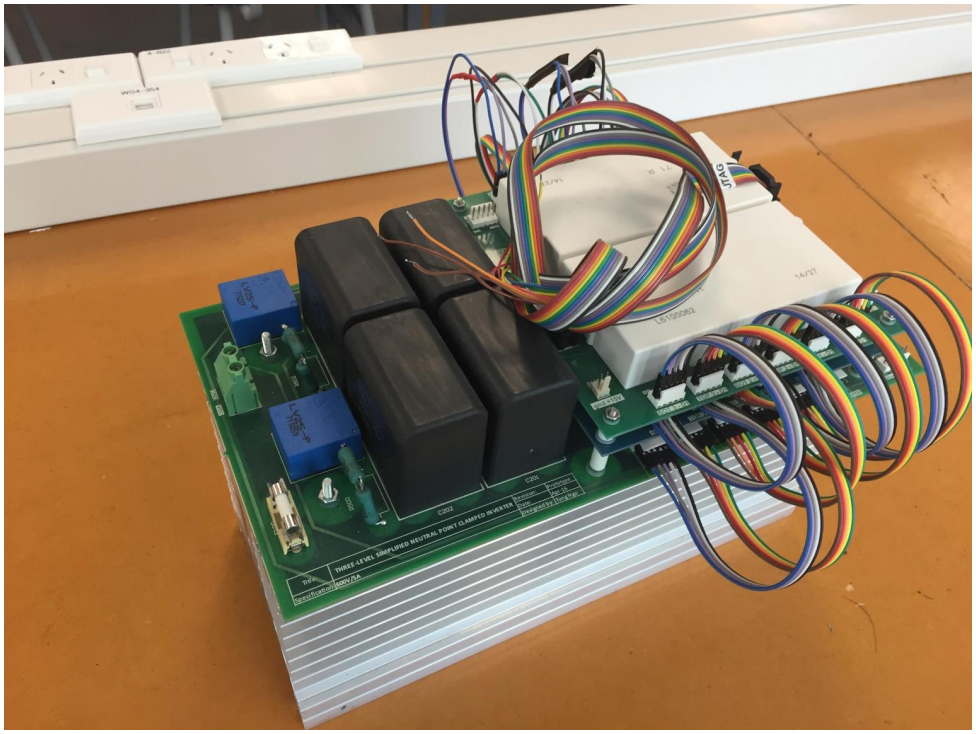

Figure A.2: Prototype of the 3L-SNPC inverter

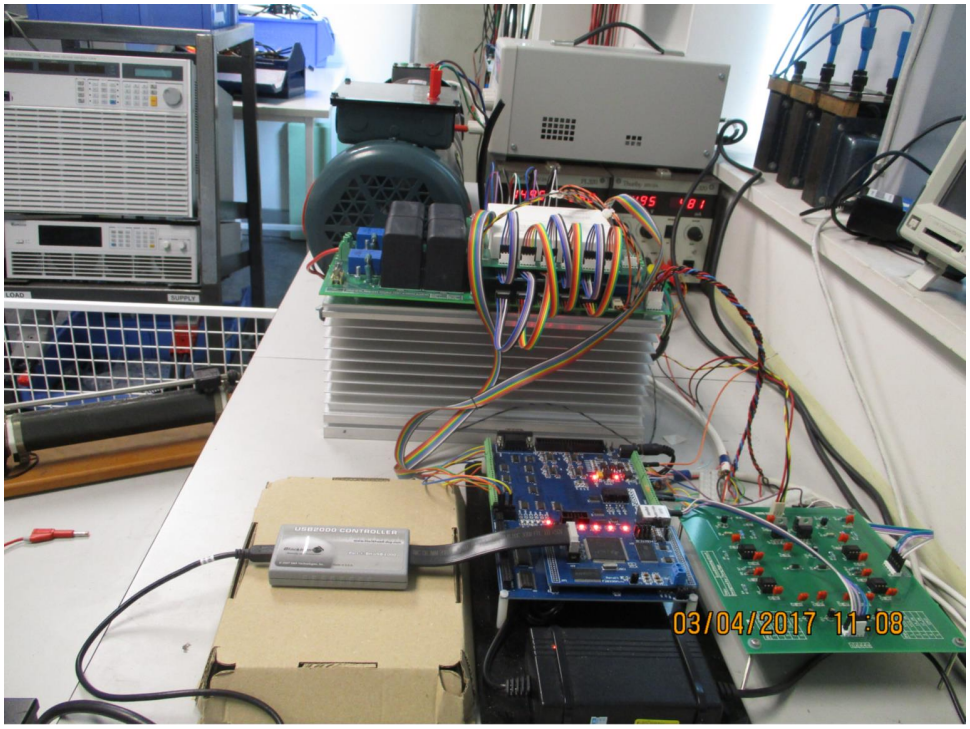

Figure A.3: Development control board and conditioning circuit

Appendix B

List of Publications

B.1 Conference Papers

- T. Ngo, G. Foo, C. Baguley, D. Mohan and Z. Xinan, "A novel direct torque control strategy for interior permanent magnet synchronous motors driven by a three-level simplified neutral point clamped inverter," *2016 IEEE Energy Conversion Congress and Exposition (ECCE)*, Milwaukee, WI, 2016, pp. 1-8.

- T. Ngo, G. Foo and C. Baguley, "A predictive torque control strategy for interior permanent magnet synchronous motors driven by a three-level simplified neutral point clamped inverter," *IECON 2016 - 42nd Annual Conference of the IEEE Industrial Electronics Society* , Florence, 2016, pp. 2648-2653.

B.2 Under Review

- Z. Xinan, T. Ngo and G. Foo, "A Simplified Deadbeat based Predictive Torque Control for Three-level Sparse Neutral Point Clamped Inverter fed IPMSM Drives using Novel SVM," *Journal of Emerging and Selected Topics in Power Electronics* , (**major revision**).

- T. Ngo, G. Foo, C. Baguley, and Z. Xinan, "A Space Vector Modulation Method for Three-level Simplified Neutral Point Clamped Inverter," *IET Electronics Letters* .

- T. Ngo, G. Foo, C. Baguley, and Z. Xinan, "Three-level Simplified NPC Inverter-fed Duty-cycle Control Based Predictive Torque Control of IPMSM with Torque Ripple Reduction," *IET Power Electronics*.

- T. Ngo, G. Foo, C. Baguley, and Z. Xinan, "A Novel SVM Algorithm for Three-level Simplified Neutral Point Clamped Inverter Fed IPMSM Drives," *IEEE Transactions on Mechatronics* .

- T. Ngo, G. Foo, C. Baguley, and Z. Xinan, "A Torque-Regulator-Based DTC Strategy for the 3L-SNPC Inverter-fed IPMSM Drives," *IEEE Transactions on Mechatronics* .

- T. Ngo, G. Foo, C. Baguley, and Z. Xinan, "Three-level Simplified NPC Inverter-fed Duty-cycle Control Based Direct Torque Control of IPMSM with Torque Ripple Reduction," *IET Electric Power Applications*.